BIOMARKER ACCESSIBLE AND CHEMICALLY ADDRESSABLE MECHANISTIC SUBTYPES OF BRAF MELANOMA

APPROVED BY SUPERVISORY COMMITTEE

Michael A. White, Ph.D (Mentor)

Ralph J. DeBerardinis, M.D., Ph.D. (Chairman)

Melanie H. Cobb, Ph.D.

Rolf A. Brekken, Ph.D.

ACKNOWLEDGEMENTS

I am very grateful that I had the opportunity to work with great people during my Ph.D. First, I would like to thank my mentor, Dr. Michael White, for his support and insightful guidance throughout my graduate life. I really appreciate the opportunities and the set of skills provided to me in his lab to help become a productive and independent scientist. I would like to thank to my thesis committee members, Drs. Rolf Brekken, Melanie Cobb and Ralph Deberardinis for their guidance, constructive discussions and invaluable feedbacks. I would also like to thank all my collaborators, in particular Drs. Ralf Kittler, Yonghao Yu, Noelle Williams and Jef De Brabander for their expertise and tremendous support. I would like to thank my colleagues, all current and former members of the White lab, for creating a great collaborative work environment. Particularly I would like to thank Elizabeth McMillan, Saurabh Mendiratta, Aubhishek Zaman and Tracy Rosales for their help and collaboration.

Finally, I would like to express my gratitude for my mom and my grandparents for their unconditional love and support throughout my life. I would also like to thank to my husband, Ugur, for his endless support, love, encouragement and helpful discussions throughout the years. None of this would have been possible without their love, strength and support, so I would like to dedicate this work to my loving mom, grandparents and my husband, Ugur.

BIOMARKER ACCESSIBLE AND CHEMICALLY ADDRESSABLE MECHANISTIC SUBTYPES OF BRAF MELANOMA

by

BANU ESKIOCAK

DISSERTATION / THESIS

Presented to the Faculty of the Graduate School of Biomedical Sciences

The University of Texas Southwestern Medical Center at Dallas

In Partial Fulfillment of the Requirements

For the Degree of

DOCTOR OF PHILOSOPHY

The University of Texas Southwestern Medical Center at Dallas

Dallas, Texas

August 2016

BIOMARKER ACCESSIBLE AND CHEMICALLY ADDRESSABLE MECHANISTIC SUBTYPES OF BRAF MELANOMA

Publication No. _____

Banu Eskiocak, Ph.D.

The University of Texas Southwestern Medical Center at Dallas, 2016

Supervising Professor: Michael A. White, Ph.D.

Genomic diversity and adaptive plasticity of melanoma tumors limit durable control with conventional and targeted therapies. Nevertheless, pathological activation of the ERK1/2 regulatory system is a linchpin tumorigenic mechanism associated with the majority of both primary and recurrent disease. To avoid common resistance mechanisms associated with perdurance of ERK1/2 signaling, we sought to identify therapeutic targets that are selectively required for tumorigenicity in the presence of pathological ERK1/2 signaling. Such targets could be leveraged in jiu jitsu fashion to breach selective pressure to engage any of the many

BRAF-independent ERK1/2 pathway activation mechanisms. By integration of multi-genome chemical and genetic screens; recurrent architectural variants in melanoma tumor genomes; and patient outcome data; we identified 2 mechanistic subtypes of BRAF(V600) melanoma that inform new cancer cell biology and offer new therapeutic opportunities. Subtype membership defines sensitivity to clinical MEK inhibitors versus TBK1/IKBKE inhibitors. Importantly, subtype membership can be predicted using a robust quantitative 5-feature genetic biomarker. This biomarker, or the mechanistic relationships linked to it, can identify a cohort of best responders to clinical MEK inhibitors (detectable in 25% of melanoma patients) and identify a cohort of TBK1/IKBKE inhibitor-sensitive disease among non-responders to current targeted therapy (detectable in 9.9% of melanomas).

TABLE OF CONTENTS

PRIOR PUBLICATIONS

Eskiocak, B., McMillan, E.A., Mendiratta, S., Kollipara, R.H., Zhang, H., Humphries C.G., Wang, C., Garcia-Rodriguez, J., Ding, M., Zaman, A., Rosales, T.I., Eskiocak, U., Smith, M., Sudderth, J., Komurov, K., DeBerardinis, R.J., Wellbrock, C., Davies, M.A., Wargo, J.A., Yu, Y., De Brabander, J.K., Williams, N.S., Chin, L., Rizos, H., Long, G., Kittler, R., White, M.A. Biomarker Accessible and Chemically Addressable Mechanistic Subtypes of BRAF Melanoma. Submitted to Cancer Cell.

McCarthy, N., Liu, J. S., Richarte, A. M., **Eskiocak, B.,** Lovely, C. B., Tallquist, M. D., & Eberhart, J. K. (2016). Pdgfra and Pdgfrb genetically interact during craniofacial development. Developmental Dynamics. http://doi.org/10.1002/dvdy.24403

Eskiocak, B., Ali, A., and White, M.A. (2014). The Estrogen-Related Receptor alpha Inverse Agonist XCT 790 Is a Nanomolar Mitochondrial Uncoupler. Biochemistry *53*, 4839-4846.

Kim, H.S., Mendiratta, S., Kim, J., Pecot, C.V., Larsen, J.E., Zubovych, I., Seo, B.Y., Kim, J., **Eskiocak, B.**, Chung, H., McMillan, E., Wu, S., De Brabander, J., Komurov, K., Toombs, J.E., Wei, S., Peyton, M., Williams, N., Gazdar, A.F., Posner, B.A., Brekken, R.A., Sood, A.K., Deberardinis, R.J., Roth, M.G., Minna, J.D., White, M.A. (2013). Systematic identification of molecular subtype-selective vulnerabilities in non-small-cell lung cancer. Cell *155*, 552-566.

Acharya, A., Baek, S.T., Huang, G., **Eskiocak, B.**, Goetsch, S., Sung, C.Y., Banfi, S., Sauer, M.F., Olsen, G.S., Duffield, J.S., Olson, E.N., Tallquist, M.D. (2012). The bHLH transcription factor Tcf21 is required for lineage-specific EMT of cardiac fibroblast progenitors. Development *139*, 2139-2149.

Acharya, A., Baek, S.T., Banfi, S., **Eskiocak, B.**, and Tallquist, M.D. (2011). Efficient inducible Cre-mediated recombination in Tcf21 cell lineages in the heart and kidney. Genesis *49*, 870-877.

Mellgren, A.M., Smith, C.L., Olsen, G.S., **Eskiocak, B.**, Zhou, B., Kazi, M.N., Ruiz, F.R., Pu, W.T., and Tallquist, M.D. (2008). Platelet-derived growth factor receptor beta signaling is required for efficient epicardial cell migration and development of two distinct coronary vascular smooth muscle cell populations. Circulation research *103*, 1393-1401.

LIST OF FIGURES

LIST OF TABLES

LIST OF ABBREVIATIONS

1-MNA	1-methylnicotinamide
ADSS	Adenylosuccinate synthase
AMPKα	AMP-activated protein kinase subunit catalytic subunit alpha 1
APC	Affinity propagation cluster
BAC	Bacterial artificial chromosome
bHLH	Basic helix-loop-helix
BRAF	B-Raf proto-oncogene, serine/threonine kinase
BrdU	5-Bromo-2′-deoxyuridine
BSA	Bovine serum albumin
CCCP	Carbonyl cyanide *m*-chlorophenyl hydrazone
CCLE	Cancer cell line encyclopedia
CDK4	Cyclin dependent kinase 4
cDNA	Complementary DNA
CEACAM1	Carcinoembryonic antigen related cell adhesion molecule 1
ChIPSeq	Chromatin immunoprecipitation with massively parallel DNA sequencing
CKAP5	Cytoskeleton associated protein 5
CND	Copy number driven
CNV	Copy number variation
CPII	Compound II
CTSV	Cathepsin V

DAPI	4′,6-Diamidine-2′-phenylindole dihydrochloride
DMSO	Dimethyl sulfoxide
DNA	Deoxyribonucleic acid
ECAR	Extracellular acidification rate
ERBB3	Erb-b2 receptor tyrosine kinase 3
ERRα	Estrogen related receptor alpha
EZH2	Enhancer of zeste 2 polycomb repressive complex 2 subunit
FAM69B	Family with sequence similarity 69 member B
FCCP	Carbonyl cyanide-*4*-(trifluoromethoxy)phenylhydrazone
FuSiOn	Functional signature ontology
GISTIC	Genomic identification of significant targets in cancer
GJB1	Gap junction protein beta 1
GOLPH3	Golgi phosphoprotein 3
GPR182	G protein-coupled receptor 182
GSEA	Gene set enrichment analysis
hTERT	Human telomerase reverse transcriptase
IKKε	Inhibitor of kappa light polypeptide gene enhancer in B-cells, kinase epsilon
IP	Intraperitoneal
ISG	Interferon stimulated gene
KPNA2	Karyopherin subunit alpha 2
KS test	Kolmogorov–Smirnov test
LAP	Localization and affinity purification tag

LATS1	Large tumor suppressor kinase 1
MAPK	Mitogen activated protein kinase
MET	MET proto-oncogene, receptor tyrosine kinase
MITF	Melanogenesis associated transcription factor
mRNA	Messenger RNA
mTORC1	Mammalian target of rapamycin complex 1
NARS2	Asparaginyl-tRNA synthetase 2
NNMT	Nicotinamide N-methyltransferase
NRP1	Neuropilin 1
OCR	Oxygen consumption rate
PBS	Phosphate buffered saline
PDX	Patient derived xenograft
PGC1α	PPARG coactivator 1 alpha
PK	Pharmacokinetics
PLAT	Plasminogen activator, tissue type
qPCR	Quantitative polymerase chain reaction
RAC2	Ras-related C3 botulinum toxin substrate 2
RagD	Ras related GTP binding D
REDD1	DNA damage inducible transcript 4
RNAi	RNA interference
ROC	Receiver operator characteristics
S2N	Signal to noise

SAM	S-adenosyl methionine
shRNA	Small hairpin RNA
siRNA	Small interfering RNA
SKCM	Skin cutaneous melanoma
SOX10	SRY-box 10
TAZ	Tafazzin
TBK1	TANK binding kinase 1
TCGA	The cancer genome atlas
TGFβ	Transforming growth factor beta
TGFBR2	Transforming growth factor beta receptor 2
TMT	Tandem mass tag
TSPAN10	Tetraspanin 10
UVM	Uveal melanoma
WBP11	WW domain binding protein 11
WT	Wild type
YAP1	Yes associated protein 1
ZEB2	Zinc finger E-box binding homeobox 2

CHAPTER ONE

INTRODUCTION

Despite displaying the greatest mutational diversity of any neoplastic disease (Alexandrov et al., 2013; Lawrence et al., 2013), fully half of all cutaneous melanomas harbor gain-of-function alleles in the *BRAF* proto-oncogene (Davies et al., 2002; Flaherty et al., 2012a). In consequence, direct pharmacological inhibition of the most common of these variants, BRAF(V600), has become a translational exemplar for targeted therapy (Chapman et al., 2011). A rapid series of advances have demonstrated both exceptional initial patient response, and ready emergence of therapy-resistant disease. Identified resistance mechanisms include gain-of-function mutations in *NRAS* (Nazarian et al., 2010), *MAP2K1* (Emery et al., 2009; Long et al., 2014a) and *PIK3CA* (Shi et al., 2014); amplification of COT (Johannessen et al., 2010), upregulation of PDGFRβ (Nazarian et al., 2010), EGFR (Girotti et al., 2013; Sun et al., 2014; Wang et al., 2015a), ERBB3 (Abel et al., 2013) and IGFR1 (Villanueva et al., 2010); and amplification (Shi et al., 2012) or alternative splice variant expression of BRAF (Poulikakos et al., 2011). The majority of these resistance mechanisms appear to be a consequence of BRAF(V600)-independent mitogen-activated protein kinase (MAPK) pathway activation. To defend against this, many current clinical and translational efforts are focused on chemical inhibition of the protein kinases MEK1/2 and ERK1/2 that mediate BRAF(V600)-induced tumorigenicity (Flaherty et al., 2012b). However, the absence of common disease-specific alleles requires targeting of wild-type proteins commonly engaged

to support normal tissue homeostasis. This leads to the conundrum of dose-limiting toxicity, which can narrow the therapeutic window and limit patient benefit (Lito et al., 2013). Melanoma-selective vulnerabilities within the ERK1/2 regulatory network may offer themselves as additional target opportunities, however, the diversity and cryptic pharmacological accessibility of this regulatory network is a considerable challenge confronting that approach. Remarkable advances in tolerance-breaking immune modulation may lead to effective therapy that is agnostic to BRAF mutant status and MAPK pathway activation, but this will clearly be aided by collaborating interventions that directly target tumor tissue (Cooper et al., 2014; Frederick et al., 2013; Hamid et al., 2013; Hodi et al., 2010; Robert et al., 2011; Topalian et al., 2012).

As an alternative approach for nomination of melanoma cell-autonomous intervention targets, we considered opportunities associated with collateral mechanistic liabilities that arise as a consequence of pathological MAPK pathway activation. If detectable and actionable, targeting these liabilities would be expected to be synthetic-lethal to any and all of the myriad genomic alterations that lead to tumorigenic disregulation of the MAPK regulatory network. A tiered multi-genomic RNAi-mediated screening strategy coupled to molecular correlates in human tumor tissues, patient outcome data, and consideration of 130 drugs and investigational chemical compounds uncovered two mechanistic subtypes of melanoma. These subtypes are simultaneously detectable with a robust quantitative biomarker, and actionable through distinct chemical vulnerabilities. A SOX10-addicted subtype specifies BRAF(V600) melanomas that are intrinsically sensitive to clinical MEK

inhibitors irrespective of sensitivity or resistance to clinical BRAF(V600) inhibitors, is detectable in ~ 25% of the BRAF(V600) melanoma patient population, and was validated in 3 independent patient cohorts on two continents. Characterization of the direct SOX10 transcriptional network in this subtype delivered previously unknown lineage-specific-, tumor activated-, proteins required for matrix-independent colony growth and defined discrete protumorigenic transcriptional programs collaboratively controlled by SOX10 together with MITF. An "innate immune" subtype specifies BRAF(V600) and BRAF(WT) melanomas that are intrinsically resistant to clinical MEK and BRAF inhibitors, and is detectable in ~9.9% of melanomas. Unbiased virtual and empirical chemical screening efforts identified low nanomolar TBK1/IKKε inhibitors, validated by four different chemical scaffolds, as lead compounds that are selectively toxic in these otherwise targeted therapy resistant melanomas in vitro and in vivo. The mechanism of action appears to be through inhibition of TBK1/IKKε-dependent Hippo pathway suppression and AKT pathway activation in this subtype. A key mechanistic determinant of subtype membership was determined to be nicotinamide N-methyltransferase (NNMT)-dependent chromatin organization. These findings contribute to productive genomics-guided medicine by both predicting the best responders to currently available BRAF/MEK-targeted agents and by nominating TBK1/IKKε inhibition as a therapy for an important BRAF/MEK-targeted therapy resistant subtype.

CHAPTER TWO

RESULTS

Integrative Analysis of Functional Genomics and Copy Number Variation in Melanoma Cells and Tissues

To help identify biologically relevant intervention targets in melanoma, from cell-based screening efforts, we combined genome-wide RNAi toxicity screens in melanoma cell lines with corresponding detection of genomic copy number gain in melanoma tumors. We reasoned that gene products commonly participating in bona fide context-specific support of melanoma cell survival would likely be the subjects of selective pressure for gain-of-expression genomic alterations during human tumor initiation and progression. To do this, a z-score distribution, derived from viability assays using siRNA pools targeting each of 21,125 genes in MNT1 cells, was compared to corresponding gene amplifications detected in resected tumors from 49 melanoma patients (Figure 1A). Copy number gain was defined as $\log_2 \geq 0.4$ in tumor versus matched normal tissue (244K array). The leading edge of the intersection of candidate "viability genes" and detectably amplified genes contained the well-appreciated lineage-associated oncogenes *BRAF* (Davies et al., 2002), *MITF* (Garraway et al., 2005) and *GOLPH3* (Scott et al., 2009) (Figure 1A) as well as a cohort of ~60 additional candidates. The latter were retested with multiple independent siRNAs in the original screening host (Figure 2A). Those with reproducible and likely on-target viability phenotypes were further evaluated for consequences on cell proliferation (BrdU incorporation, Figure

2B) and anchorage-independent growth (soft agar colony formation, Figure 2C) in both MNT1 (Figure 1B) and an additional melanoma cell line (WW165, Figures 1C, 2D, 2E, and 2F) chosen due to its reported phenotypic similarity to MNT1 (Hoek et al., 2004). Combinatorial consideration of these assays helped resolve cytotoxic (Figure 1D) and cytostatic (Figure 1E) siRNA phenotypes, as well as the clonal magnitude of the siRNA phenotypes within the cell population (Figure 1F). Finally, we examined the commonality and selectivity of these siRNA sensitivities across a panel of 17 additional melanoma lines and 3 strains of telomerase immortalized non-tumorigenic epithelial cells (Ramirez et al., 2004) (Figures 2G and 2H). The resulting phenotypic profiles revealed both "public" and "private" vulnerabilities within the melanoma cell line panel (Figure 1G).

Affinity propagation clustering (APC) (Frey and Dueck, 2007; Witkiewicz et al., 2015) was used to delineate deterministic patterns of commonality among cell lines derived from either whole genome expression variation or siRNA sensitivity patterns. Whole genome transcript profiles suggest 5 expression subtypes are present within this panel (Figures 1H and 2I). However, these clusters had unimpressive correspondence to siRNA phenotype-based clusters (Figure 1I) indicating global gene expression phenotypes, considered as a whole, did not specify selective response to the siRNA panel. Therefore, we employed a regularized linear regression algorithm (Barretina et al., 2012; Garnett et al., 2012; Potts et al., 2015) to help identify distinct gene expression features that may be predictive of response to depletion of the candidate viability genes. This returned 15 sparse quantitative gene expression profiles significantly linked to sensitivity to depletion of SOX10, DHRS4, CKAP5, LIF, KPNB1,

CMIP, TPX2, PIPOX, GPR182, GPR160, SYT11, MVP, CCDC15, APLP2, and PDIA3. Importantly, these expression profiles were detectable and discriminatory (Z-scores≥2) within a panel of 470 patient samples (SKCM, TCGA), and by extrapolation, cumulatively accounted for 22% of the patient population (105 samples with at least 1 target/biomarker association) (data not shown). In addition, we asked if the candidate viability genes were significantly overexpressed when detectably amplified (GISTIC, (Mermel et al., 2011)) in a cohort of 106 melanoma tumor samples with matched genomic copy number variation (CNV) and mRNA expression annotation. This revealed KPNB1, TPX2, BRAF, GOLPH3, SOX10, METTL18, UBE2Z, CEP68, MARCH6, LRP12, ZNF706, ZC3H7B, ATXN10, COG5, MTX1, and ZNF79 as candidate high-confidence copy number driven melanoma cell survival genes (Figure 1G). Among these, cellular sensitivity to depletion of BRAF, GOLPH3, and SOX10 also correlated with corresponding target gene expression within the melanoma cell line panel (Figure 1G, Pearson correlation and expression variance). The lineage-specific transcription factor, SOX10, has recently been demonstrated to support melanoma initiation in mice (Shakhova et al., 2012). Thus, in addition to MITF (Garraway et al., 2005), SOX10 presents itself as a likely lineage-selective, copy number driven oncogene in human melanoma.

The SOX10 Regulatory Network Supporting Cell Autonomous Melanoma Cell Growth and Survival

Among the copy number driven survival genes detected in the melanoma cell line panel, SOX10 displayed the largest expression variation, and this was significantly correlated with

SOX10 gene copy number (Figure 4A, P=0.006) and SOX10 siRNA sensitivity among the cell lines (Figure 3A, Mann-Whitney P<0.0001; Figure 4B, P=0.018). Effective SOX10 depletion was relatively innocuous in immortalized non-tumorigenic melanocytes (Eskiocak et al., 2014) (Figures 4C and 4D). In contrast each of 4 independent siRNA oligos significantly reduced viability (Figures 4E, 4F, and 4G) and BrdU incorporation in MNT1 cells (Figures 4H and 4I). Moreover, SOX10 depletion abolished the anchorage independent growth of MNT1 and WW165 cells (Figures 4J and 4K), indicating that there are no resistant subpopulations in these SOX10-addicted cell lines.

MITF is a direct target gene of the SOX10 transcription factor (Huber et al., 2003; Potterf et al., 2000; Verastegui et al., 2000), and the MITF protein is an important melanoma survival factor in at least some subtypes of disease (McGill et al., 2002). This suggests that the mechanism of SOX10 participation in melanoma cell survival may be a direct consequence of MITF activation. However, we found that detectable MITF protein expression was uncoupled from SOX10 addiction in some melanoma cell lines, indicating there may be MITF-independent contributions of SOX10 to melanoma cell survival (Figure 4L). Therefore, we directly characterized the SOX10 client gene network. A SOX10-LAP (Localization and affinity purification tag) BAC transgenic MNT1 cell line was generated that expresses a SOX10-LAP fusion protein under control of native SOX10 promoter elements (Hua et al., 2009; Kittler et al., 2013; Poser et al., 2008). This allowed for highly specific solid-phase recovery of SOX10-LAP-bound DNA fragments by chromatin immunoprecipitation (ChIP), in the absence of supra-physiological SOX10 expression, that

were subsequently quantified by massively parallel sequencing (HiSeq2000, Illumina) (Figures 3B and 4M). De novo DNA-binding motif discovery returned a single significant motif present within 100 bp of sequences flanking 100% of the peak summits (Figure 3C). Mapping against transcription factor annotation databases (JASPAR and TRANSFAC) returned a strong match of this motif to a predicted SOX10 DNA binding motif (Figure 3C) and was consistent with recovery of known SOX10 targets in neural crest derived melanocytes (MITF) (Huber et al., 2003) and Schwann cells (ERBB3 and GJB1) (Bondurand et al., 2001; Prasad et al., 2011) (Figure 4N). This motif was consistently present as a paired inverted repeat, suggesting SOX10 occupies these sites as a homodimer (Figure 3C). Three additional motifs were recovered that occurred at frequencies of 13-21% and corresponded to candidate consensus binding sites for TFAP, TCF7, and bHLH-family transcription factors (Figure 3C).

To identify genes occupied by SOX10 that are also responsive to SOX10 regulation, we generated whole-genome transcript profiles from MNT1 cells with and without SOX10 depletion. The first-degree protein-protein interaction network (Kim et al., 2013a; Komurov et al., 2012; Komurov et al., 2010) of these SOX10 targets included three nodes that are pharmacologically accessible: NOTCH, MET, and ERBB3 (Figures 3D and 4O). MET protein accumulation and signaling was sensitive to both SOX10 and MITF (Beuret et al., 2007; McGill et al., 2006) depletion, while ERBB3 and NOTCH were selectively sensitive to SOX10 depletion (Figure 3E), consistent with both collaborative and distinct transcriptional programs downstream of SOX10 and MITF. Within this panel of experimentally defined

SOX10 target genes, we identified 25 genes with expression patterns that significantly correlated with SOX10 in three independent melanoma tumor cohorts (Figure 3F). This enrichment was greater than that predicted by chance (P=4.4E-15) suggesting a conserved functional interaction between SOX10 and these genes in patient samples. siRNA-mediated testing of all 25 in soft agar assays identified 6 that support anchorage-independent colony formation in MNT1 cells (Figure 3G). Notably, these included the type1 Charcot-Marie-Tooth disease gene GJB1 (Kleopa and Sargiannidou, 2014); the melanoma metastasis prognostic indicator, CEACAM1 (Sivan et al., 2012; Thies et al., 2002); and the BRAF therapy resistance gene ERBB3 (Abel et al., 2013).

RagD is an MITF Transcriptional Target Gene That Promotes MITF Nuclear Translocation

To potentially identify key MITF targets, indirectly engaged by SOX10, which support melanoma cell survival, we examined the intersection of SOX10 and MITF dependent genes with the MNT1 genome-wide siRNA toxicity screen (Figure 5A). This returned TPX2 (Figure 1G), TSPAN10 (Figures 1F and 1G), FOXN2 and RagD. Integrated analysis of MITF DNA binding sites (Strub et al., 2011) near MITF-responsive genes (Hoek et al., 2008) in public data sets suggested RagD is a direct MITF transcriptional target. Furthermore RagD expression positively correlated with SOX10 and MITF in 3 independent melanoma tumor cohorts (Table 1). RagD encodes a member of the Rag family of GTPases (RagA, B, C and D, also known as RRAGA-D). These proteins form active heterodimers, in response to amino acids, that are required to induce recruitment and activation of mTORC1 on lysosomes

(Sancak et al., 2010; Sancak et al., 2008). Consistent with the whole genome transcript array data, RagD mRNA concentrations and accumulation of RagD protein were significantly reduced upon short-term depletion of SOX10 or MITF (Figures 5B and 5C). In addition, inhibition of cell viability upon RagD depletion was recapitulated with 3 independent siRNA oligonucleotides (Figure 6A) and correlated with SOX10 addiction in the melanoma cell line panel (Figure 5D). mTORC1 activity, as indicated by accumulation of activation site phosphorylation on p70S6 kinase, was substantially impaired upon depletion of SOX10, BRAF, or MITF in MNT1 cells (Figure 5C). However, depletion of RagD or any other Rag family member had little to no effect on mTORC1 pathway activation (Figures 5C and 6B), suggesting that individual Rag proteins are not limiting for support of mTORC1 activity. Furthermore, the inhibition of cell viability (Figure 6C) and profound ablation of soft agar colony formation, observed upon RagD depletion, was not recapitulated by depletion of any other Rag family member (Figure 5E). Of note, among Rag family genes, RagD is selectively upregulated in melanoma as compared to nevi (Talantov et al., 2005) (Figure 5F), and positively correlates with SOX10 expression in melanoma samples. These cumulative observations led us to consider potential Ragulator/mTORC1-independent mechanisms for participation of RagD in melanoma cell survival.

From whole genome transcript arrays, we were surprised to find that over half of the global gene expression changes observed upon RagD depletion overlapped with those observed upon MITF depletion (Figure 5G; hypergeometric distribution $P<2.220446e-16$ (machine zero)). 36 of these 73 genes also had MITF binding sites (Strub et al., 2011) (hypergeometric

distribution P<2.220446e-16 (machine zero)) strongly suggesting that the observed overlap is not due to cell toxicity, but rather reflects a change in MITF transcriptional output. To hunt for mechanistic leads, we turned to fungi, which encode two orthologs of mammalian Rag proteins, Gtr1p and Gtr2p that may model conserved ancestral functions of mammalian Rag proteins that are mTOR-independent. In budding yeast, Gtr1p/2p interact physically and functionally with the nuclear pore complex and nuclear transport machinery (Nakashima et al., 1999; Wang et al., 2005) (Figure 5H); partially localize to the nucleus (Sekiguchi et al., 2008); and directly support import of nuclear proteins (Sekiguchi et al., 2004). Among the 4 mammalian Rag proteins, we found that RagD exclusively contained a predicted nuclear localization sequence (Figure 6D), and that RagD selectively interacted directly with the nuclear transport receptor karyopherin alpha 2 (KPNA2) (Figure 5I). Although little RagD was detectable in nuclear fractions of growing cells, inhibition of protein turnover revealed selective accumulation of RagD in the nucleus as compared to RagA, RagB or RagC (Figure 6E). Notably, RagD depletion impaired nuclear accumulation of MITF (Figures 5J, 6F and 6G), while RagD overexpression induced enhanced nuclear accumulation of MITF (Figure 6H). These cumulative observations suggest the presence of a feedback amplification loop, whereby induction of RagD expression by MITF promotes enhanced MITF nuclear localization and consequent enhanced transcriptional activation of MITF targets. However, the contribution of SOX10 and MITF to support of mTORC1 activity in proliferating melanoma cells is not mediated by RagD, and instead appears to be a consequence of direct transcriptional repression, by SOX10 and MITF, of the mTORC1 inhibitory protein REDD1 (Brugarolas et al., 2004) (Figure 6I).

The ERRα Inverse Agonist XCT 790 is a Nanomolar Mitochondrial Uncoupler

To try to chemically inhibit RagD activity, we tested estrogen-related receptor alpha (ERRα) inverse agonist XCT 790 based on the observations that RagD protein concentrations reduced in response to XCT 790 exposure in HCT116 cells (data not shown). However RagD protein concentrations did not change upon XCT 790 exposure in MNT1 melanoma cells (data not shown) and melanocytes and melanoma cells were indiscriminately sensitive to XCT 790. A distributive analysis of baseline oncogenic pathway activity upon exposure of MNT1 cells to XCT 790 revealed potent inactivation of mTORC1 signaling together with accumulation of active AMP kinase (AMPK) as indicated by T172 phosphorylation status (Figure 7A). These alterations occurred within an hour, and were uncoupled from accumulation of ERRα (Figure 7B). AMPK activation by low micromolar XCT 790 was observed in all cell lines tested, including multiple melanoma lines (Figure 8A), telomerase immortalized human melanocytes (Figure 8B), and bronchial epithelial cells from three different patients (Ramirez et al., 2004) (Figure 8C).

Time and dose response analyses indicated AMPK pathway activation occurred within 5 minutes of XCT 790 exposure (Figure 9A) with doses as low as 390 nM (Figure 9B). Importantly, siRNA-mediated ablation of ERRα had no effect on this response, indicating the participation of an alternate target of XCT 790 (Figure 9C). Reduction in ATP concentrations, as measured by a luciferin/luciferase couple assay, occurred within 20 minutes of XCT 790 exposure (Figure 9D) suggesting that the observed AMPK activation

may be secondary to deregulation of energy production. To examine this directly, we tested the consequence of XCT 790 exposure on mitochondrial respiratory potential through measurements of oxygen consumption and extracellular acidification. We observed a substantial increase in oxygen consumption rates (OCR) in as early as 8 minutes post XCT 790 exposure (Figure 10A) concomitant with an increase in extracellular acidification (ECAR) (Figure 10B). Elevated OCR was persistent at the lowest doses tested, but eroded over time in a dose-dependent fashion (Figure 10A). XCT 790-induced OCR was insensitive to the ATP synthase inhibitor oligomycin or to the proton ionophore FCCP, but collapsed in the presence of the complex 1 inhibitor rotenone (Figure 10C). These mitochondrial electron transport chain inhibitors also did not further increase ECAR above levels observed with XCT 790 alone, (Figure 10D) suggesting that XCT 790 had induced maximum adaptive lactate production downstream of mitochondrial respiratory defects. Taken together, these observations suggest XCT 790 rapidly uncouples oxygen consumption from ATP production in intact mitochondria (Figure 10A, C). Importantly, these effects were completely independent of ERRα (Figure 10E, F) expression or overt alterations in the concentration of mitochondrial proteins over the time course of the experiment (Figure 10G).

These observations, together with the capacity of FCCP to mimic XCT 790 activation of AMPK (Figure 11A) and decrease in ATP levels (Figure 11B) with similar timing and potency, strongly suggest XCT 790 is a chemical uncoupler of mitochondrial membrane potential independently of interaction with ERRα. Direct measurements of delta phi, using MitoTracker CMXRos, demonstrated a dose-dependent inhibition of mitochondrial

membrane potential (Figure 11C) by XCT 790 in the absence of effects on mitochondrial mass (Figure 11D). The consequent defect in cellular ATP production was evident by a dramatic inhibition of autophagolysosomal maturation, which requires high ATP consumption to fuel lysosomal acidification (Figure 11E).

We find that the thiadiazoleacrylamide XCT 790, developed as an ERRα inverse agonist, is a potent mitochondrial uncoupler. This activity leads to rapid depletion of cellular ATP pools, which in turn activates AMPK- a master regulator of metabolic homeostasis. Importantly, these effects are completely independent of ERRα activity. ERRα depletion neither mimicked nor rescued the effects of XCT 790 measured here. XCT 790 is commonly used at 1-20 mM concentrations for 8-24 hours to examine the biological significance of ERRα activity in cells (Bianco et al., 2009; Bombail et al., 2010; Bonnelye et al., 2011; Chang et al., 2011; Chen and Wong, 2009; Dwyer et al., 2010; Fiori et al., 2011; Fisher et al., 2011; Gacias et al., 2012; Kong et al., 2009; Krzysik-Walker et al., 2013; Lanvin et al., 2007; Liu et al., 2006; Lu et al., 2011; Murray and Huss, 2011; Rasbach et al., 2010; Teng et al., 2014; Teyssier et al., 2008; Wang et al., 2010; Wu et al., 2009; Zhu et al., 2010; Zou et al., 2014). Rapid XCT 790-induced perturbations of energy production and energy sensing pathways occurred at much lower doses. Thus most, if not all, reported biological responses to XCT 790 are in the context of combinatorial inhibition of ERRα and mitochondrial respiratory activity and should be interpreted accordingly.

The biochemical phenotype, timing, and dose-sensitivity of the cellular response to XCT 790 is identical to the well-studied proton ionophore, carbonyl cyanide-*4*-(trifluoromethoxy)phenylhydrazone (FCCP) (Benz and McLaughlin, 1983). This molecule and the closely related carbonyl cyanide *m*-chlorophenyl hydrazone (CCCP) disrupt mitochondrial transmembrane electrochemical gradients by directly facilitating proton transport across the lipid membrane barrier (Benz and McLaughlin, 1983; Kasianowicz et al., 1984). All three chemicals are amphipathic nitriles, which in the case of FCCP and CCCP, is a structural feature that facilitates discharge of the mitochondrial pH gradient. Thus, it is highly likely that XCT 790 is also a proton ionophore with a consequent direct mechanism of action against mitochondrial respiration.

There is considerable genetic, molecular and biochemical evidence that ERRα is a bona fide regulator of energy homeostasis in cells and tissue. Through interactions with PGC-1α and PGC-1β, ERRα can directly induce the expression of genes that support oxidative phosphorylation and mitochondrial biogenesis in response to changes in energy demand (Huss et al., 2007; Huss et al., 2002; Kamei et al., 2003; Laganiere et al., 2004; Schreiber et al., 2003). Furthermore, XCT 790 can clearly interfere with this activity by directly dissociating ERRα from its protein cofactors. Thus, the potent and rapid destruction of mitochondrial membrane potential by XCT 790, independently of ERRα activity, is a particularly confounding phenotype associated with use of this tool compound for exploration of ERRα biology.

SOX10 Addiction Specifies Sensitivity of BRAF Mutant Melanomas to BRAF and MEK Inhibitors In Vitro and in Patients

SOX10 suppression has been reported to be associated with resistance to BRAF-targeted therapy in melanoma, at least in part as a consequence of increased TGF-β receptor 2 (TGFBR2) expression (Sun et al., 2014). Indeed, we found that TGFBR2 expression is likely directly suppressed by SOX10 occupancy of TGFBR2 gene regulatory elements. This prompted us to examine the correlation of SOX10 addiction with *BRAF* mutation status and response to clinical BRAF and MEK inhibitors. Oncogenic *BRAF* mutations were present in SOX10-dependent and SOX10-independent melanoma cell lines with distinct, bimodal expression of the elastic net-derived expression biomarkers correlating with SOX10 addiction (Figure 12A). Of note, SOX10-dependent cell lines were sensitive to the MEK inhibitor trametinib, while SOX10-independent cell lines were uniformly resistant to both trametinib and the mutant BRAF inhibitor vemurafenib irrespective of BRAF mutant status (Figures 12B and 12C). The linear weighted sums of the individual expression values for each feature in the expression biomarker, for each cell line, showed significant correlation with vemurafenib and trametinib LD50 (Figures 13A and 13B) and log kill as defined by area under the curve (Figures 12D and 12E); suggesting potential utility of this metric as a prediction score for response to targeted therapy. To test this outside of the "discovery" cell line panel, we rank-ordered the 61 melanoma cell lines from the Cancer Cell Line Encyclopedia (CCLE) according to the available Affymetrix-derived individual expression values for each biomarker feature (RAC2, NRP1, MGC4294, CTSV, FAM69B) (Figures 12F and 13C). 5 publically accessible BRAF(V600E) cell lines present in the predicted-resistant

tail of the distribution were tested, and 4 of these were found to be vemurafenib and trametinib resistant (Figures 12G and 12H). Among the predictive expression features, we found that sensitivity to depletion of RAC2 specifically correlated with SOX10-independence (blue bars), suggesting discrete mechanistic contributions of SOX10 and RAC2 to the targeted therapy sensitive versus targeted therapy resistant classes (Figure 13D). Of note, SOX10 expression alone was not sufficient to predict targeted therapy resistance (Figure 12F, SOX10 signal intensity); emphasizing the utility of the Elastic Net-derived feature set.

To assess biomarker performance using discrete measurements of biomarker gene expression, as opposed to whole genome transcript profiles, qPCR was employed across the cell line panel (Figure 12I). These values were then used to assign a prediction score (summed weighted expression) to every cell line (Figure 13E). The samples in the tails of the score distribution (5 lowest and 5 highest) corresponded to a significant separation of drug sensitivity between the two “subtypes” (Figure 12J). Moreover, a two-class comparison of predicted versus measured response to targeted therapy across the cell panel returned excellent receiver/operator characteristics with significant area under the curve (Figures 13F and 13G).

The magnitude of the separation of sensitivity of these cell lines to vemurafenib and trametinib prompted us to ask if the quantitative expression features associated with SOX10 addiction could discriminate melanoma tumor responses to BRAF and/or MEK-targeted

therapy. To test this, we first leveraged a clinical study with whole genome transcript profiles derived from resected tumors from 30 patients with BRAF(V600)-mutant melanoma undergoing treatment with the BRAF(V600)-inhibitors dabrafenib or vemurafenib (Rizos et al., 2014). The multi-feature expression biomarker was used to assign probability values for membership of each patient in the SOX10-addicted (vemurafenib/trametinib sensitive) class or the SOX10-independent (vemurafenib/trametinib resistant) class. Given the on/off nature of the expression of the biomarker genes in the cell lines associated with these classes (Figures 12A and 13C), we employed a summed-weight metric to rank the patients based on the expression values of the biomarker genes in the patients' tumors (Figure 13H). A survival analysis, comparing the quartiles from the extrema of the resulting ranked distribution (<-0.05 versus >0.05, Figure 13H), revealed a marked separation in patient outcome-- with membership in the "vemurafenib/trametinib resistant" class predictive of poor prognosis (Figure 12K). Importantly, this result was reproducible in an independent cohort of patients who received BRAF(V600) inhibitors (dabrafenib or vemurafenib) or a combination of BRAF(V600) and MEK inhibitor (dabrafenib and trametinib) therapy (Figures 12L and 13I). This outcome association is especially notable, as membership in the "vemurafenib/trametinib resistant" class corresponds to better prognosis in patients treated with standard chemotherapy in two independent cohorts (Figures 13K and 13L) (Jonsson et al., 2010). Finally, we analyzed a third independent cohort that reported best overall response in patients undergoing BRAF(V600) (dabrafenib or vemurafenib) or combination of BRAF(V600) and MEK inhibitor (dabrafenib and trametinib) therapy, and was associated with RNASeq transcript profiles derived from melanoma tumors isolated prior to therapy

(Hugo et al., 2015) (Figure 13J). As this cohort was too small to select the tails of the sample score distribution, we resorted to dichotomization of the patients into 2 groups of equal size based on the summed-weight metric (Figure 13J). Nevertheless, we still observed a significant enrichment of poor responders in the predicted resistant group (Figure 12M). Together, these observations support the notion that the cellular SOX10-addiction derived quantitative multi-feature biomarker can detect distinct mechanistic subtypes of melanoma that correspond to intrinsic sensitivity or resistance to BRAF(V600)/MEK targeted therapy.

To examine if the expression biomarker may also report acquired resistance, we sampled tumors from patients before and during the course of targeted MAPK pathway therapy. Again, individual gene features were measured by qPCR and used to calculate a predicted response score. We found that 4 out of 4 patients with an initial "targeted therapy sensitive" score progressed to a "resistant" score on therapy. Moreover, the prediction score did not change in 2 out of 2 patients whose initial signature was already in the "targeted therapy resistant" class (Figure 12N). Similar observations were made with an in vitro model of acquired resistance to trametinib (Figures 13M and 13N), indicating a cancer cell-autonomous biomarker signature evolution.

Nomination of TBK1 as a Therapeutic Target for Drug-Resistant Melanoma

Given the observed potential for predictive molecular discrimination of intrinsically BRAF inhibitor (BRAFi)-sensitive and resistant melanoma together with the need to identify treatment strategies for patients harboring BRAFi-resistant tumors, we sought chemical leads

with selective activity in the targeted-therapy resistant melanoma cell line cohort. To do this, we used the predictive feature set to stratify 35 melanoma cell lines for which whole genome expression data was available together with experimentally defined or imputed IC_{50}s for up to 130 chemical compounds (Garnett et al., 2012) (Figure 14A). Signal-to-noise (S2N) ratios were then calculated for each of these 130 compounds, according to their activity in the top 10% predicted BRAFi/MEKi sensitive versus the top 10% predicted BRAFi/MEKi insensitive cell lines, in order to identify any compounds with selective activity in the targeted therapy resistant class (Figure 15A). BX795, a low nanomolar inhibitor of PDK1 (Feldman et al., 2005) and the non-canonical IkB kinases TBK1 and IKKε (Bain et al., 2007), was the top hit (Figure 14B). Differential toxicity of BX795 was first validated against 2 predicted sensitive cell lines (LOXIMVI and RPMI7951) and 2 predicted resistant cell lines (SKMEL28 and COLO792) (Figure 14C). To potentially disambiguate the mode-of-action underpinning the selective toxicity of BX795, we tested a 6-aminopyrazolopyrimidine (compound II) previously developed as a selective TBK1 inhibitor with no activity against PDK1 (Ou et al., 2011) as well as BX795 in a panel of 19 BRAF mutant melanoma cell lines (Figure 14D and Figure 15K). While compound II was more potent against sensitive cell lines, these structurally distinct chemicals displayed highly correlated activity across the cell panel (Figures 14E, 15B, 15C, 15D, 15E and 15J), suggesting activity against TBK1/IKKε is responsible for the cytotoxic phenotype. Consistent with this MRT6737, a BX795 derivative that retains activity against TBK1 but not PDK1 (Clark et al., 2011), and Momelotinib, a JAK1, 2, 3/TBK1/IKKε inhibitor, also exhibited similar dose-dependent selective toxicity profiles (Figures 15M and 15N). TBK1i sensitive cell lines responded to inhibition of

TBK1/IKKε activity by induction of apoptosis, suggesting these non-canonical IKK family members support context selective cell survival signaling (Figure 14G). Importantly, sensitivity to TBK1/IKKε inhibitors inversely correlated with both real and predicted sensitivity to trametinib (Figures 14F, 15F, 15G, 15H and 15I). Taken together, these observations indicate selective vulnerability of vemurafenib/trametinib-resistant BRAF mutant melanoma cells to inhibition of TBK1/IKKε activity. Notably, we found that A375 clones, with acquired resistance to MEK inhibition, were also sensitized to TBK1/IKKε inhibition in a manner predicted by their biomarker scores (Figure 14K).

Within the discovery panel and the CCLE panel, we noted the presence of BRAF wild type melanoma cell lines with biomarker signatures that were predictive of sensitivity to TBK1/IKKε inhibition (Figure 12A and Figure 13C). Evaluation of 10 BRAF wild-type lines from across the cell line panel revealed significant correspondence of BX795- and compound II-sensitivity with the biomarker scores (Figures 14H, 14I and 15L). CHL1 was an unanticipated responder, with a biomarker score that predicted resistance to TBK1/IKKε inhibition (Figure 14H). To search for an underlying discriminating feature associated with this response, we compared the whole genome transcript profiles of TBK1i-sensitive (Hs895.T, Hs934.T, Hs839.T and CHL1) and TBK1i-resistant (COLO729 and MEWO) BRAF wild-type melanoma cell lines. Signal-to-noise analysis revealed selective downregulation of pigmentation genes and PGC1α, all MITF transcriptional targets, in TBK1i-sensitive cell lines; a correlation that was also observed in CHL1 (Figure 14J). This indicates the biomarker score has some false negative associations that may be a

consequence of similar cellular states that occur through different genetic or epigenetic alterations. Nevertheless, ROC curve analysis, of actual versus predicted response to compound II, of all tested melanoma cell lines (N=16 from the discovery set, N=13 from the CCLE set) suggests that the biomarker effectively detects distinct subtypes of melanoma that correspond to sensitivity or resistance to TBK1i (Figure 14L).

To determine if TBK1/IKKε vulnerability was detectable and actionable in heterogeneous melanoma tissues, we used the predictive feature set to stratify a cohort of molecularly annotated patient-derived xenografts (PDX) (Quintana et al., 2012; Quintana et al., 2010; Quintana et al., 2008) and tested the resulting predictions in short-term cultures derived from the corresponding PDX model (Figures 15O and 15P). Positive results, in representative samples, with both BX795 (Figure 15Q) and compound II (Figure 15R), indicated that predictable sensitivity patterns are conserved in this more physiologically relevant model.

Given the activity of TBK1/IKKε inhibition against BRAF wild-type melanoma cells, we considered potential activity in melanoma. We used biomarker signature scores of <-0.1 and >0.1 to assign TCGA uveal melanoma samples into predicted TBK1i-resistant or sensitive cohorts, and found the later was associated with dismal prognosis (Figure 14M). We then ranked a panel of uveal melanoma cell lines using the same metric (Figure 14N). The 2 cell lines (MEL285 and MEL290), with biomarker expression scores predicting sensitivity to TBK1/IKKε inhibition, were the most responsive to both compound II and BX795 (Figures

14O, 14P, 15S and 15T), and non-responsive to MEK inhibition (Figures 15U, 15V); indicated mechanistic conservation of these cell states in cutaneous and uveal melanoma.

TBK1/IKKε-Addiction is Conserved In Vivo and Corresponds to a Cell Autonomous Innate Immune Melanoma Subtype

To test if TBK1/IKKε are targetable in vivo, we first examined the pharmacokinetics (PK) of compound II and BX795 in CD-1 mice. Good aqueous solubility allowed compound II formulation in 100% saline, while BX795 required 10% DMSO and 10% cremophor. Effective peak serum concentrations (Cmax) were achievable with both compounds, however the terminal T1/2 was under 40 minutes for BX795 and just under 3 hours for compound II (Figures 16A and 16B). This indicated that IC_{50}s of compound II, as determined in culture, would be achievable in serum for a maximum of 2 to 3 hours post injection. Wash-out experiments, in cultured cells, suggested that a two-hour exposure to compound II was sufficient to induce significant toxicity over the following 96 hours, which was not the case for BX795 (Figures 16C and 16D). Given this, we elected to proceed with compound II for in vivo testing, and developed an optimized chemical synthesis strategy to provide sufficient material (Figure 17A).

Two intrinsically MAPK pathway inhibitor resistant BRAF(V600E) melanoma cell lines, LOXIMVI and A2058 and a BRAF wild-type melanoma cell line CHL1 were selected for xenograft studies. Upon presentation of palpable tumors, compound II was administered intraperitoneally (IP) daily at 100mg/kg. Despite the poor PK properties of compound II, in

all cases, treatment with compound II significantly reduced growth of these aggressive tumors in mice as compared to the vehicle control (Figures 16E-G). Compound II concentrations in resected tumors (2 hours post last dose) were at or above the IC_{50} (Table 2). Thus TBK1/IKKε inhibition may be a potential strategy for development of therapies to control BRAF- and MEK-inhibitor resistant melanomas.

Recent molecular and pathophysiological annotation of TCGA melanoma samples identified 3 major expression subtypes of melanoma with distinct patient outcomes: immune, keratin and MITF-low (Cancer Genome Atlas, 2015). To evaluate the relationship of these subtypes to predicted TBK1/IKKε addiction, we first ranked the TCGA melanoma tumor cohort based on our biomarker expression score (Figure 16H). Tumors with high lymphocyte infiltration were excluded in order to reduce or eliminate any confounding contribution of immune cells to the quantitative gene expression score. Survival analyses with or without samples with high lymphocyte infiltration returned highly similar patient outcomes, and indicated that the exclusion of tumors with high lymphocyte infiltration did not affect the reported TCGA expression subtype classification (Figures 17C and 17D) or distribution of mutation burden (Figure 17E). We found that the predicted TBK1i-sensitive subtype was significantly enriched within both the immune and MITF-low TCGA-reported subtypes, and de-enriched in the keratin subtype (Figures 16I and 16J). Gene set enrichment analysis (GSEA) comparing samples from the tails of the prediction score distribution (prediction score cutoff <-0.05 and >0.05, Figure 17B) indicated that the predicted BRAFi/MEKi-sensitive subtype is enriched for tyrosine metabolism and oxidative phosphorylation, consistent with active

SOX10 and MITF regulatory programs; whereas the predicted TBK1i sensitive subtype is enriched for toll-like receptor and innate immune signaling (Figures 16K-N). These cumulative observations support the notion that the predicted TBK1i-sensitive subtype is a mechanistically distinct “innate immune” pathway subtype.

TBK1/IKKε Activate AKT and YAP to Support Survival of the Cell-autonomous Immune Melanoma Subtype

Given the canonical participation of TBK1 in the cell autonomous innate immune/host defense signaling response, we evaluated TBK1 signaling in TBK1/IKKε inhibitor resistant versus sensitive subtypes. Accumulation of TBK1 with active site phosphorylation (serine 172) trended higher in the sensitive cohort, in both BRAF(V600) and BRAF wild-type cell lines, as compared to the resistant cohort, and correlated with significant enrichment of interferon stimulated gene (ISG) expression (West et al., 2015), as would be expected downstream of TBK1/IKKε-dependent innate immune pathway activation (Figures 18A-D and 19A). AKT and NF-κB have both been implicated as direct targets of TBK1 survival signaling in cancer cells (Buss et al., 2004; Ou et al., 2011; Pomerantz and Baltimore, 1999). Of interest, AKT activity was far more responsive to inhibition by compound II in the TBK1/IKKε-addicted cell lines (Figure 18B). However, direct chemical inhibition of AKT (MK2206, (Hirai et al., 2010) or the canonical IκB Kinases (IKK1/2, BMS-345541, (Burke et al., 2003)) had limited consequences on cell viability and no selectivity among cell lines tested (Figures 19D and 19E). Moreover, the PI3K inhibitor LY29400 and the PI3K and mTOR dual inhibitor BEZ235 did not display selective toxicity (Figure 19F and 19G)

suggesting that modulation of these pathways is not sufficient to account for the selective toxicity of TBK1/IKKε inhibition. RNAi-mediated or chemical-mediated perturbation of innate immune pathway components upstream and downstream of TBK1 also showed no subtype selective activity (Figure 19B, 19C, 19H).

Of potential mechanistic significance, YAP pathway activation has recently been identified as a BRAFi-resistance mechanism (Lin et al., 2015); and inhibition of YAP activation has been reported upon shRNA-mediated TBK1 depletion (Kim et al., 2013b); and a physical association of TBK1 and Hippo pathway components has been suggested by proximity-mediated ligation assays (Couzens et al., 2013). YAP activity is directly governed by the LATS1/2 tumor suppressor kinases via inhibitory phosphorylation of YAP1 (Hao et al., 2008; Huang et al., 2005). Notably, we found that compound II exposure selectively induced accumulation of activated LATS1 in the TBKi-sensitive cohort, suggesting TBK1 actively suppresses LATS1 in this setting (Figures 18A, 18B and 19A). In addition, epitope-tagged TBK1 immunoprecipitated together with endogenous YAP1 and LATS1, suggesting a physically proximal activation mechanism (Figure 18F). RNAi-mediated depletion of YAP1 and its paralog TAZ greatly impaired the viability of LOXIMVI and CHL1, but was not sufficient to account for TBK1i-induced cytotoxicity for the majority of cell lines (Figure 19J and 19K). In contrast, combining YAP/TAZ depletion with AKT inhibition resulted in significant and selective induction of apoptosis in TBK1/IKKε-addicted cells (Figure 18E). Thus the mechanism of context-specific vulnerability to TBK1/IKKε inhibition is likely the

combinatorial activation of the Hippo tumor suppressor pathway together with suppression of cell survival signaling.

Consistent with observations in TCGA tumor samples (Figure 16K-N), and selective cell autonomous innate immune pathway activation (Figure 18A-C), comparison of the global gene expression profiles between BRAF/MEK-addicted versus TBK1/IKKε-addicted cell lines by GSEA returned pigment biosynthetic process and TCA cycle as enriched in the BRAF/MEK-addicted subtype (Figures 18G and 18H) versus NOD-like receptor signaling pathway and TGFβ signaling as enriched in the TBK1-addicted subtype (Figures 18I and 18J). Of note, PGC1α-associated oxidative phosphorylation is an acquired resistance mechanism observed in response to BRAF/MEK inhibitor exposure (Gopal et al., 2014). Given the contrary de-enrichment of citrate-cycle associated gene expression in the TBK1/IKKε-addicted subtype, that is also resistant to BRAF/MEK inhibition, we measured relative mitochondrial abundance and function in the BRAF/MEK-addicted subtype versus the TBK1/IKKε-addicted subtype. Consistent with the identification of PGC1α as a SOX10 transcriptional target, the majority of TBK1/IKKε-addicted cell lines, which lack detectable SOX10 expression, were also lacking PGC1α expression (Figure 18K and 19L). These lines also displayed reduced mitochondrial DNA content (Figure 18L), and significantly reduced oxygen consumption rates and maximum respiratory capacity as compared to the BRAF/MEK-addicted lines (Figures 18M and 18N). These observations suggest the TBK1/IKKε-addicted "innate immune" subtype is a previously unrecognized, and

mechanistically distinct, molecular subtype of melanoma that is refractory to current targeted therapy (Figure 19M).

Distinct Epigenetic Cell Fate Programs Specify TBK1/IKKε Addiction

The distinct respiratory capacity among the BRAF/MEK-addicted versus TBK1/IKKε-addicted cells prompted us to investigate carbon utilization and cellular metabolite profiles. Stable isotope (^{13}C) tracing, using labeled glucose or glutamine, showed no detectable differences in the fractional contribution of ^{13}C to the downstream pools of TCA cycle intermediates among the cell lines. Lactate secretion was elevated in TBK1i-sensitive relative to TBK1i-resistant cell lines-- consistent with elevated AKT activity and therefore increased glycolytic rates (Figure 21A) in the "innate immune" subtype, however the respiring mitochondria in both subtypes displayed identical carbon utilization profiles. Moreover, exposure to TBK1/IKKε inhibitors did not detectably alter these profiles. By contrast, LC-MS/MS measurements of 141 intracellular metabolites revealed selective reduction of TCA cycle metabolic intermediates (α-ketoglutarate, aconitate and aspartate) in TBK1i-sensitive cells upon compound II exposure for 2 hours (Figure 21B). This was correlated with accumulation of the polyamines putrescine and spermidine, which occurs upon perturbation of mitochondrial utilization of ornithine (Figure 21C). Supporting TCA cycle activity by supplementation with dimethyl α-ketoglutarate significantly reduced compound II induced apoptosis in sensitive cell lines (Figure 21D). Taken together these observations indicate that while TBK1i-sensitive cells have mitochondria that respire "normally", there are fewer of

them, and they are selectively sensitive to compound II exposure as compared to the BRAFi/MEKi-sensitive counterparts (Figure 21C).

Unbiased evaluation of distinct baseline metabolic profiles in TBK1i-sensitive versus TBK1i-resistant cells, by S2N, revealed 1-methylnicotinamide (1-MNA) as the top ranked molecule selectively enriched in the TBK1i-sensitive cell lines (Figures 20A). We considered this to be of potential significance given that 1-MNA production by nicotinamide N-methyltransferase (NNMT) globally inhibits histone methylation potentially by dominant consumption of S-adenosyl methionine (Ulanovskaya et al., 2013). In consequence, NNMT expression results in the accumulation of relaxed chromatin, and is associated with epigenetic remodeling that supports the naïve pluripotent state of human embryonic stem cells (Sperber et al., 2015), and promotes aggressively invasive tumorigenesis in a number of neoplastic disease lineages (Ulanovskaya et al., 2013). Concordant with this relationship, we found NNMT protein expression was exclusively detectable in the TBK1i-sensitive cells, and was associated with global reduction in H3K27 trimethylation (Figure 20B)-- an EZH2-dependent epigenetic mark that otherwise promotes formation of repressive chromatin (Kirmizis et al., 2004). siRNAs targeting NNMT expression selectively reduced viability of the TBK1i-sensitive cell lines, suggesting persistent NNMT activity is apparently required to support this mechanistic subtype (Figure 20C, two-sided unpaired Mann-Whitney test, $P = 0.004$). We considered that inhibition of the H3K27 methyltransferase, EZH2, in TBK1i-resistant cells may generate a regulatory context that mimics NNMT expression and promotes addiction to TBK1/IKKε activity. Remarkably, we found that a 48-hour treatment with two

different EZH2 inhibitors, with chemically distinct modes of action, was sufficient to sensitize 3 of the 4 TBK1i-resistant cell lines to compound II-induced programmed cell death (Figure 20K and Figure 21E).

The above suggested that distinct molecular routes to melanomagenesis can result in at least two distinct regulatory states that specify differential dependence on RAF/MEK versus TBK1/IKKε survival signaling. Though not sufficient to serve as a predictive marker, a major distinguishing molecular feature for BRAF/MEK-addicted versus TBK1/IKKε-addicted subtypes is the selective presence of the lineage-specific transcription factor SOX10. We noted that among the direct gene targets of SOX10, that are suppressed by SOX10 expression, were multiple components of the TGFβ and innate immune regulatory networks (Figures 21F and 21G). Moreover, SOX10 expression indirectly suppressed expression of both NNMT and multiple components of the polycomb repressor complex 2 (which includes EZH2) (Figures 20D and 20E). These observations suggest that loss of SOX10 during neoplastic transformation from the neural crest lineage may account for many of the mechanistic features associated with the "innate immune" melanoma subtype we describe here. We noted that the "innate immune" melanoma lines consistently displayed elevated TGFβ target gene expression, with the exception of the outlier cases that responded poorly to TBK1/IKKε inhibitors (Figure 20F, 20G and Figure 21H). Importantly, compensation with exogenous TGFβ, was sufficient to sensitize these lines to compound II-induced apoptosis (Figure 20J). Unbiased functional signature ontology (FuSiOn) analysis indicated a close mechanistic relationship between TGFBR2 and TBK1 (Figure 21I). We

therefore asked if TBK1 may be TGFβ-responsive. Short-term TGFβ stimulation resulted in a significant accumulation of TBK1 with active site phosphorylation in the otherwise TBK1i-resistant cell lines. However, TBK1 status was unaffected in the TBK1i-sensitive cell lines, consistent with the presence of chronic TGFβ signaling (Figure 20H-I). These observations suggest that the absence of SOX10 may both promote open chromatin and TBK1 activation (via TGFβ signaling)- resulting in a tumorigenic state that is resistant to MEK inhibition but sensitive to TBK1/IKKε inhibition.

Finally, to help evaluate the breadth of the TBK1/IKKε-dependent regulatory network within the "innate-immune" subtype, we performed whole-proteome analysis of compound II-sensitive phosphopeptides in TBKi sensitive versus resistant cells. We employed a 10-plex tandem mass tag (TMT) approach for quantitative evaluation of 4 cell lines (2 compound II-sensitive and 2 compound II-resistant) exposed to carrier or TBK1i for two hours. Approximately 8897 unique phosphopeptides were identified, 2210 of which were TBK1/IKKε responsive in at least one cell line (fold change ≤ 0.5 or ≥ 2). Global comparison of compound II-sensitive events among the 4 lines indicated a close correlation of response specifically between cells of the "innate immune" subtype (Figures 20L and 21J). Among the most discriminatory changes were peptides corresponding to multiple proteins that participate in epigenetic regulation and a mesenchymal phenotype (Figure 20M). Of note, ZEB2 loss of function mutations are associated with a form of Hirschsprung disease that is also associated with SOX10 mutations. The compound II-sensitive phosphorylation site in ZEB2 (S1014) is next to a charge reversal alteration present is the TCGA melanoma cohort

(K1018E), which conceivably mimics phosphorylation. These context-dependent TBK1/IKKε substrates may therefore represent additional mechanistic components of a BRAF/MEK-insensitive melanomagenesis paradigm.

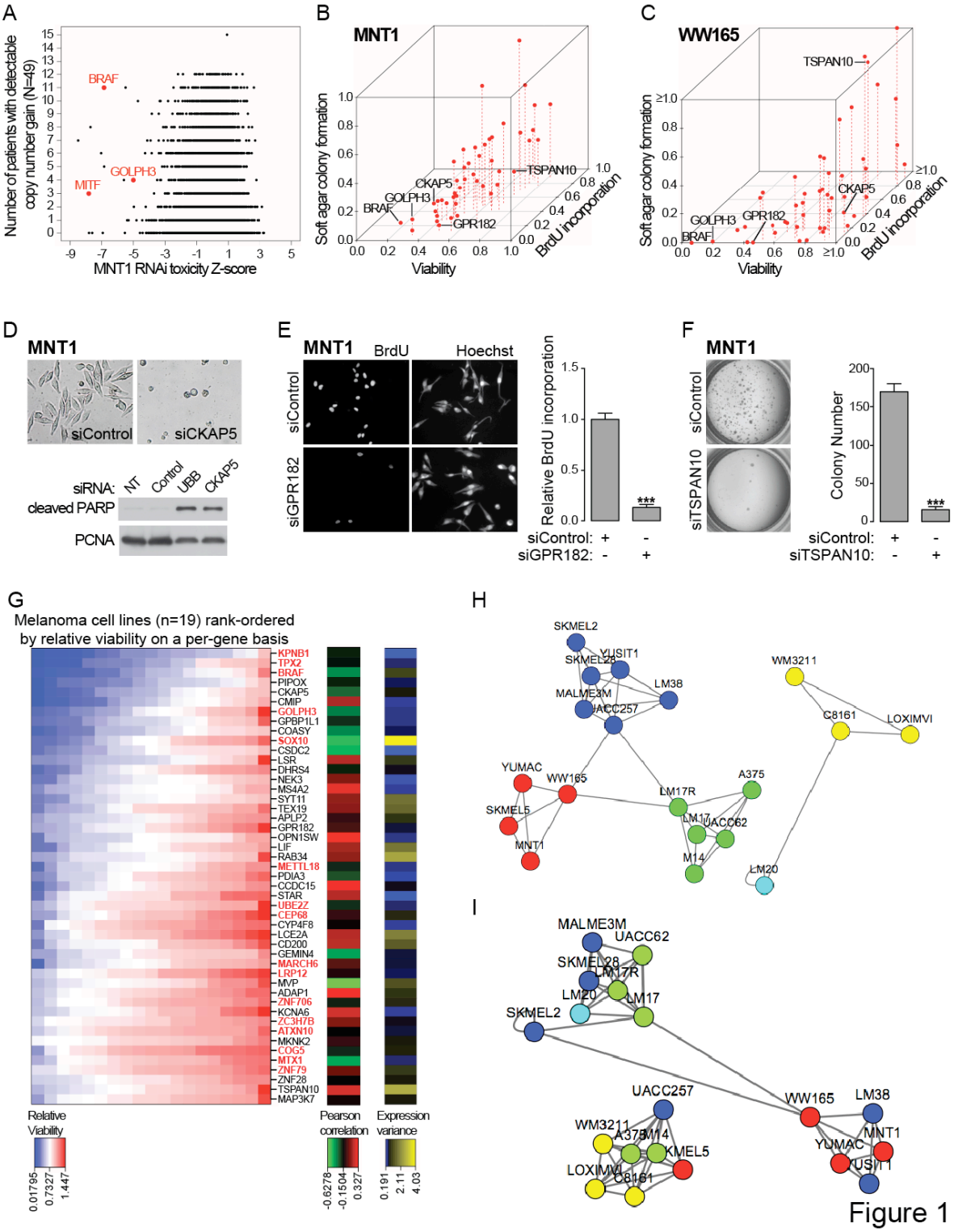
A
Number of patients with detectable copy number gain (N=49)
MNT1 RNAi toxicity Z-score
BRAF
GOLPH3
MITF
B
MNT1
Soft agar colony formation
Viability
BrdU incorporation
TSPAN10
CKAP5
GOLPH3
BRAF
GPR182
C
WW165
TSPAN10
CKAP5
GOLPH3
GPR182
BRAF
D
MNT1
siControl
siCKAP5
siRNA: NT Control UBB CKAP5
cleaved PARP
PCNA
E
MNT1
BrdU
Hoechst
siControl
siGPR182
Relative BrdU incorporation
siControl: + -
siGPR182: - +
F
MNT1
siControl
siTSPAN10
Colony Number
siControl: + -
siTSPAN10: - +
G
Melanoma cell lines (n=19) rank-ordered by relative viability on a per-gene basis
KPNB1
TPX2
BRAF
PIPOX
CKAP5
CMIP
GOLPH3
GPBP1L1
COASY
SOX10
CSDC2
LSR
DHRS4
NEK3
MS4A2
SYT11
TEX19
APLP2
GPR182
OPN1SW
LIF
RAB34
METTL18
PDIA3
CCDC15
STAR
UBE2Z
CEP68
CYP4F8
LCE2A
CD200
GEMIN4
MARCH6
LRP12
MVP
ADAP1
ZNF706
KCNA6
ZC3H7B
ATXN10
MKNK2
COG5
MTX1
ZNF79
ZNF28
TSPAN10
MAP3K7
Relative Viability
Pearson correlation
Expression variance
H
SKMEL2
YUSIT1
SKMEL28
LM38
MALME3M
UACC257
WM3211
C8161
LOXIMVI
YUMAC
WW165
A375
LM17R
SKMEL5
LM17
UACC62
MNT1
M14
LM20
I
MALME3M
UACC62
SKMEL28
LM17R
LM20
LM17
SKMEL2
UACC257
WW165
LM38
WM3211
A375
M14
MNT1
YUMAC
SKMEL5
LOXIMVI
C8161
YUSIT1

Figure 1

Figure 1. Integrative Analysis of Functional Genomics and Copy Number Variation in Melanoma Cells and Tissues

(A) RNAi toxicity screen Z score distributions in MNT1 cells are shown as a function of the copy number variation (CNV) in melanoma tumor samples.

(B-C) 3D plots indicating relative viability (CellTiter Glo assay, x-axis), proliferation (BrdU incorporation, y-axis), and anchorage-independent growth (soft agar colony formation, z-axis) upon depletion of CNV-associated candidate survival genes in MNT1 cells (B) and WW165 cells (C).

(D) Live-cell images and whole cell lysates from MNT1 cells were assessed for the induction of apoptosis 48 hr after transfection with siRNAs targeting LONRF1 (negative control), UBB (positive control) or CKAP5. PCNA was used as a loading control. NT is non-transfected.

(E) Consequence of GPR182 depletion on proliferation, as indicated by BrdU incorporation, in MNT1 cells. Bars indicate mean ± standard deviation (s.d.) (n = 6), ***P < 0.0001, two-sided unpaired Student's t test.

(F) Consequence of TSPAN10 depletion on soft agar colony formation efficiency. Bars indicate mean ± s.d. (n = 3), ***P < 0.0001, two-sided unpaired Student's t test.

(G) Relative viability scores upon depletion of candidate CNV-associated survival genes in each of 19 melanoma cell lines. Correlation of gene expression with sensitivity to gene depletion (middle panel, Pearson correlation coefficient), and gene expression variance across the cell lines (right panel, standard deviation) are shown. Color scales are as indicated in each panel.

(H) Affinity propagation cluster (APC) of melanoma cell lines based on whole-genome transcript profiles (Pearson correlation). Nodes are colored according to cluster membership. (I) APC of melanoma cell lines based on RNAi toxicity profiles (Pearson correlation). Nodes are colored according to cluster membership in the gene expression-based APC (panel H).

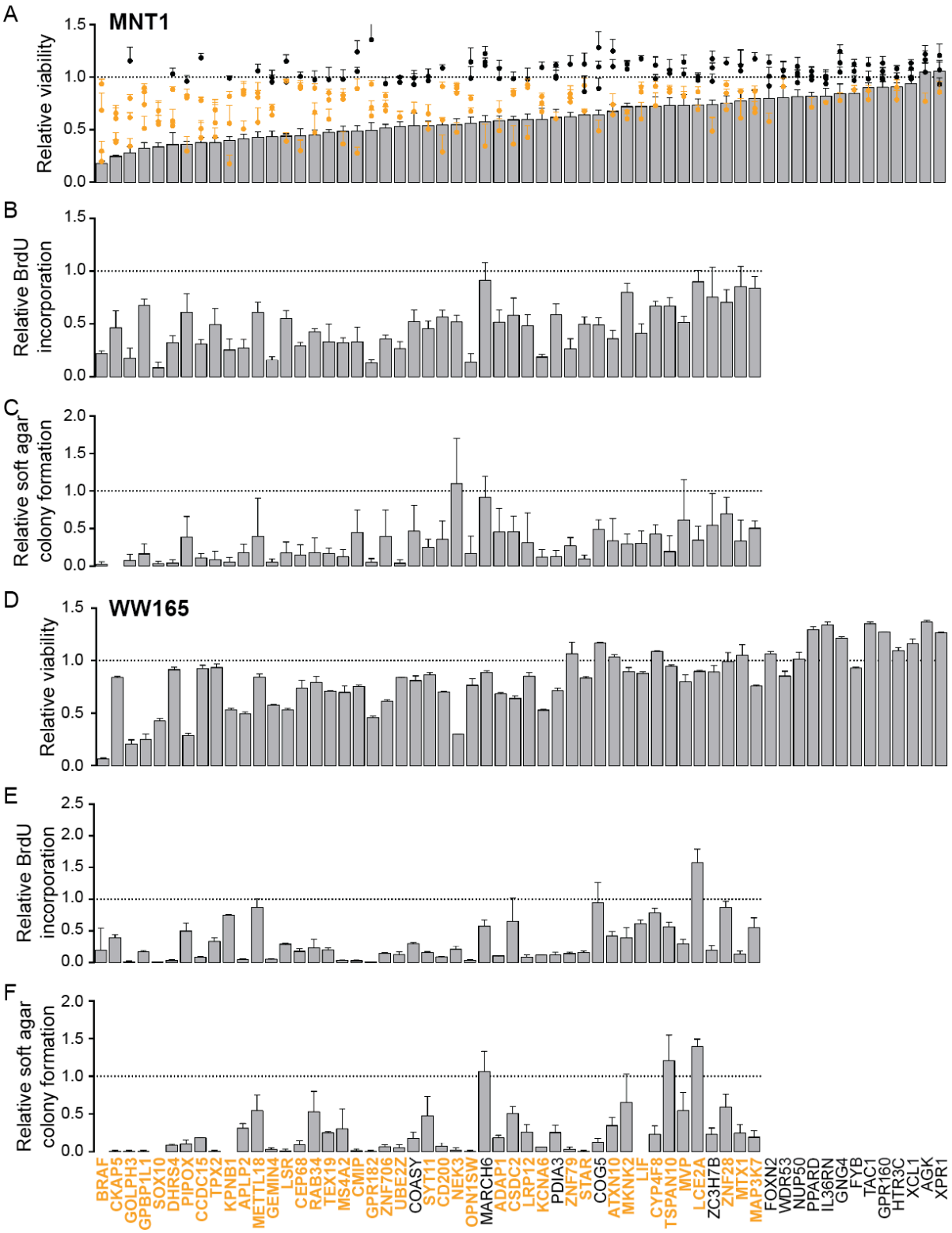
A
MNT1
Relative viability
B
Relative BrdU incorporation
C
Relative soft agar colony formation
D
WW165
Relative viability
E
Relative BrdU incorporation
F
Relative soft agar colony formation
BRAF CKAP5 GOLPH3 GPBP1L1 SOX10 DHRS4 PIPOX CCDC15 TPX2 KPNB1 APLP2 METTL18 GEMIN4 LSR CEP68 RAB34 TEX19 MS4A2 CMIP GPR182 ZNF706 UBE2Z COASY SYT11 CD200 NEK3 OPN1SW MARCH6 ADAP1 CSDC2 LRP12 KCNA6 PDIA3 ZNF79 STAR COG5 ATXN10 MKNK2 LIF CYP4F8 TSPAN10 MVP LCE2A ZC3H7B ZNF28 MTX1 MAP3K7 FOXN2 WDR53 NUP50 PPARD IL36RN GNG4 FYB TAC1 GPR160 HTR3C XCL1 AGK XPR1

Figure 2

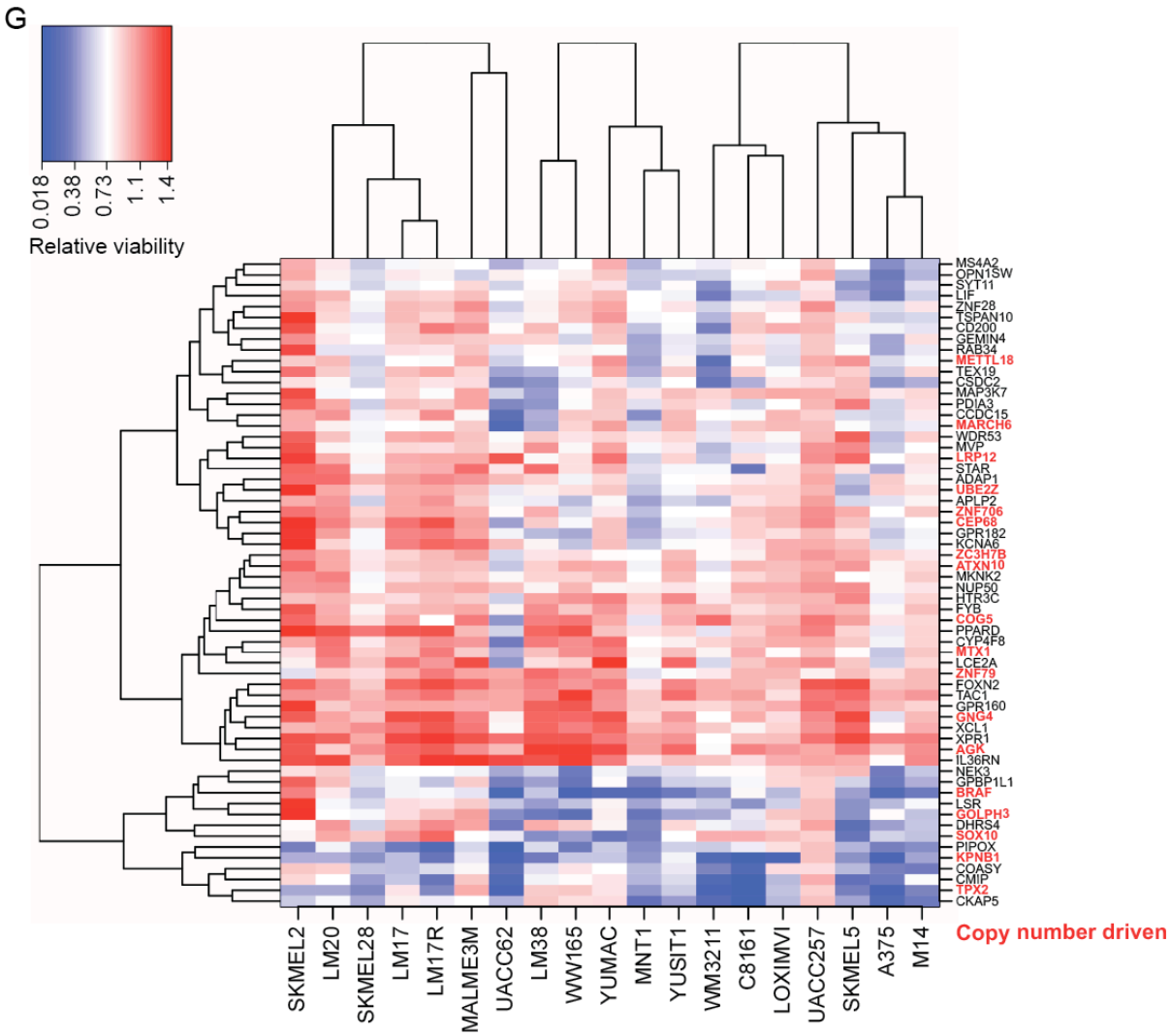

Figure 2 continued

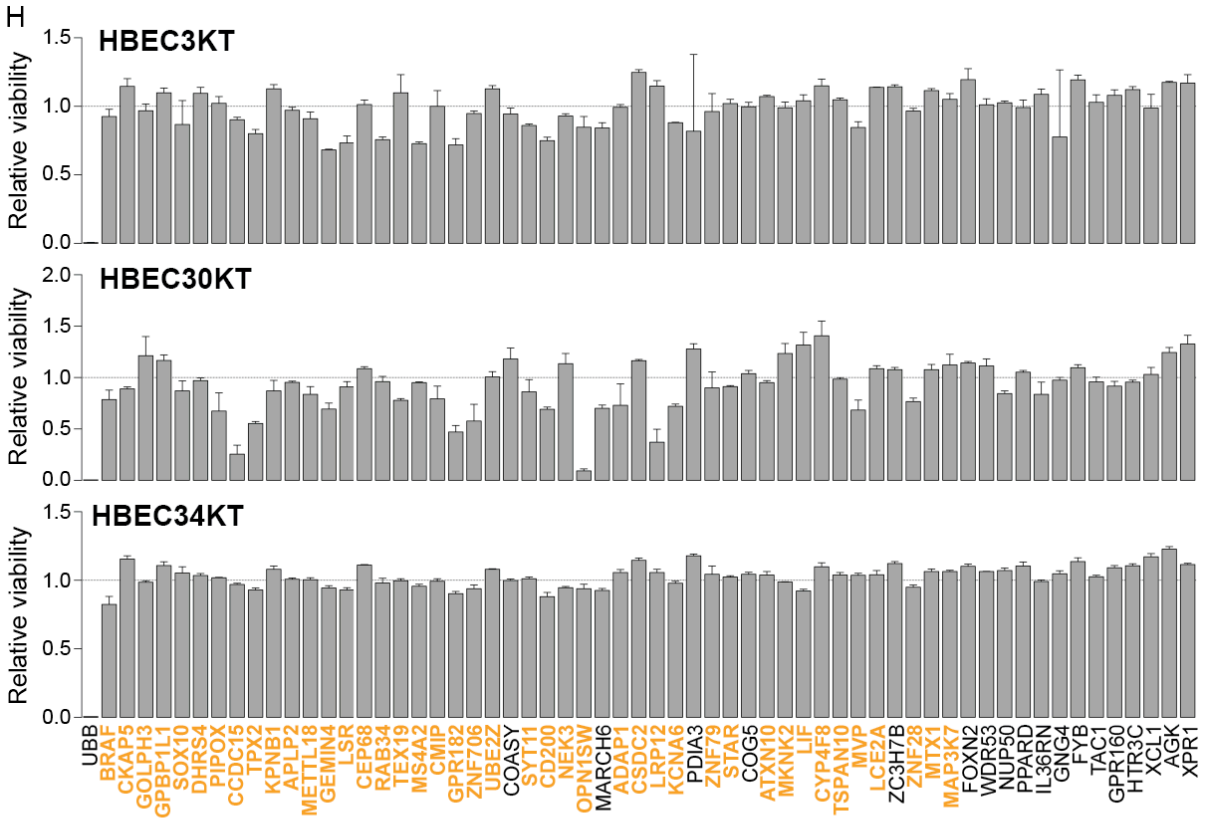

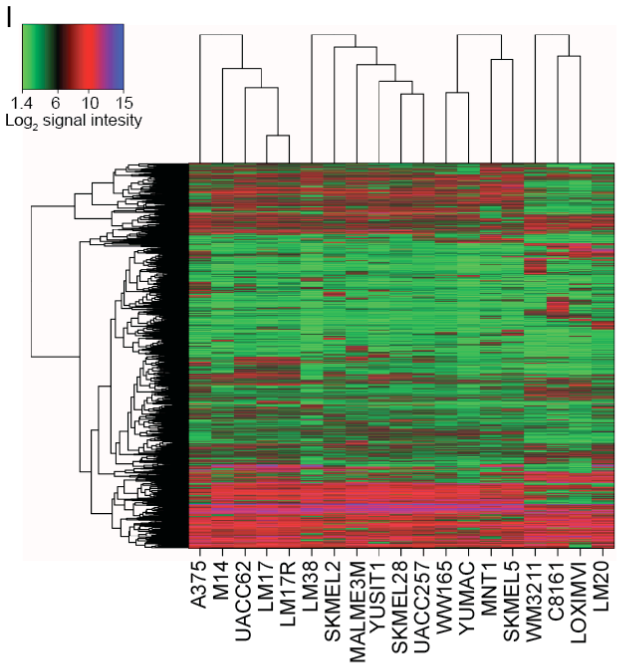

Figure 2 continued

Figure 2. Integrative Analysis of Functional Genomics and Copy Number Variation in Melanoma Cells and Tissues, Related to Figure 1

(A) Retests of candidate CNV-associated survival genes, in MNT1 cells, with independently synthesized siRNAs. Bars indicate relative viability upon transfection of pools of 4 siRNA oligonucleotide pairs. Bars indicate mean ± s.d. (n = 6). Dots indicate relative viability upon transfection with individual siRNA oligonucleotide pairs (4 pairs per gene). Bars indicate mean ± s.d. (n = 6). Orange color indicates significance of toxicity; $P < 0.05$ by two-sided unpaired Student's t test. Corresponding gene targets are labeled at the bottom of panel F. Those with 2 or more siRNAs that significantly decrease viability are indicated in orange.

(B) Consequence of depletion of candidate CNV-associated survival genes on proliferation (BrdU incorporation) in MNT1 cells. Bars indicate mean ± s.d. (n = 6).

(C) Consequence of depletion of candidate CNV-associated survival genes on soft agar colony formation in MNT1 cells. Bars indicate mean ± s.d. (n = 6).

(D) Relative viability of WW165 cells in response to depletion of candidate CNV-associated survival genes. Bars indicate mean ± s.d. (n = 3).

(E) Consequence of depletion of candidate CNV-associated survival genes on proliferation in WW165 cells. Bars indicate mean ± s.d. (n = 3).

(F) Consequence of depletion of candidate CNV-associated survival genes on soft agar colony formation in WW165 cells. Bars indicate mean ± s.d. (n = 3).

(G) Unsupervised hierarchical cluster (Euclidean distance) displaying response to depletion of candidate CNV-associated survival genes in the indicated melanoma cell lines (genes are clustered using unsupervised hierarchical clustering based on Euclidean distance. Columns

are supervised clustered by Pearson correlation based on APC membership). Color scale is as indicated.

(H) Relative viability of HBEC strains in response to depletion of candidate CNV-associated survival genes. Bars indicate mean ± s.d. (n = 3).

(I) Cluster of the melanoma cell lines based on whole-genome transcript profiles. Top varying genes are clustered by unsupervised hierarchical clustering based on Euclidean distance. Columns are supervised clustered by Pearson correlation based on APC membership.

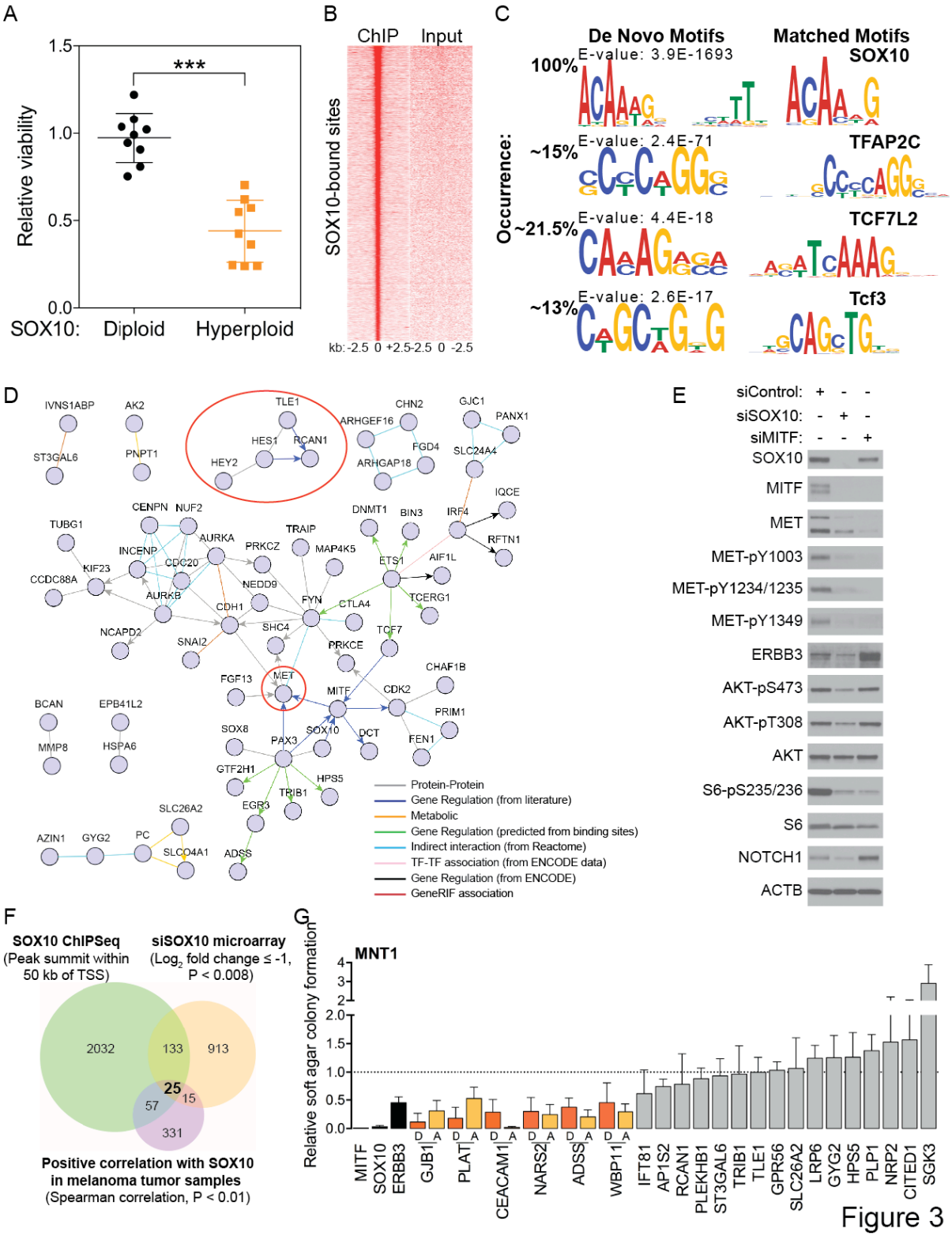
A
Relative viability
1.5
1.0
0.5
0.0
***
SOX10:
Diploid
Hyperploid
B
ChIP
Input
SOX10-bound sites
kb: -2.5 0 +2.5 -2.5 0 -2.5
C
De Novo Motifs
Matched Motifs
Occurrence:
100%
E-value: 3.9E-1693
SOX10
~15%
E-value: 2.4E-71
TFAP2C
~21.5%
E-value: 4.4E-18
TCF7L2
~13%
E-value: 2.6E-17
Tcf3
D
IVNS1ABP
AK2
ST3GAL6
PNPT1
TLE1
HES1
RCAN1
HEY2
CHN2
ARHGEF16
FGD4
ARHGAP18
GJC1
PANX1
SLC24A4
IQCE
IRF4
RFTN1
DNMT1
BIN3
CENPN
NUF2
TUBG1
AURKA
TRAIP
PRKCZ
MAP4K5
INCENP
KIF23
CDC20
CCDC88A
AURKB
NEDD9
ETS1
AIF1L
CDH1
FYN
CTLA4
TCERG1
NCAPD2
SHC4
TCF7
SNAI2
PRKCE
CHAF1B
FGF13
MET
MITF
CDK2
PRIM1
BCAN
EPB41L2
MMP8
HSPA6
SOX8
PAX3
SOX10
DCT
FEN1
GTF2H1
HPS5
TRIB1
EGR3
SLC26A2
AZIN1
GYG2
PC
SLCO4A1
ADSS
Protein-Protein
Gene Regulation (from literature)
Metabolic
Gene Regulation (predicted from binding sites)
Indirect interaction (from Reactome)
TF-TF association (from ENCODE data)
Gene Regulation (from ENCODE)
GeneRIF association
E
siControl: + - -
siSOX10: - + -
siMITF: - - +
SOX10
MITF
MET
MET-pY1003
MET-pY1234/1235
MET-pY1349
ERBB3
AKT-pS473
AKT-pT308
AKT
S6-pS235/236
S6
NOTCH1
ACTB
F
SOX10 ChIPSeq
(Peak summit within 50 kb of TSS)
siSOX10 microarray
(Log2 fold change ≤ -1, P < 0.008)
2032
133
913
25
57
15
331
Positive correlation with SOX10 in melanoma tumor samples
(Spearman correlation, P < 0.01)
G
MNT1
Relative soft agar colony formation
4
3
2
2.0
1.5
1.0
0.5
0.0
D A
MITF
SOX10
ERBB3
GJB1
PLAT
CEACAM1
NARS2
ADSS
WBP11
IFT81
AP1S2
RCAN1
PLEKHB1
ST3GAL6
TRIB1
TLE1
GPR56
SLC26A2
LRP6
GYG2
HPS5
PLP1
NRP2
CITED1
SGK3

Figure 3

Figure 3. The SOX10 Regulatory Network Supporting Cell Autonomous Melanoma Cell Growth and Survival

(A) Consequence of SOX10 depletion in SOX10-diploid versus -hyperploid melanoma cell lines; two-sided unpaired Mann-Whitney test, ***P < 0.0001.

(B) Heatmap indicating read density (reads per base pair per peak) in peak summit regions of SOX10-LAP ChIP versus input.

(C) De novo motifs identified from SOX10 ChIP-Seq (left panel) and matched motifs from TOMTOM (right panel).

(D) First-degree network neighborhood of the gene products of SOX10 targets identified from ChIP-Seq and significantly downregulated in response to SOX10 depletion.

(E) Whole cell lysates of MNT1 cells, 48 hr after transfection with siRNAs targeting LONRF1 (negative control), SOX10 or MITF, were assessed for accumulation of indicated total and phosphorylated proteins by immunoblot.

(F) Euler plot indicating the intersection of genes identified from ChIP-Seq, microarray and patient correlations.

(G) Consequence of highly correlated SOX10 targets (Figure 2F, 25 genes) on soft agar colony formation in MNT1 cells. siRNAs obtained from Ambion are indicated in yellow. All other siRNAs were obtained from Dharmacon (orange, gray and black). Bars indicate mean ± s.d.(n = 3).

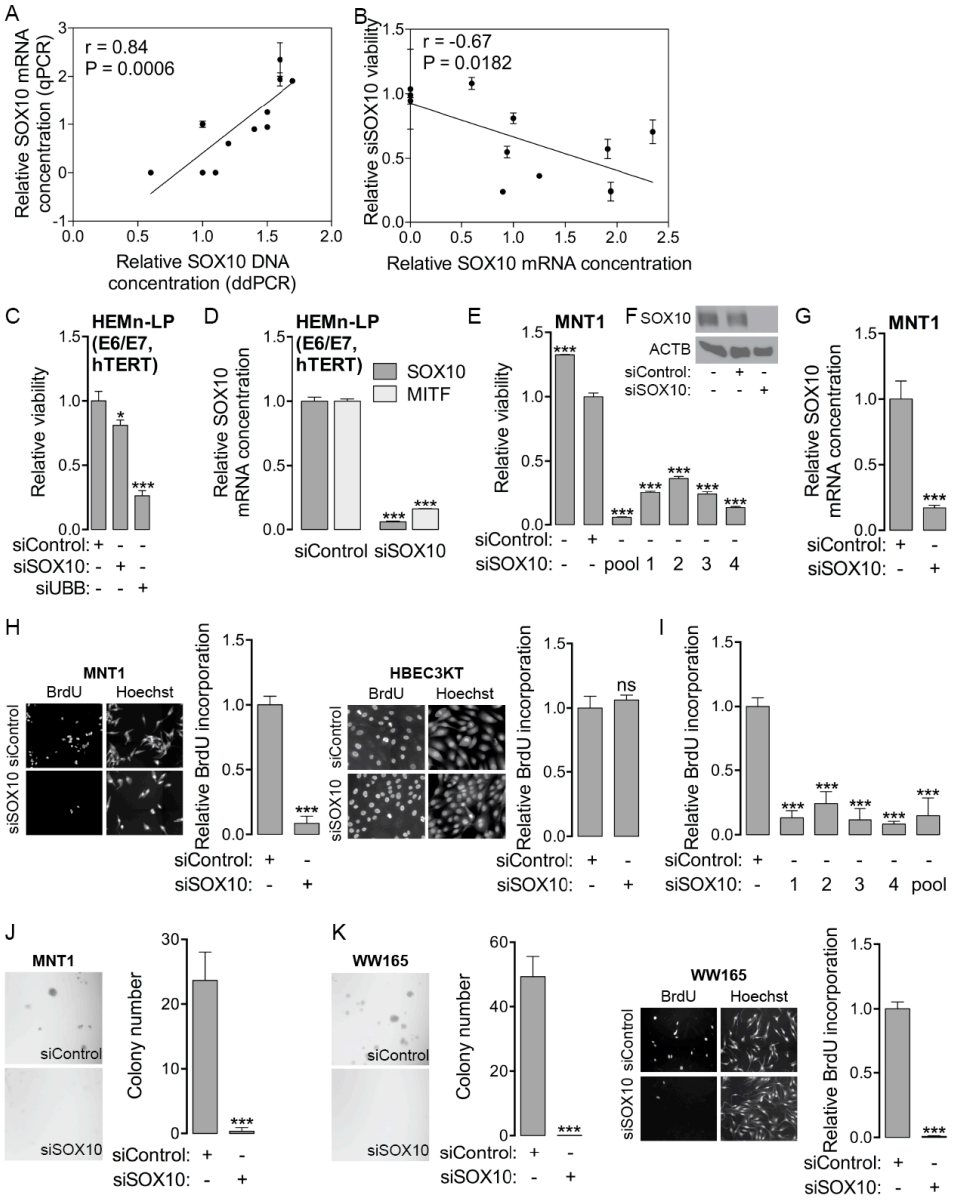
A
Relative SOX10 mRNA concentration (qPCR)
r = 0.84
P = 0.0006
Relative SOX10 DNA concentration (ddPCR)
B
Relative siSOX10 viability
r = -0.67
P = 0.0182
Relative SOX10 mRNA concentration
C
HEMn-LP (E6/E7, hTERT)
Relative viability
siControl: + - -
siSOX10: - + -
siUBB: - - +
D
HEMn-LP (E6/E7, hTERT)
SOX10
MITF
Relative SOX10 mRNA concentration
siControl siSOX10
E
MNT1
Relative viability
siControl: - + - - - - -
siSOX10: - - pool 1 2 3 4
F
SOX10
ACTB
siControl: - + -
siSOX10: - - +
G
MNT1
Relative SOX10 mRNA concentration
siControl: + -
siSOX10: - +
H
MNT1
BrdU
Hoechst
siControl
siSOX10
Relative BrdU incorporation
siControl: + -
siSOX10: - +
HBEC3KT
ns
I
Relative BrdU incorporation
siControl: + - - - - - -
siSOX10: - 1 2 3 4 pool
J
MNT1
siControl
siSOX10
Colony number
siControl: + -
siSOX10: - +
K
WW165
Colony number
WW165
BrdU
Hoechst
Relative BrdU incorporation

Figure 4

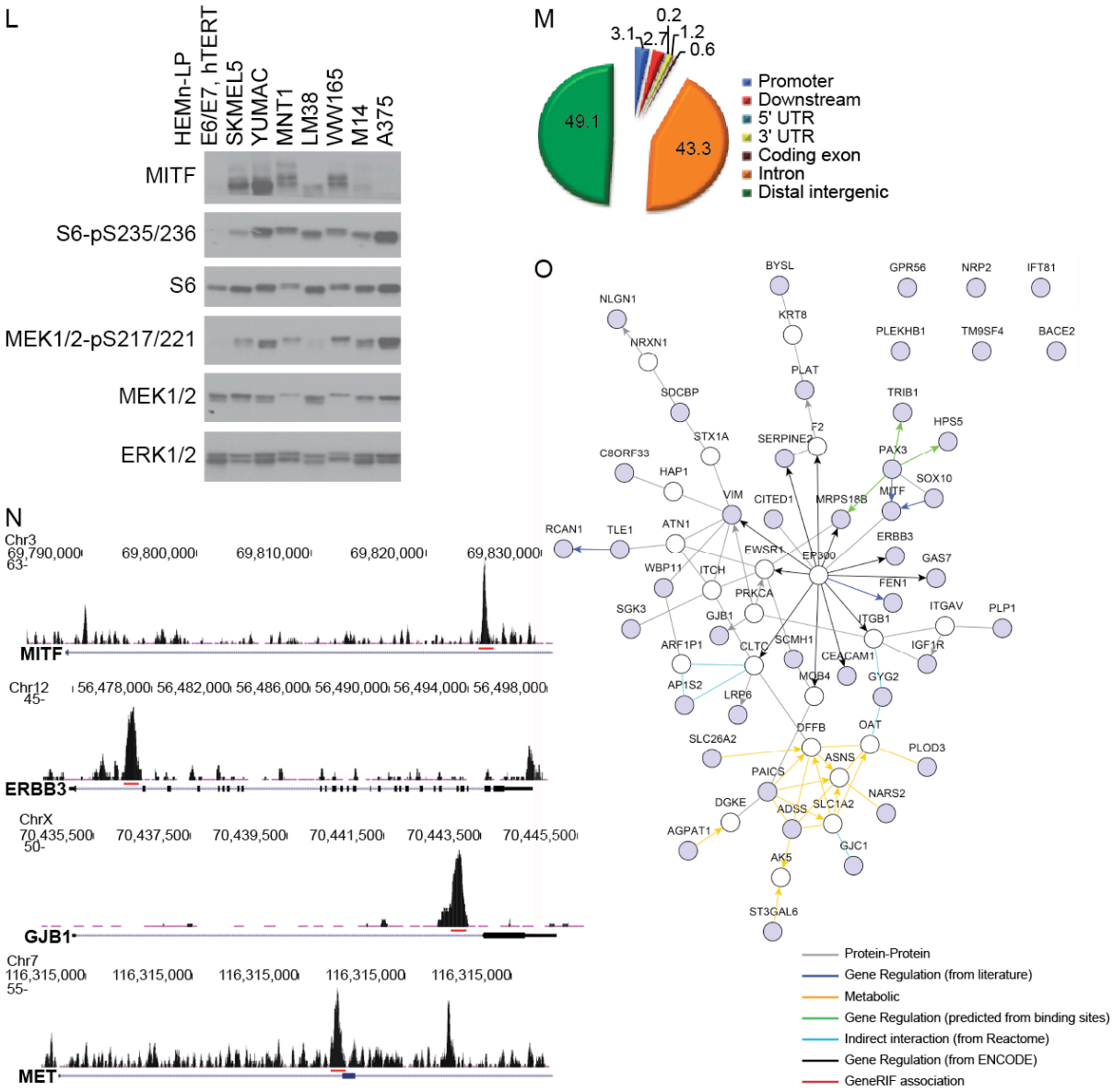

Figure 4 continued

Figure 4. The SOX10 Regulatory Network Supporting Cell Autonomous Melanoma Cell Growth and Survival, Related to Figure 3

(A) Correlation of SOX10 DNA and mRNA concentrations in the melanoma cell line panel. Bars indicate mean ± s.d. (n = 3). P = 0.0006, two-tailed Pearson correlation coefficient.

(B) Correlation of SOX10 mRNA concentrations and sensitivity to SOX10 depletion in the melanoma cell line panel. Bars indicate mean ± s.d. (n = 3). P = 0.0182, two-tailed Pearson correlation coefficient.

(C) Consequence of SOX10 depletion on the viability of immortalized human melanocytes. Bars indicate mean ± s.d. (n = 3). One-way ANOVA followed by Tukey's multiple comparisons test, *P = 0.0122, ***P < 0.0001.

(D) qPCR analysis of SOX10 and MITF mRNA concentrations upon SOX10 depletion in immortalized human melanocytes. Bars indicate mean ± s.d. (n = 3). ***P < 0.0001, two-sided unpaired Student's t test.

(E) Consequence of SOX10 depletion using pooled or individual siRNAs on the viability of MNT1 cells. Bars indicate mean ± s.d. (n = 3). One-way ANOVA followed by Tukey's multiple comparisons test, ***P < 0.0001.

(F) Whole cell lysates assessed for the accumulation of SOX10 protein 48 hr after transfection with siRNAs targeting LONRF1 (negative control) or SOX10 by immunoblotting.

(G) qPCR analysis of SOX10 mRNA concentrations upon SOX10 depletion in MNT1 cells. Bars indicate mean ± s.d. (n = 3). Two-sided unpaired Student's t test, ***P = 0.0005.

(H) Consequence of SOX10 depletion on proliferation as measured by BrdU incorporation in MNT1 and HBEC3KT cells. Bars indicate mean ± s.d. (n = 6, MNT1) (n=3, HBEC3KT). Two-sided unpaired Student's t test, ***P < 0.0001).

(I) Consequence of SOX10 depletion on proliferation in MNT1 cells using pooled or individual siRNAs. Bars indicate mean ± s.d. (n = 3). One-way ANOVA followed by Tukey's multiple comparisons test, ***P < 0.0001.

(J) Consequence of SOX10 depletion on MNT1 soft agar colony formation. Bars indicate mean ± s.d. (n = 3). Two-sided unpaired Student's t test, ***P = 0.0008.

(K) Consequence of SOX10 depletion on WW165 soft agar colony formation and proliferation. Bars indicate mean ± s.d. (n = 3). Two-sided unpaired Student's t test, ***P < 0.0001 (soft agar) and ***P = 0.0002 (BrdU incorporation).

(L) Whole cell lysates were assessed for the accumulation of indicated total and phosphorylated proteins by immunoblot.

(M) Genomic distribution of SOX10 binding sites relative to known protein-coding elements.

(N) Examples of SOX10 ChIP peaks.

(O) First-degree network neighborhood of the gene products in the intersection of ChIP-Seq, microarray and patient correlations. (see Figure 3F, euler plot). (Blue nodes indicate highly correlated SOX10 putative targets and white nodes indicate intermediate connectors).

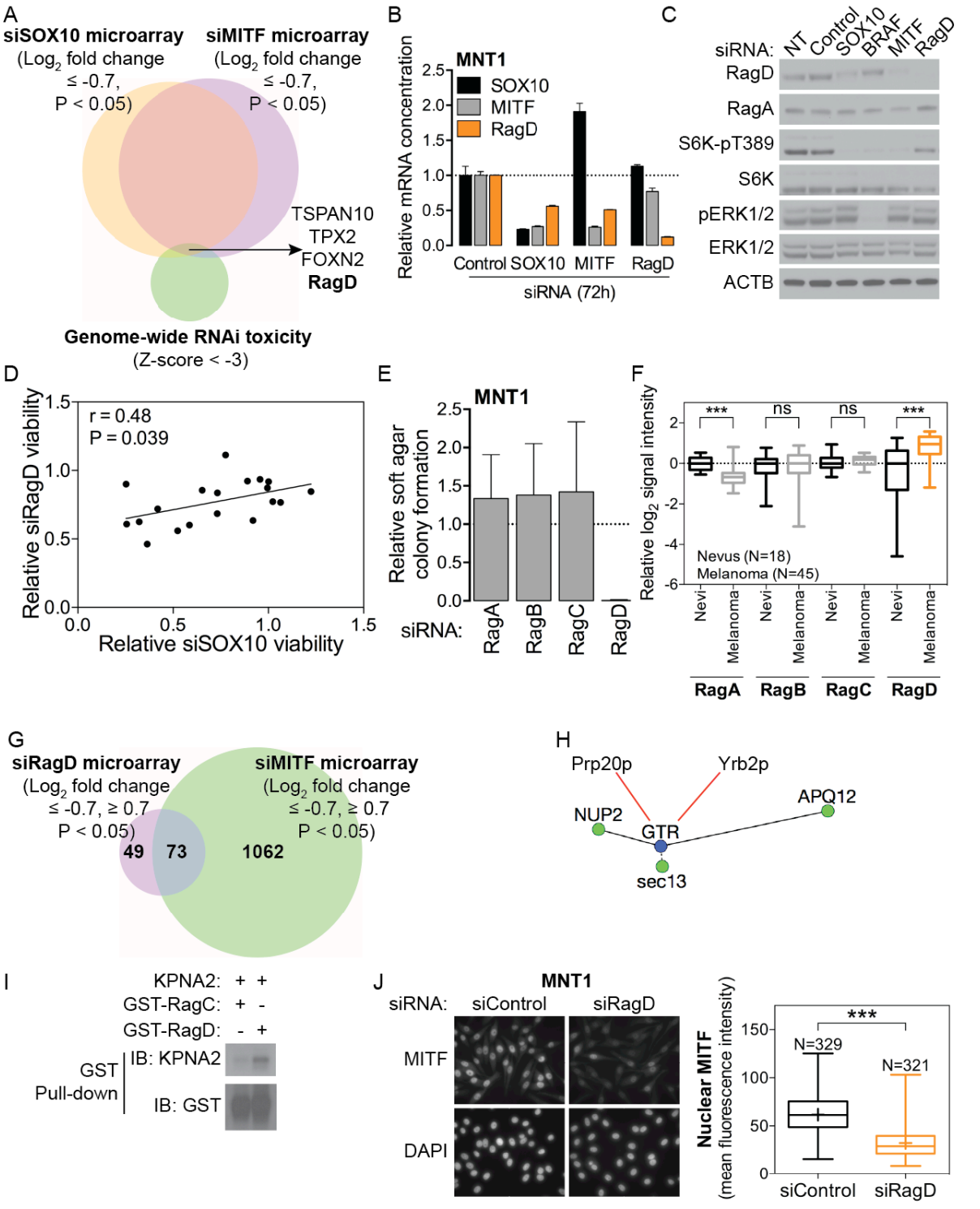
A
siSOX10 microarray
(Log2 fold change
≤ -0.7,
P < 0.05)
siMITF microarray
(Log2 fold change
≤ -0.7,
P < 0.05)
TSPAN10
TPX2
FOXN2
RagD
Genome-wide RNAi toxicity
(Z-score < -3)
B
MNT1
SOX10
MITF
RagD
Relative mRNA concentration
Control SOX10 MITF RagD
siRNA (72h)
C
siRNA: NT Control SOX10 BRAF MITF RagD
RagD
RagA
S6K-pT389
S6K
pERK1/2
ERK1/2
ACTB
D
r = 0.48
P = 0.039
Relative siRagD viability
Relative siSOX10 viability
E
MNT1
Relative soft agar colony formation
siRNA: RagA RagB RagC RagD
F
Relative log2 signal intensity
***
ns
ns
***
Nevus (N=18)
Melanoma (N=45)
Nevi
Melanoma
RagA
RagB
RagC
RagD
G
siRagD microarray
(Log2 fold change
≤ -0.7, ≥ 0.7
P < 0.05)
siMITF microarray
(Log2 fold change
≤ -0.7, ≥ 0.7
P < 0.05)
49
73
1062
H
Prp20p
Yrb2p
APQ12
NUP2
GTR
sec13
I
KPNA2: + +
GST-RagC: + -
GST-RagD: - +
GST Pull-down
IB: KPNA2
IB: GST
J
MNT1
siRNA: siControl siRagD
MITF
DAPI
Nuclear MITF
(mean fluorescence intensity)
***
N=329
N=321
siControl
siRagD

Figure 5

Figure 5. RagD is an MITF Transcriptional Target Gene That Promotes MITF Nuclear Translocation

(A) Euler plot indicating the intersection of genes that were downregulated in response to SOX10 or MITF depletion and genes that, when depleted, significantly reduced viability.

(B) Consequence of LONRF1 (negative control), SOX10, MITF or RagD depletion on SOX10, MITF and RagD mRNA concentrations as measured by qPCR. Bars indicate mean ± s.d. (n = 3).

(C) Whole cell lysates were assessed for the accumulation of indicated total and phosphorylated proteins 72 hr after transfection with siRNAs targeting LONRF1 (negative control), SOX10, BRAF, MITF or RagD.

(D) Correlation of relative viability upon depletion of SOX10 or RagD in 19 melanoma cell lines. P = 0.48, two-tailed Pearson correlation coefficient.

(E) Consequence of RagA, RagB, RagC or RagD depletion on MNT1 soft agar colony formation. Bars indicate mean ± s.d. (n = 3).

(F) Relative expression of Rag family members in melanoma versus nevi; two-sided unpaired Mann-Whitney test, ***P < 0.0001.

(G) Euler plot of genes significantly up- or down- regulated upon RagD or MITF depletion.

(H) GTR genetic interactions with nuclear pore machinery from DRYGIN (black edges) and literature curated physical and functional interactions of GTR with the Ran GTPase cycle in yeast (red edges).

(I) Direct in vitro Rag/KPNA2 interactions using purified recombinant protein.

(J) Consequence of RagD depletion on MITF nuclear accumulation; two-sided unpaired Mann-Whitney test, ***P < 0.0001).

Gene Symbol	Vienna .rho	GSE3189 .rho	GSE8401 .rho	Vienna .P	GSE3189 .P	GSE8401 .P	nSig0 .01	nSig 0.001
SOX10	1	1	1	0	0	0	3	3
RagD	**0.46**	**0.28**	**0.42**	**1.41E-08**	**0.009**	**3.66E-05**	**3**	**2**
RagA	-0.24	-0.02	-0.21	1.00	0.57	0.97	0	0
RagB	0.20	0.30	0.05	0.01	0.01	0.32	2	0
RagC	-0.17	-0.09	-0.09	0.98	0.77	0.79	0	0
MITF	**0.54**	**0.52**	**0.51**	**3.64E-12**	**1.77E-06**	**3.65E-07**	**3**	**3**

- Spearman correlation test with SOX10 expression
- Significantly correlated genes P<0.01 and P<0.001

Table 1. Expression correlation between Rag family members and SOX10 in three different melanoma patient cohorts.

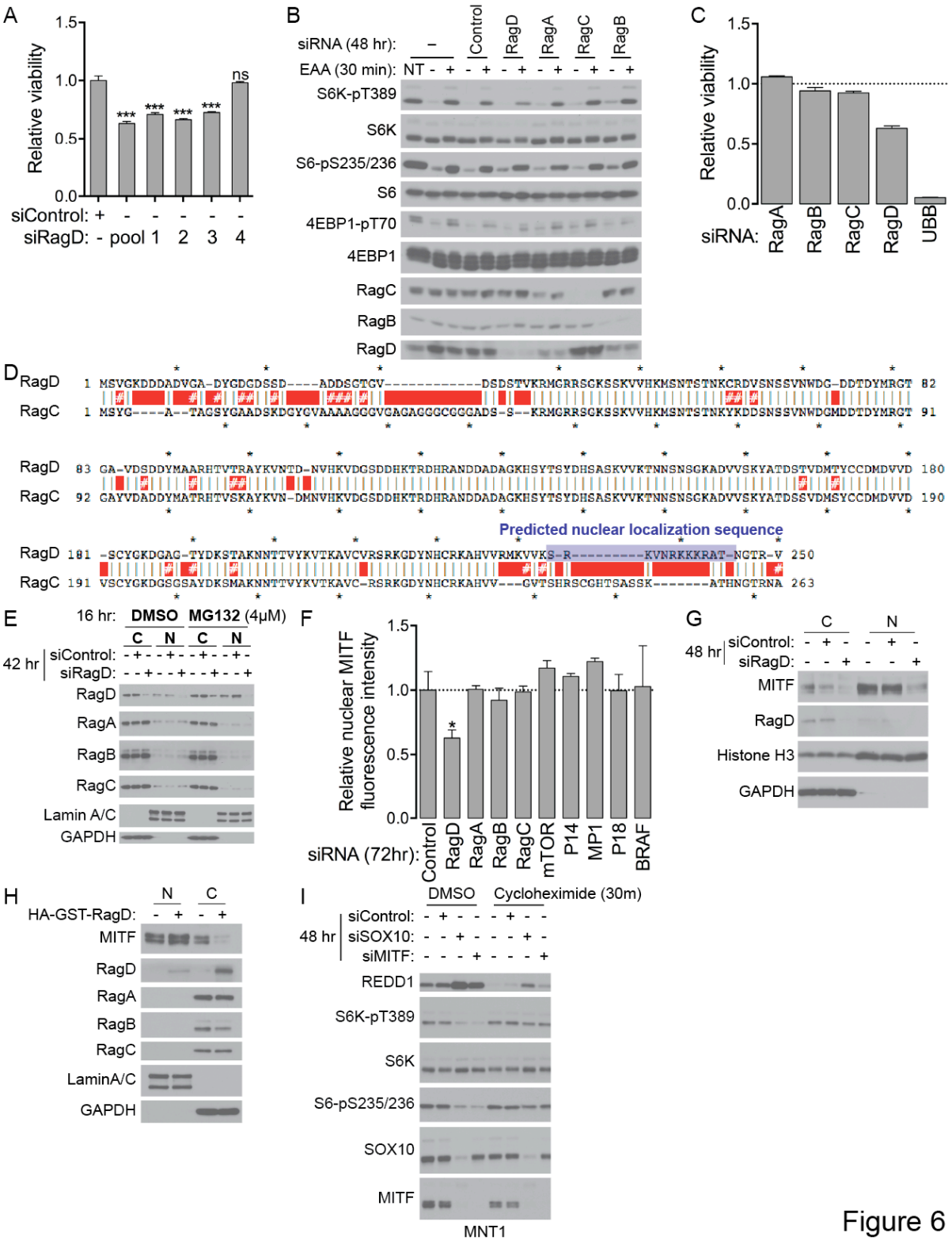
A
Relative viability
siControl: + - - - - -
siRagD: - pool 1 2 3 4
ns
B
siRNA (48 hr): – Control RagD RagA RagC RagB
EAA (30 min): NT - + - + - + - + - + - +
S6K-pT389
S6K
S6-pS235/236
S6
4EBP1-pT70
4EBP1
RagC
RagB
RagD
C
Relative viability
siRNA: RagA RagB RagC RagD UBB
D
RagD
RagC
Predicted nuclear localization sequence
E
16 hr: DMSO MG132 (4μM)
C N C N
42 hr siControl:
siRagD:
RagD
RagA
RagB
RagC
Lamin A/C
GAPDH
F
Relative nuclear MITF fluorescence intensity
siRNA (72hr): Control RagD RagA RagB RagC mTOR P14 MP1 P18 BRAF
G
C N
48 hr siControl:
siRagD:
MITF
RagD
Histone H3
GAPDH
H
N C
HA-GST-RagD:
MITF
RagD
RagA
RagB
RagC
LaminA/C
GAPDH
I
DMSO Cycloheximide (30m)
48 hr siControl:
siSOX10:
siMITF:
REDD1
S6K-pT389
S6K
S6-pS235/236
SOX10
MITF
MNT1

Figure 6

Figure 6. RagD is an MITF Transcriptional Target Gene That Promotes MITF Nuclear Translocation, Related to Figure 5

(A) Relative viability of MNT1 cells in response to RagD depletion using pooled or individual oligos. Bars indicate mean ± s.d. (n = 3). One-way ANOVA followed by Tukey's multiple comparisons test, ***P < 0.0001.

(B) The mTORC1 response to amino acid depletion/repletion was assessed 48 hr after transfection with siRNAs targeting LONRF1 (negative control), RagD, RagA, RagC or RagB.

(C) Consequence of RagA, RagB, RagC, RagD or UBB (positive control) depletion on MNT1 cell viability. Bars indicate mean ± s.d. (n = 3).

(D) Alignment of RagD and RagC amino acid sequences and the predicted nuclear localization sequence on RagD identified by NLS Mapper.

(E) Cytoplasmic and nuclear fractions were assessed for the accumulation of Rag proteins in cells exposed to DMSO or MG132 42 hr after transfection with siRNAs targeting LONRF1 (negative control) or RagD.

(F) Consequence of the depletion of indicated proteins on MITF nuclear signal intensity in MNT1 cells. Bars indicate mean ± s.d. (n = 3). One-way ANOVA followed by Tukey's multiple comparisons test, ***P = 0.0166.

(G) Cytoplasmic and nuclear fractions were assessed for the accumulation of MITF protein 48 hr after transfection with siRNAs targeting LONRF1 (negative control) or RagD.

(H) MNT1 cells were transfected with plasmid encoding RagD (HA-GST-RagD) and nuclear and cytoplasmic fractions were assessed for the accumulation of MITF protein.

(I) Whole cell lysates, exposed to DMSO or cycloheximide for 30m, were assessed for the accumulation of REDD1 and indicated phosphorylated proteins 48 hr after transfection with siRNAs targeting LONRF1 (negative control), SOX10 or MITF.

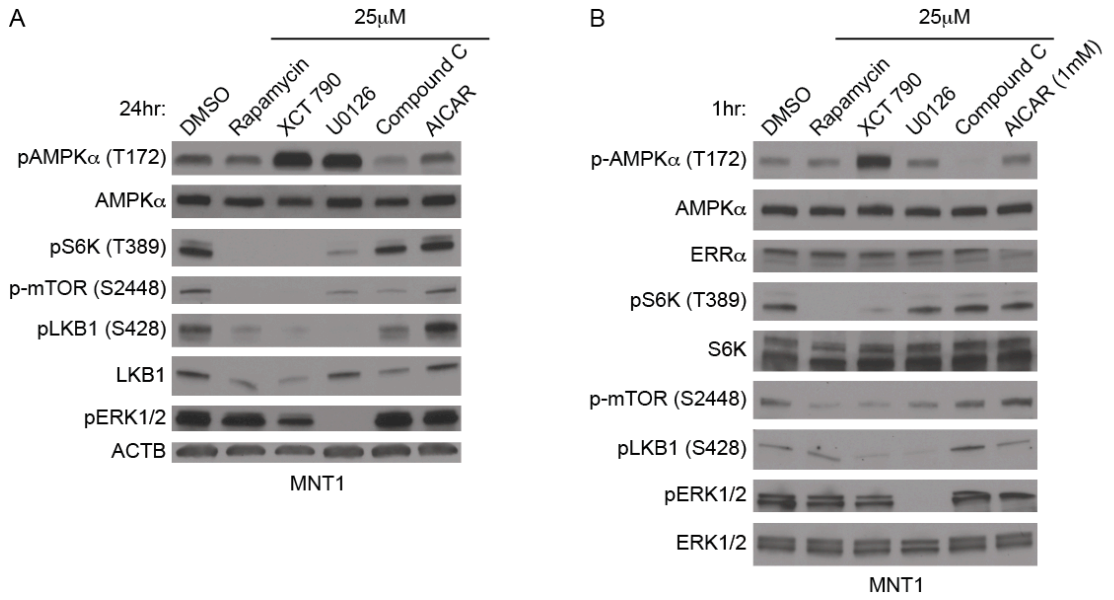

Figure 7

Figure 7. Selective viability and signaling perturbations by XCT 790.

(A) Normalized cell viability of immortalized human colonic epithelial cells and colon cancer cell lines or (B) immortalized human melanocytes and melanoma cell lines 72 hours following exposure to XCT 790 at the indicated doses. Bars indicate mean ± standard deviation, N=3. (C) Population doublings of HEMn-LP, HEMn-LP (CDK4/hTERT) and HEMn-LP (E6/E7/hTERT) cells for the indicated times. (D-E) Whole cell lysates of MNT1 cells, exposed to XCT 790 for 24 hours (D) or 1 hour (E) were assessed for the accumulation of indicated phosphorylated proteins.

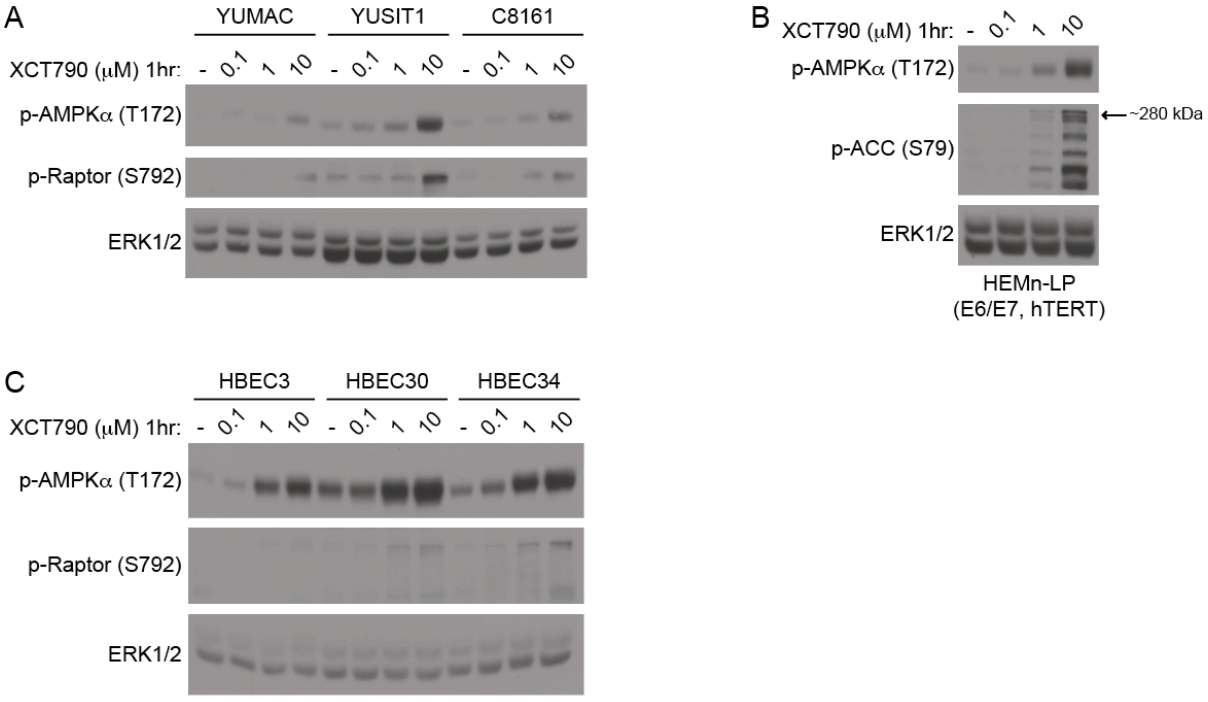

Figure 8

Figure 8. Abrupt AMPK activation is a common response to XCT 790 in both normal and cancer cell lines.

(A-C) Whole cell lysates from melanoma cells (A), immortalized human melanocytes (B) and human bronchial epithelial cells (C) were assessed for accumulation of phosphorylated AMPK and AMPK substrates (phosphorylated Raptor at Ser792(Gwinn et al., 2008) and ACC at Ser79 (Davies et al., 1990)) following exposure to the indicated concentrations of XCT 790.

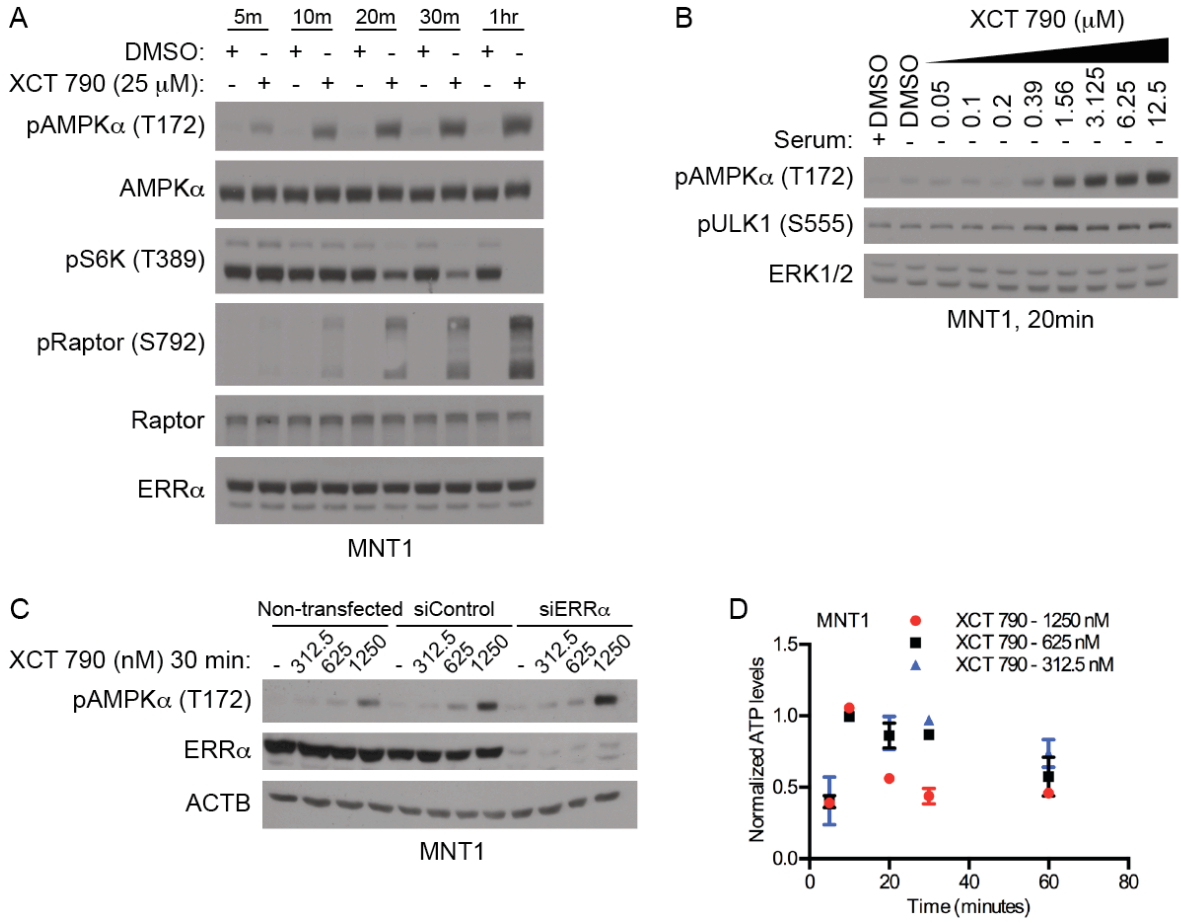

Figure 9

Figure 9. XCT 790 activates AMPK in a dose-dependent and ERRα independent manner. (A) Whole cell lysates from MNT1 cells, exposed to XCT 790 for the indicated times, were assessed for accumulation of the indicated phosphorylated proteins by immunoblot.

(B) AMPK activation was visualized as in (A) following exposure to the indicated concentrations of XCT 790.

(C) The AMPK response to XCT 790 was assessed 72 hours after transfection with siRNAs targeting LONRF1 (negative control) or ERRα.

(D) Normalized ATP levels in MNT1 cells, exposed to XCT 790 for indicated times, as measured by ATP-coupled luciferase assays. Bars indicate mean ± s.d., N=3.

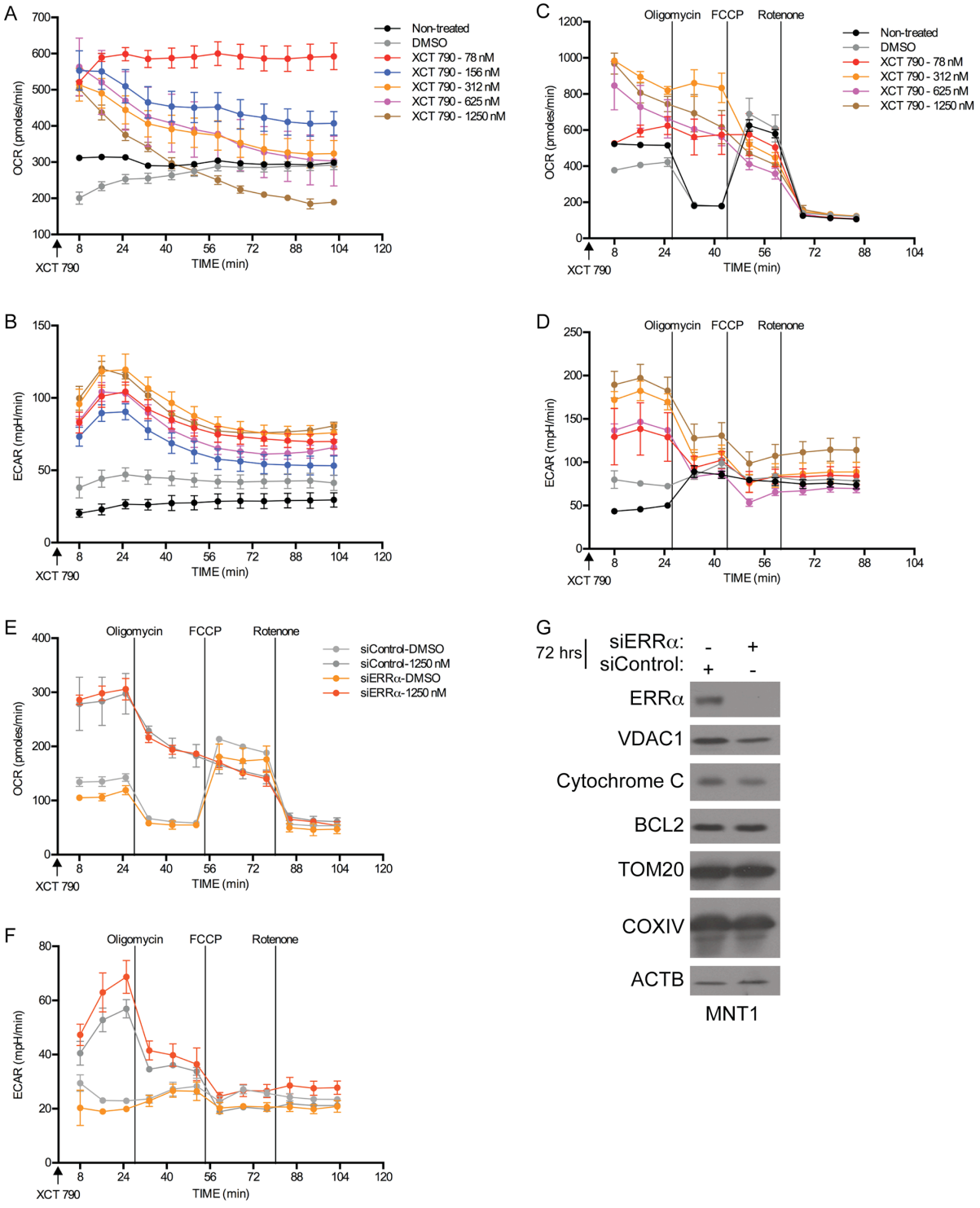
A
OCR (pmoles/min)
TIME (min)
XCT 790
Non-treated
DMSO
XCT 790 - 78 nM
XCT 790 - 156 nM
XCT 790 - 312 nM
XCT 790 - 625 nM
XCT 790 - 1250 nM
C
Oligomycin
FCCP
Rotenone
B
ECAR (mpH/min)
D
E
siControl-DMSO
siControl-1250 nM
siERRα-DMSO
siERRα-1250 nM
F
G
72 hrs
siERRα:
siControl:
ERRα
VDAC1
Cytochrome C
BCL2
TOM20
COXIV
ACTB
MNT1

Figure 10

Figure 10. ERRα-independent perturbation of mitochondrial respiration by XCT 790. (A-D) OCR (A, C) and ECAR (B, D) were measured in MNT1 cells, exposed to XCT 790 at indicated concentrations 8 minutes before the assay, in the absence (A, B) or presence (C, D) of mitochondrial electron transport chain inhibitors. (E-F) OCR (E) and ECAR (F) were measured starting 8 minutes after XCT 790 exposure at the indicated doses. Cells were assayed 72 hours after transfection with the indicated siRNAs. Bars indicate mean ± S.E.M, N=3. (G) Whole cell lysates from cells treated as on (E, F) were assessed for ERRα and representative mitochondrial protein expression by immunoblot.

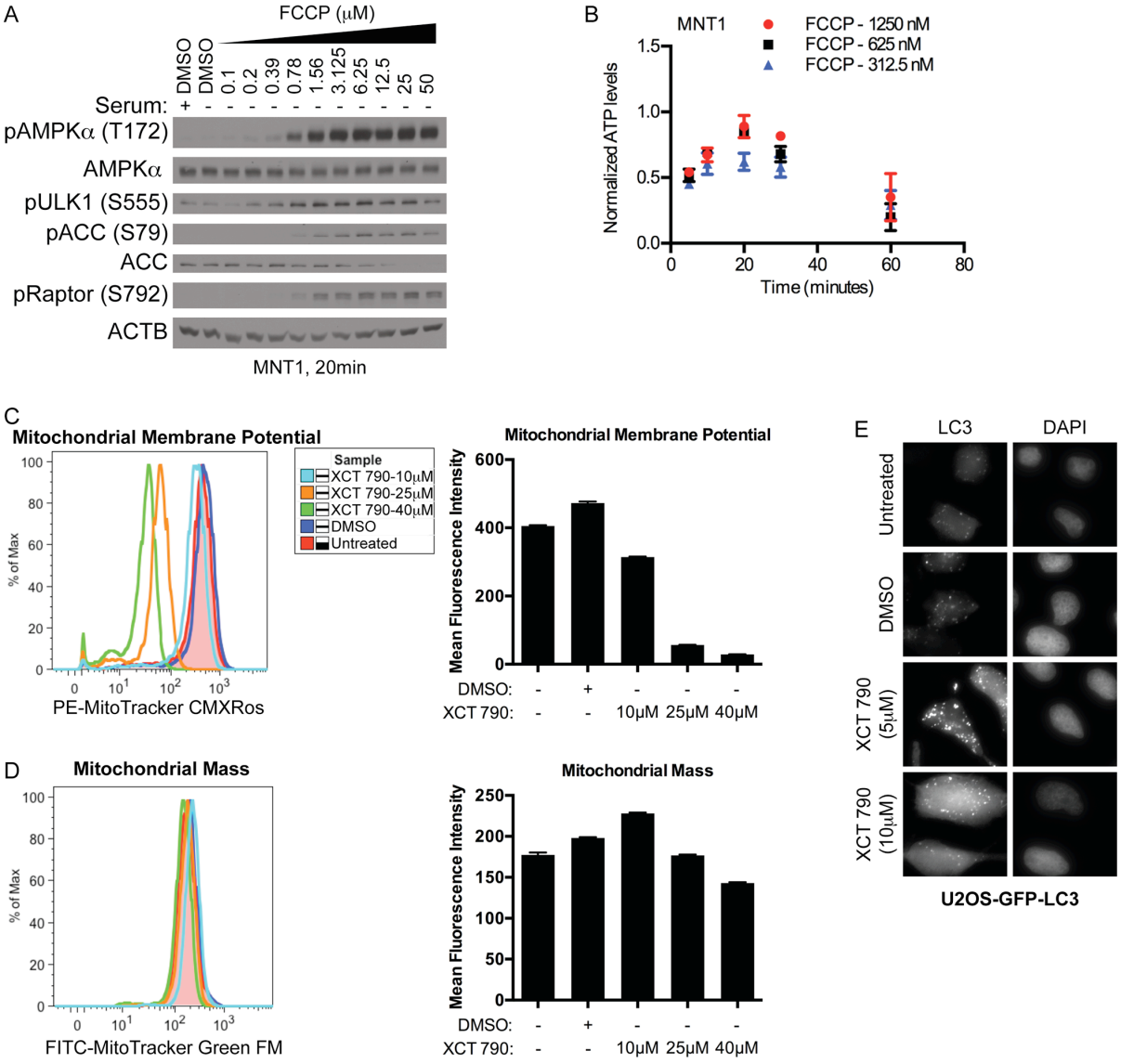
A
FCCP (μM)
DMSO
DMSO
0.1
0.2
0.39
0.78
1.56
3.125
6.25
12.5
25
50
Serum: + - - - - - - - - - - -
pAMPKα (T172)
AMPKα
pULK1 (S555)
pACC (S79)
ACC
pRaptor (S792)
ACTB
MNT1, 20min
B
MNT1
FCCP - 1250 nM
FCCP - 625 nM
FCCP - 312.5 nM
Normalized ATP levels
Time (minutes)
C
Mitochondrial Membrane Potential
Sample
XCT 790-10μM
XCT 790-25μM
XCT 790-40μM
DMSO
Untreated
% of Max
PE-MitoTracker CMXRos
Mitochondrial Membrane Potential
Mean Fluorescence Intensity
DMSO: - + - - -
XCT 790: - - 10μM 25μM 40μM
D
Mitochondrial Mass
% of Max
FITC-MitoTracker Green FM
Mitochondrial Mass
Mean Fluorescence Intensity
DMSO: - + - - -
XCT 790: - - 10μM 25μM 40μM
E
LC3
DAPI
Untreated
DMSO
XCT 790 (5μM)
XCT 790 (10μM)
U2OS-GFP-LC3

Figure 11

Figure 11. XCT 790 is a mitochondrial uncoupler. (A) Consequence of FCCP exposure on AMPK pathway activation was measured as in figure 1A, B. (B) Normalized ATP levels in MNT1 cells, exposed to FCCP for indicated times, as measured by ATP-coupled luciferase assays. Bars indicate mean ± s.d., N=3. (C-D) Mitochondrial membrane potential (C) and mass (D) was measured by FACS in MNT1 cells, treated with XCT 790 for 30 min, using mitochondrial dyes MitoTracker CMXRos and MitoTracker Green FM, respectively. Bar graphs indicate the mean and standard deviation of triplicates. (E) Representative micrographs of U2OS-GFP-LC3 cells treated with XCT 790 or carrier at indicated concentrations for 24 hours.

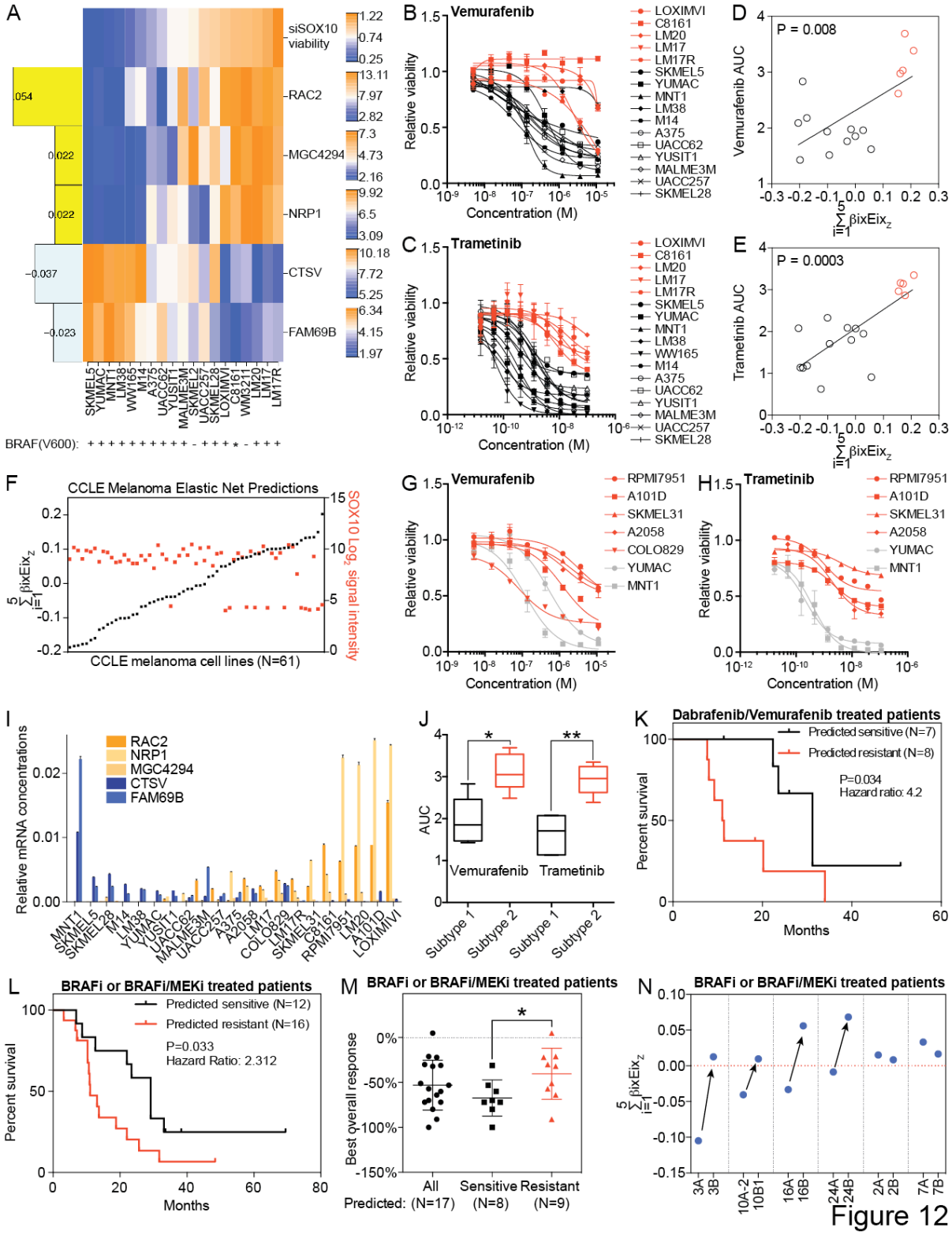
A
siSOX10 viability
RAC2
MGC4294
NRP1
CTSV
FAM69B
BRAF(V600):
B
Vemurafenib
Relative viability
Concentration (M)
C
Trametinib
D
P = 0.008
Vemurafenib AUC
E
P = 0.0003
Trametinib AUC
F
CCLE Melanoma Elastic Net Predictions
CCLE melanoma cell lines (N=61)
SOX10 Log2 signal intensity
G
Vemurafenib
H
Trametinib
I
Relative mRNA concentrations
J
AUC
Vemurafenib
Trametinib
Subtype 1
Subtype 2
K
Dabrafenib/Vemurafenib treated patients
Predicted sensitive (N=7)
Predicted resistant (N=8)
P=0.034
Hazard ratio: 4.2
Percent survival
Months
L
BRAFi or BRAFi/MEKi treated patients
Predicted sensitive (N=12)
Predicted resistant (N=16)
P=0.033
Hazard Ratio: 2.312
M
BRAFi or BRAFi/MEKi treated patients
Best overall response
All
Sensitive
Resistant
Predicted: (N=17) (N=8) (N=9)
N
BRAFi or BRAFi/MEKi treated patients

Figure 12

Figure 12. SOX10 Addiction Specifies Sensitivity of BRAF Mutant Melanomas to BRAF and MEK Inhibitors In Vitro and in Patients

(A) A sparse linear regression model (elastic net) for weighted expression features that specify SOX10 dependence or independence. siRNA response is indicated as a heat map (top row). The central heat map indicates predictive gene expression features (values are $\log_2$) across the indicated cell lines. Bar plot on the left indicates the average weight for the corresponding feature as determined from a 100X bootstrapping analysis.

(B-C) Vemurafenib (B) and trametinib (C) dose-response curves for SOX10-dependent (black) and independent (red) cell lines. Dots indicate mean ± s.d. (n = 3).

(D-E) Linear regression analysis of vemurafenib (D) and trametinib (E) area under the curve values for each cell line in the melanoma panel and the prediction scores determined using a summed weight metric based on the elastic net derived expression features.

(F) Distribution of Cancer Cell Line Encyclopedia (CCLE) melanoma cell lines based on the linear weighted sums of the individual gene expression values for each predictive feature (left y-axis) and the corresponding SOX10 $\log_2$ signal intensity values from microarray is also shown (right y-axis).

(G-H) Vemurafenib (G) and trametinib (H) dose-response curves for predicted targeted therapy resistant melanoma cell lines (red) and the previously tested targeted therapy sensitive cell lines (gray- as comparison).

(I) qPCR analysis of RAC2, NRP1, MGC4294, CTSV and FAM69B mRNA concentrations in melanoma cells. Bars indicate mean ± s.d. (n = 3).

(J) Comparison of area under the curve values for dose response curves from predicted targeted therapy sensitive (subtype 1) and resistant (subtype 2) melanoma cell lines exposed to vemurafenib (two-sided unpaired Mann-Whitney test *P = 0.0159) and trametinib (two-sided unpaired Mann-Whitney test **P = 0.0079).

(K) Kaplan-Meier plot of the overall survival of predicted targeted therapy sensitive and resistant dabrafenib/vemurafenib treated melanoma patients (Rizos et al.). Statistical significance was assessed using the Log-rank (Mantel-Cox) test.

(L) Kaplan-Meier plot of the overall survival of predicted targeted therapy sensitive and resistant vemurafenib or dabrafenib/trametinib treated melanoma patients (Long dataset). Statistical significance was assessed using the Log-rank (Mantel-Cox) test.

(M) Best overall response of predicted targeted therapy sensitive and resistant vemurafenib or dabrafenib/trametinib treated melanoma patients (Hugo et al.) (Two-sided unpaired Mann-Whitney test *P = 0.0339).

(N) Prediction scores of patient tumors isolated before (3A, 10A-2, 16A, 24A, 2A and 7A) and on targeted therapy (vemurafenib or dabrafenib/trametinib) (3B, 10B-1, 16B, 24B, 2B and 7B). Same numbers indicate tumors from same patients.

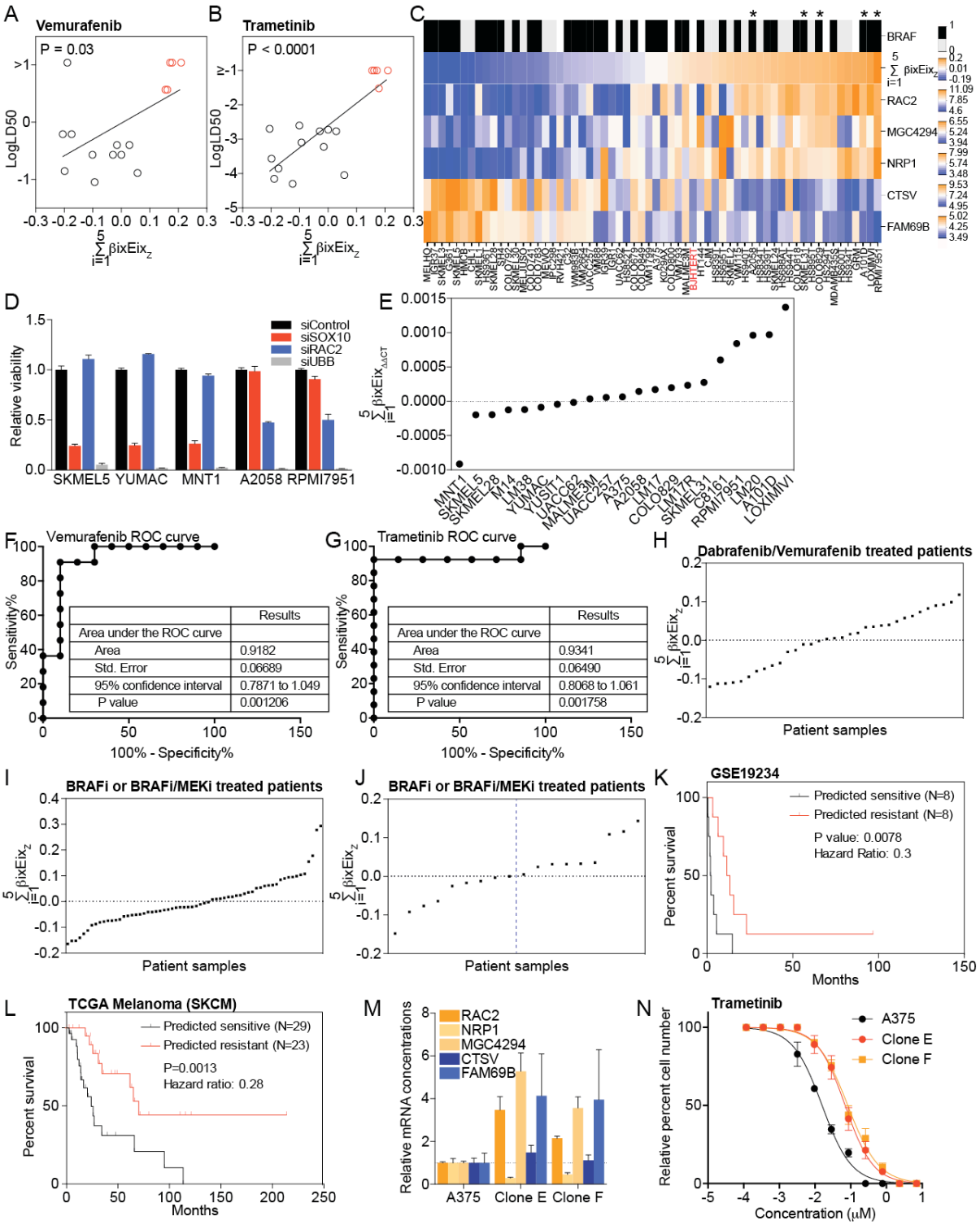
A
Vemurafenib
P = 0.03
LogLD50
B
Trametinib
P < 0.0001
LogLD50
C
BRAF
RAC2
MGC4294
NRP1
CTSV
FAM69B
D
Relative viability
siControl
siSOX10
siRAC2
siUBB
SKMEL5 YUMAC MNT1 A2058 RPMI7951
E
MNT1
SKMEL5
SKMEL28
M14
LM38
YUMAC
YUSIT1
UACC62
MALME3M
UACC257
A375
A2058
LM17
COLO829
LM17R
SKMEL31
C8161
RPMI7951
LM20
A101D
LOXIMVI
F
Vemurafenib ROC curve
Sensitivity%
100% - Specificity%
Area under the ROC curve 0.9182
Std. Error 0.06689
95% confidence interval 0.7871 to 1.049
P value 0.001206
G
Trametinib ROC curve
Sensitivity%
100% - Specificity%
Area under the ROC curve 0.9341
Std. Error 0.06490
95% confidence interval 0.8068 to 1.061
P value 0.001758
H
Dabrafenib/Vemurafenib treated patients
Patient samples
I
BRAFi or BRAFi/MEKi treated patients
Patient samples
J
BRAFi or BRAFi/MEKi treated patients
Patient samples
K
GSE19234
Predicted sensitive (N=8)
Predicted resistant (N=8)
P value: 0.0078
Hazard Ratio: 0.3
Percent survival
Months
L
TCGA Melanoma (SKCM)
Predicted sensitive (N=29)
Predicted resistant (N=23)
P=0.0013
Hazard ratio: 0.28
Percent survival
Months
M
RAC2
NRP1
MGC4294
CTSV
FAM69B
Relative mRNA concentrations
A375 Clone E Clone F
N
Trametinib
A375
Clone E
Clone F
Relative percent cell number
Concentration (μM)

Figure 13

Figure 13. SOX10 Addiction Specifies Sensitivity of BRAF Mutant Melanomas to BRAF and MEK Inhibitors In Vitro and in Patients, Related to Figure 12

(A-B) Linear regression analysis of vemurafenib (D) and trametinib (E) LD50 values for each cell line in the melanoma panel and the prediction scores determined using a summed weight metric based on the elastic net derived expression features.

(C) Biomarker behavior in the CCLE melanoma cell lines. Top row indicates prediction score. Subsequent rows indicate $\log_2$ normalized expression of the indicated genes.

(D) Consequences of SOX10 or RAC2 depletion in SOX10-dependent and newly predicted SOX10-independent melanoma cell lines. Bars indicate mean ± s.d. (n = 3).

(E) Distribution of melanoma cell lines based on the linear weighted sums of the individual gene expression values for each predictive feature measured by qPCR.

(F-G) ROC curve analysis for vemurafenib (F) and trametinib (G) response.

(H-J) Distribution of melanoma tumors resected from patients undergoing BRAFi or BRAFi/MEKi therapy in Rizos et al. (H), Long dataset (I) and Hugo et al. (blue dashed line is the dichotomization boundary) (J) based on the linear weighted sums of the individual gene expression values for each predictive feature.

(K-L) Kaplan-Meier plot of the overall survival of predicted targeted therapy sensitive and resistant melanoma patients in Jonsson et al. (K) and TCGA SKCM (L). Statistical significance was assessed using the Log-rank (Mantel-Cox) test.

(M) qPCR analysis of RAC2, NRP1, MGC4294, CTSV and FAM69B mRNA concentrations in A375 MEKi resistant melanoma clones. Bars indicate mean ± s.d. (n = 3).

(N) Trametinib dose-response curves for A375 parental cells and A375 MEKi resistant clones. Dots indicate mean ± s.d. (n = 3).

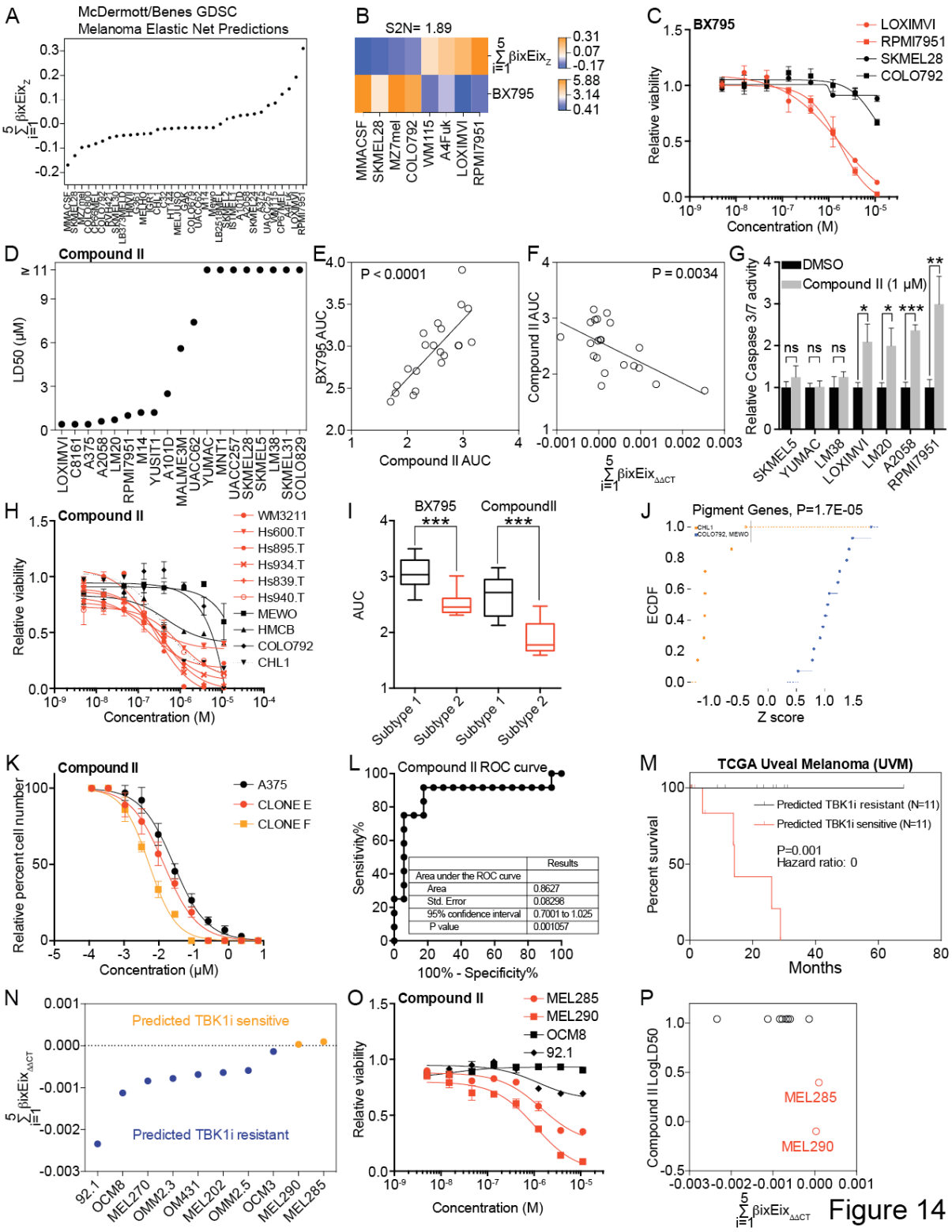
A
McDermott/Benes GDSC
Melanoma Elastic Net Predictions
B
S2N= 1.89
BX795
MMACSF
SKMEL28
MZ7mel
COLO792
WM115
A4Fuk
LOXIMVI
RPMI7951
C
BX795
LOXIMVI
RPMI7951
SKMEL28
COLO792
Relative viability
Concentration (M)
D
Compound II
LD50 (μM)
E
P < 0.0001
BX795 AUC
Compound II AUC
F
P = 0.0034
Compound II AUC
G
DMSO
Compound II (1 μM)
Relative Caspase 3/7 activity
ns
SKMEL5
YUMAC
LM38
LOXIMVI
LM20
A2058
RPMI7951
H
Compound II
WM3211
Hs600.T
Hs895.T
Hs934.T
Hs839.T
Hs940.T
MEWO
HMCB
COLO792
CHL1
Relative viability
Concentration (M)
I
BX795
CompoundII
AUC
Subtype 1
Subtype 2
J
Pigment Genes, P=1.7E-05
ECDF
Z score
K
Compound II
A375
CLONE E
CLONE F
Relative percent cell number
Concentration (μM)
L
Compound II ROC curve
Sensitivity%
100% - Specificity%
Area under the ROC curve
Area
0.8627
Std. Error
0.06298
95% confidence interval
0.7001 to 1.025
P value
0.001057
M
TCGA Uveal Melanoma (UVM)
Predicted TBK1i resistant (N=11)
Predicted TBK1i sensitive (N=11)
P=0.001
Hazard ratio: 0
Percent survival
Months
N
Predicted TBK1i sensitive
Predicted TBK1i resistant
92.1
OCM8
MEL270
OMM2.3
OM431
MEL202
OMM2.5
OCM3
MEL290
MEL285
O
Compound II
MEL285
MEL290
OCM8
92.1
Relative viability
Concentration (M)
P
Compound II LogLD50
MEL285
MEL290

Figure 14

Figure 14. Nomination of TBK1 as a Therapeutic Target for Drug-Resistant Melanoma

(A) Distribution of 35 melanoma cell lines based on the linear weighted sums of the individual expression values for each predictive feature.

(B) S2N ratios identify BX795 IC50s as corresponding to selective activity against predicted drug-resistant melanoma. Top row indicates prediction score. Second row indicates real and imputed IC50s ($\log_{10}$ mM) for BX795 toxicity in the indicated cell lines.

(C) BX795 dose-response curves for cell lines in Figure 14B.

(D) Compound II LD50 values in the melanoma panel.

(E) Linear regression analysis of BX795 and compound II AUC values for each cell line in the melanoma panel.

(F) Linear regression analysis of compound II AUC values for each cell line in the melanoma panel and the prediction scores determined using a summed weight metric based on the elastic net derived expression features.

(G) Caspase-3 and -7 activity was measured following exposure of TBK1 inhibitor sensitive and resistant cell lines to DMSO or compound II (1mM) for 24 hours. Bars indicate mean ± s.d. (n = 3). *P = 0.0132 (LOXIMVI), *P = 0.0174 (LM20), **P = 0.0076 and ***P = 0.0002, two-sided unpaired Student's t test.

(H) Compound II dose-response curves for BRAF wild-type predicted TBK1i-sensitive (red) and -resistant (black) melanoma cell lines.

(I) Comparison of area under the curve values for dose response curves from predicted TBK1i resistant (subtype 1) and sensitive (subtype 2) melanoma cell lines exposed to BX795

(two-sided unpaired Mann-Whitney test ***P = 0.0001) and compound II (two-sided unpaired Mann-Whitney test ***P = 0.0002).

(J) Cumulative distribution function (CDF) plot of mRNA expression of pigment genes (MITF, DCT, TYR, MLANA, TYRP1, PMEL and PPARGC1) comparing TBK1 inhibitor sensitive CHL1 and resistant cell lines COLO792 and MEWO. P = 1.7E-05, one-sided two-sample K-S test.

(K) Compound II dose-response curves for A375 parental cells and A375 MEKi resistant clones. Dots indicate mean ± s.d. (n = 3).

(L) ROC curve analysis for compound II response.

(M) Kaplan-Meier plot of the overall survival of predicted TBK1i sensitive and resistant TCGA uveal melanoma patients. Statistical significance was assessed using the Log-rank (Mantel-Cox) test.

(N) Distribution of uveal melanoma cell lines based on the linear weighted sums of the individual gene expression values for each predictive feature measured by qPCR.

(O) Compound II dose-response curves for predicted TBK1i sensitive (red) and resistant (black) uveal melanoma cell lines from the tails of the distribution. Dots indicate mean ± s.d. (n = 3).

(P) Dot plot showing the compound II LD50 values of uveal melanoma cell lines (y-axis) and the corresponding linear weighted sums of the individual gene expression values for each predictive feature (x-axis). Predicted TBK1i sensitive cell lines are labeled red.

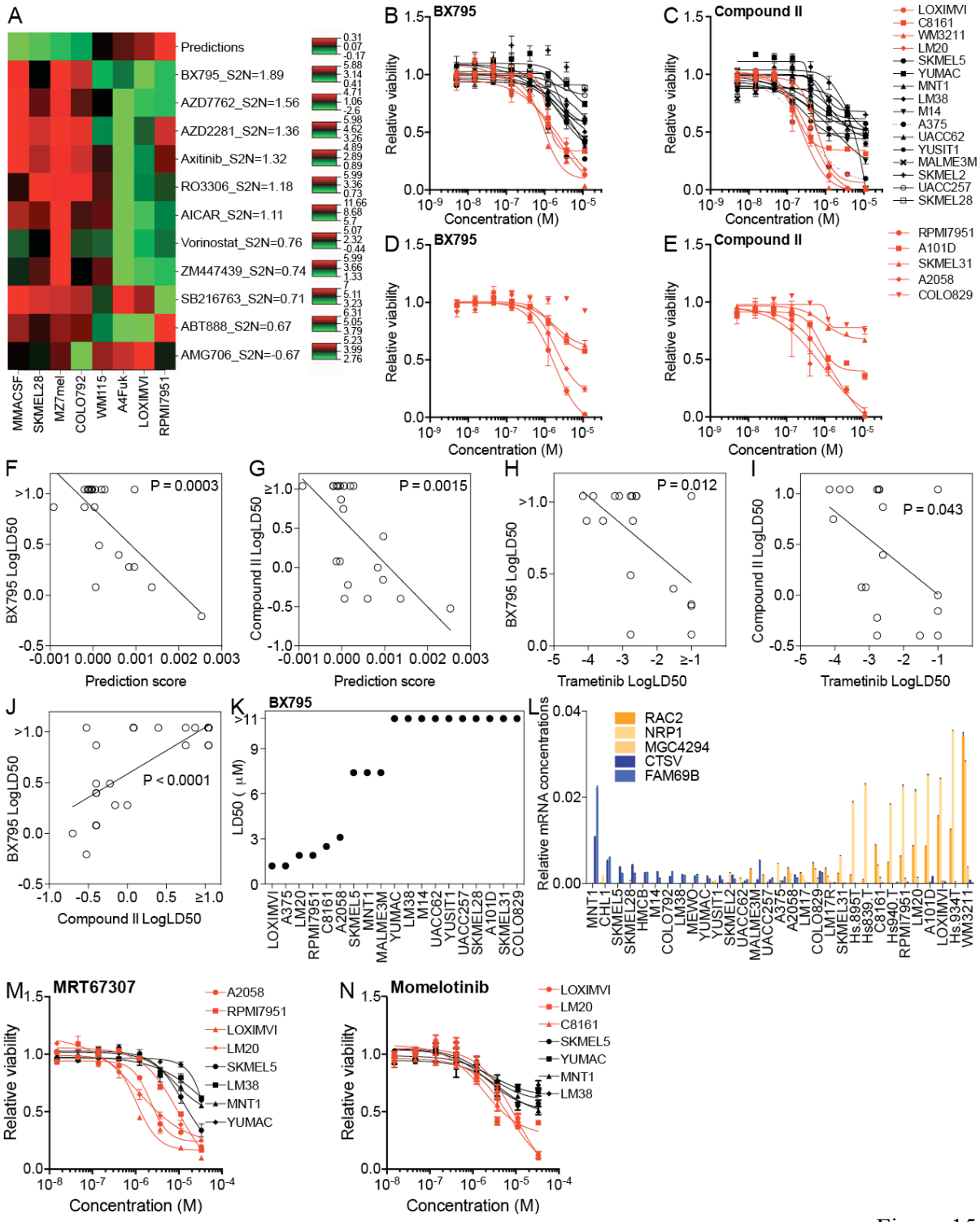
A
Predictions
BX795_S2N=1.89
AZD7762_S2N=1.56
AZD2281_S2N=1.36
Axitinib_S2N=1.32
RO3306_S2N=1.18
AICAR_S2N=1.11
Vorinostat_S2N=0.76
ZM447439_S2N=0.74
SB216763_S2N=0.71
ABT888_S2N=0.67
AMG706_S2N=-0.67
MMACSF
SKMEL28
MZ7mel
COLO792
WM115
A4Fuk
LOXIMVI
RPMI7951
B BX795
C Compound II
D BX795
E Compound II
Relative viability
Concentration (M)
LOXIMVI
C8161
WM3211
LM20
SKMEL5
YUMAC
MNT1
LM38
M14
A375
UACC62
YUSIT1
MALME3M
SKMEL2
UACC257
SKMEL28
RPMI7951
A101D
SKMEL31
A2058
COLO829
F P = 0.0003
G P = 0.0015
H P = 0.012
I P = 0.043
BX795 LogLD50
Compound II LogLD50
Prediction score
Trametinib LogLD50
J P < 0.0001
Compound II LogLD50
K BX795
LD50 (μM)
L
Relative mRNA concentrations
RAC2
NRP1
MGC4294
CTSV
FAM69B
M MRT67307
N Momelotinib

Figure 15

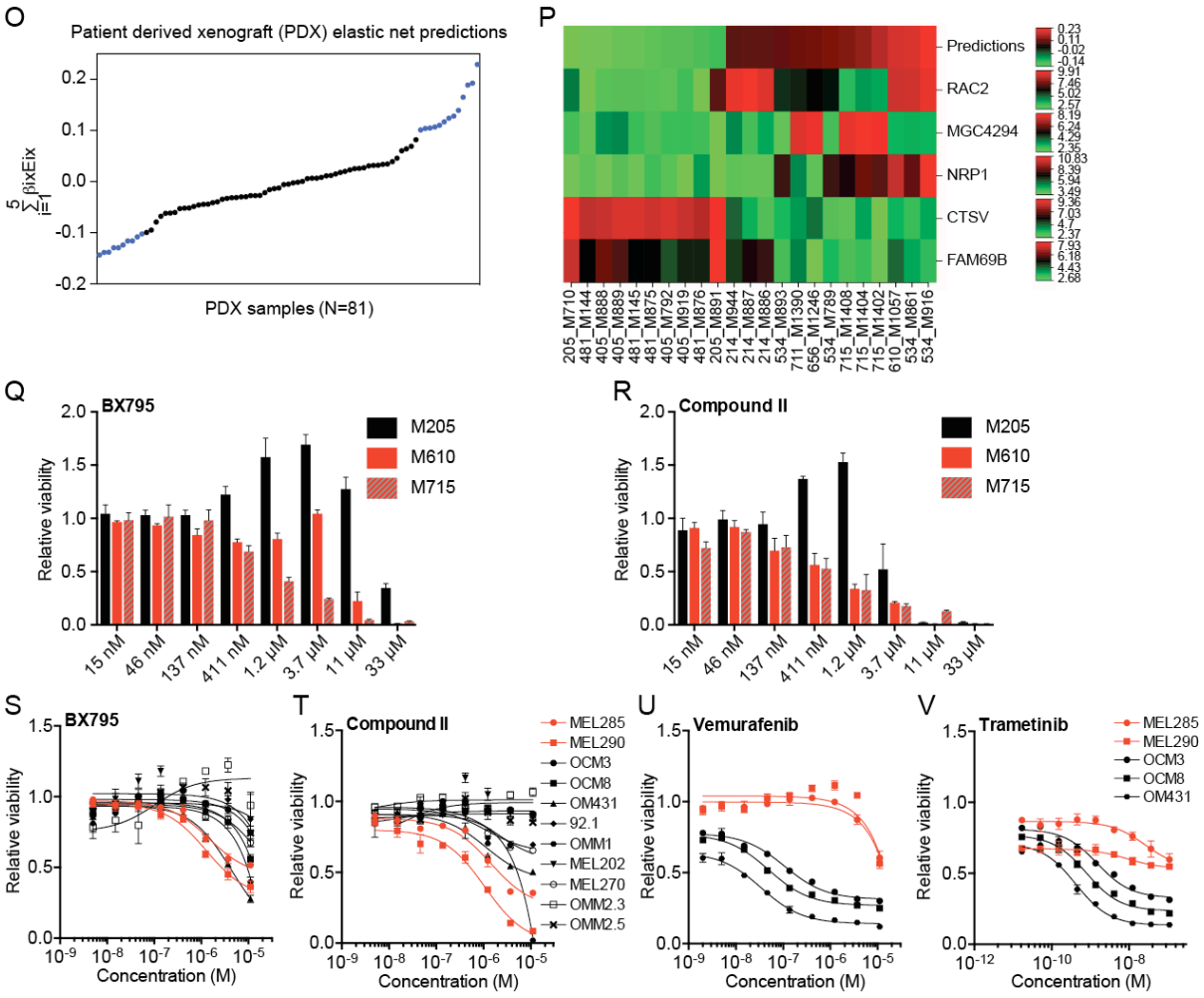

Figure 15 continued

Figure 15. Nomination of TBK1 as a Therapeutic Target for Drug-Resistant Melanoma, Related to Figure 14

(A) S2N ratios for the top 10 compounds that were selectively toxic to predicted drug-resistant melanoma (related to Figure 14B).

(B-C) BX795 (B) and compound II (C) dose-response curves for MAPK pathway inhibitor-sensitive (black) and resistant (red) melanoma cell lines.

(D-E) BX795 (D) and compound II (E) dose-response curves for predicted MAPK pathway inhibitor-resistant (red) CCLE melanoma cell lines.

(F-G) Linear regression analysis of BX795 (F) and compound II (G) LD50 values for each cell line and the corresponding prediction scores determined using the summed weight metric based on the elastic net derived expression features.

(H-I) Linear regression analysis of BX795 (F) and compound II (G) LD50 values for each cell line and their corresponding trametinib LD50 values.

(J) Linear regression analysis of BX795 and compound II LD50 values.

(K) BX795 LD50 values in the melanoma panel.

(L) qPCR analysis of RAC2, NRP1, MGC4294, CTSV and FAM69B mRNA concentrations in BRAF(V600) and BRAF wild-type melanoma cells. Bars indicate mean ± s.d. (n = 3).

(M-N) MRT67307 (M) and momelotinib (N) dose-response curves for predicted TBK1 inhibitor-sensitive (red) and resistant (black) melanoma cell lines.

(O) Distribution of patient derived xenografts (PDXs) based on the linear weighted sums of the individual gene expression values for each predictive feature.

(P) Biomarker behavior in the predicted TBK1 inhibitor-sensitive and resistant samples.

(Q-R) Consequence of BX795 (Q) and compound II (R) exposure on the viability of predicted TBK1 inhibitor-sensitive (red) and resistant (black) primary melanoma cells in culture.

(S-T) BX795 (S) and compound II (T) dose-response curves for predicted TBK1 inhibitor-resistant (black) and -sensitive (red) uveal melanoma cell lines.

(U-V) Vemurafenib (U) and trametinib (V) dose-response curves for predicted TBK1 inhibitor-sensitive (red) and -resistant (black-BRAF(V600)) uveal melanoma cell lines.

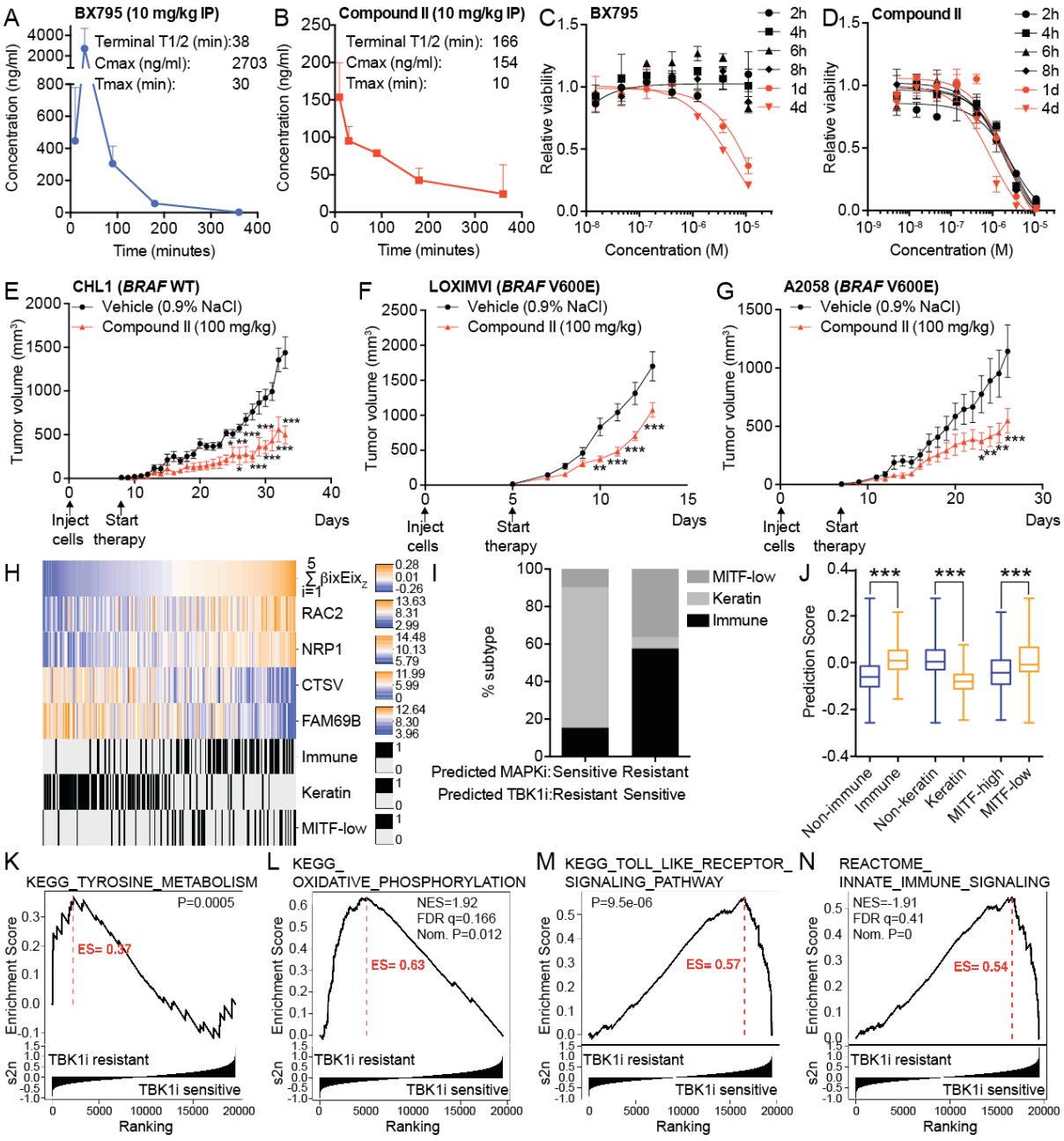
A
BX795 (10 mg/kg IP)
Terminal T1/2 (min): 38
Cmax (ng/ml): 2703
Tmax (min): 30
Concentration (ng/ml)
Time (minutes)
B
Compound II (10 mg/kg IP)
Terminal T1/2 (min): 166
Cmax (ng/ml): 154
Tmax (min): 10
Concentration (ng/ml)
Time (minutes)
C
BX795
2h
4h
6h
8h
1d
4d
Relative viability
Concentration (M)
D
Compound II
2h
4h
6h
8h
1d
4d
Relative viability
Concentration (M)
E
CHL1 (BRAF WT)
Vehicle (0.9% NaCl)
Compound II (100 mg/kg)
Tumor volume (mm3)
Inject cells
Start therapy
Days
F
LOXIMVI (BRAF V600E)
Vehicle (0.9% NaCl)
Compound II (100 mg/kg)
Tumor volume (mm3)
Inject cells
Start therapy
Days
G
A2058 (BRAF V600E)
Vehicle (0.9% NaCl)
Compound II (100 mg/kg)
Tumor volume (mm3)
Inject cells
Start therapy
Days
H
RAC2
NRP1
CTSV
FAM69B
Immune
Keratin
MITF-low
I
% subtype
MITF-low
Keratin
Immune
Predicted MAPKi: Sensitive Resistant
Predicted TBK1i: Resistant Sensitive
J
Prediction Score
Non-immune
Immune
Non-keratin
Keratin
MITF-high
MITF-low
K
KEGG_TYROSINE_METABOLISM
P=0.0005
ES= 0.37
Enrichment Score
TBK1i resistant
TBK1i sensitive
s2n
Ranking
L
KEGG_OXIDATIVE_PHOSPHORYLATION
NES=1.92
FDR q=0.166
Nom. P=0.012
ES= 0.63
Enrichment Score
TBK1i resistant
TBK1i sensitive
s2n
Ranking
M
KEGG_TOLL_LIKE_RECEPTOR_SIGNALING_PATHWAY
P=9.5e-06
ES= 0.57
Enrichment Score
TBK1i resistant
TBK1i sensitive
s2n
Ranking
N
REACTOME_INNATE_IMMUNE_SIGNALING
NES=-1.91
FDR q=0.41
Nom. P=0
ES= 0.54
Enrichment Score
TBK1i resistant
TBK1i sensitive
s2n
Ranking

Figure 16

Figure 16. TBK1/IKKε-Addiction is Conserved In Vivo and Corresponds to a Cell Autonomous Innate Immune Melanoma Subtype

(A-B) Pharmacokinetic assays for BX795 (A) and compound II (B) indicate the maximum concentrations of the compounds in plasma, time to reach the maximum concentrations and half-life of the compounds following IP injection at 10mg/kg.

(C-D) LOXIMVI cells were exposed to BX795 (C) or compound II (D) at the indicated concentrations for the indicated times. Cell viability was measured after 96 hours for all conditions. Bars indicate mean ± s.d. (n = 3).

(E-G) 1 x 10^6 CHL1 cells (E) 5 x 10^5 LOXIMVI cells (F) or 7.5 x 10^5 A2058 cells/flank (G) were injected subcutaneously into one flank (CHL1) or both flanks (LOXIMVI and A2058) of NOD/SCID IL2Rg^{null} (NSG) mice. (N = 8 mice per group). Compound II (100 mg/kg) or saline were delivered IP daily after detection of palpable tumors (5 days post inoculation for LOXIMVI and 7 days post inoculation for A2058 and CHL1). Tumor volume versus treatment time is indicated. Dots indicate mean ± standard error of mean (N = 16 for LOXIMVI and A2058, N = 8 for CHL1), *P = 0.0428 (CHL1, day 24), *P = 0.0314 (CHL1, day 26), **P = 0.0013 (CHL1, day 27), **P = 0.0018 (LOXIMVI), *P = 0.0324, **P = 0.0042 (A2058, day 24), **P = 0.0017 (A2058, day 25) and ***P < 0.0001, two-way ANOVA followed by Bonferroni's multiple comparisons test).

(H) Biomarker behavior in the TCGA SKCM tumors with low lymphocyte infiltration. Top row indicates prediction score. Subsequent rows indicate $\log_2$ normalized expression of the indicated genes. Immune (black), keratin (black) and MITF-low (black) tumors are indicated as determined in The Cancer Genome Atlas Network, Cell.

(I) Bars indicate the percentage of different subtypes in predicted MAPKi sensitive/TBK1i resistant (prediction score cut-off is < -0.05) and predicted MAPKi resistant/TBK1i sensitive (prediction score cut-off is 0.05 <) subtypes.

(J) Comparison of prediction scores between the indicated subtypes; two-sided unpaired Mann-Whitney test, ***P < 0.0001 for immune versus non-immune and keratin versus non-keratin, ***P = 0.0009 for MITF-low versus MITF-high.

(K-L) GSEA analysis shows a positive enrichment of tyrosine metabolism (K) and oxidative phosphorylation (L) in the predicted MAPKi sensitive/TBK1i resistant (prediction score cut-off is < -0.05) cohort.

(M-N) GSEA analysis shows a positive enrichment of toll-like receptor signaling (M) and innate immune signaling (N) in predicted MAPKi resistant/TBK1i sensitive (prediction score cut-off is 0.05 <) cohort.

Tumor ID#	Tumor weight (mg)	DI H2O added (µL)	Compound II concentration (ng/ml detected)	Dilution rate
Combined Vehicle	1173.6	3520.8	0	4
1538R	261.8	785.4	948	4
1538L	186.4	559.2	780	4
1532R	260.4	781.2	1760	4
1532L	17.8	NA	NA	NA
1544R	292.8	878.4	1030	4
1544L	379.8	1139.4	1620	4
1542R	111.2	333.6	579	4
1542L	227	681	510	4
1537R	161.6	484.8	787	4
1537L	183.4	550.2	1630	4
1525R	238.3	714.9	896	4
1525L	181.9	545.7	709	4
1536R	275.4	826.2	910	4
1536L	260.1	780.3	3270	4
1533R	352.2	1056.6	1220	4
1533L	216.9	650.7	3610	4

Table 2. Compound II concentrations in xenografted tumors.

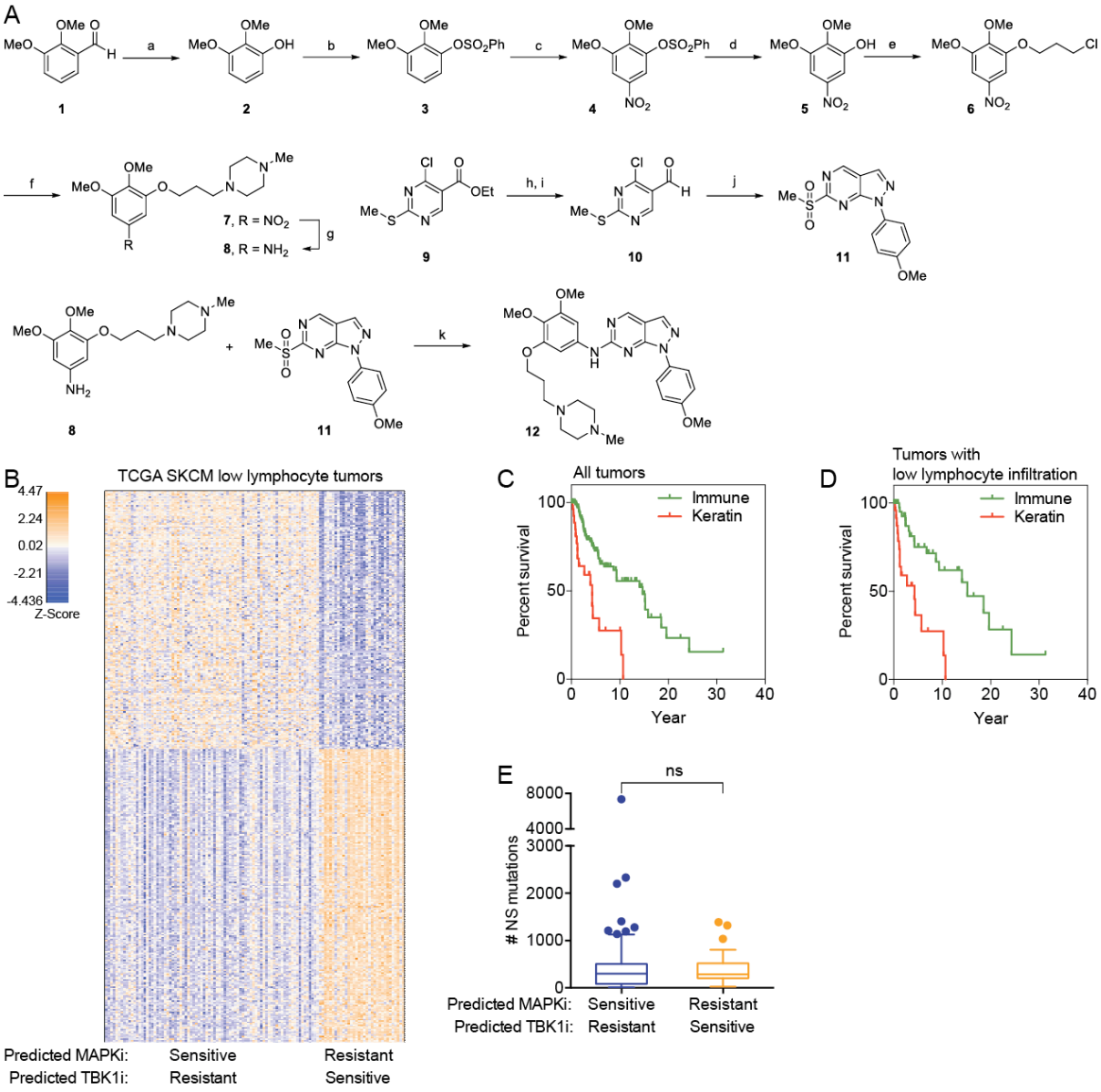
A
1
2
3
4
5
6
7, R = NO2
8, R = NH2
9
10
11
12
B
TCGA SKCM low lymphocyte tumors
4.47
2.24
0.02
-2.21
-4.436
Z-Score
Predicted MAPKi: Sensitive Resistant
Predicted TBK1i: Resistant Sensitive
C
All tumors
Immune
Keratin
Percent survival
Year
D
Tumors with
low lymphocyte infiltration
Immune
Keratin
Percent survival
Year
E
ns
NS mutations
Predicted MAPKi: Sensitive Resistant
Predicted TBK1i: Resistant Sensitive

Figure 17

Figure 17. TBK1/IKKε-Addiction is Conserved In Vivo and Corresponds to a Cell Autonomous Innate Immune Melanoma Subtype, Related to Figure 16

(A) Reagents and conditions. a) boric acid (5.0 equiv), 30% H_2O_2 (2.2 equiv), H_2SO_4, THF, 23 ºC, 24 h; b) benzenesulfonyl chloride (1.1 equiv), Et_3N (1.2 equiv), CH_2Cl_2, 23 ºC, 14 h, 54% (two steps); c) AcOH (14.0 equiv), HNO_3, 23 ºC, 10 h, 60%; d) 20% KOH, MeOH, 50 ºC, 4 h, 88%; e) 1-bromo-3-chloropropane (3.0 equiv), K_2CO_3 (2.0 equiv), DMF, 23 ºC, 10 h, 84%; f) 1-methylpiperazine (5.0 equiv), NaI (0.1 equiv), DMF, 23 ºC, 5 h, 85%; g) Fe (5.0 equiv), satd. aqueous NH_4Cl, EtOH, 100 ºC, 3 h, 95%; h) DIBAL-H (3.0 equiv), THF, -78 to 23 ºC, 12 h, 52%; i) MnO_2 (5.0 equiv), $CHCl_3$, 23 ºC, 48 h, 70%; j) 1. Et_3N (2.1 equiv), (4-methoxyphenyl)hydrazine hydrochloride (2.0 equiv), THF, MW, 1 h, 150 ºC, 73%; 2. 3-chloroperoxybenzoic acid (3.0 equiv), CH_2Cl_2, 23 ºC, 2 h, 73%; k) **8** (1.0 equiv), **11** (1.1 equiv), Et_3N (1.1 equiv), 1-methyl-3-pentanol, MW, 150 ºC, 4 h, 37%.

(B) S2N analysis shows the most differentially expressed genes in predicted MAPKi sensitive/TBK1i resistant (prediction score cut-off is < -0.05) and predicted MAPKi resistant/TBK1i sensitive (prediction score cut-off is 0.05 <) cohorts in TCGA SKCM with low lymphocyte infiltration.

(C-D) Kaplan-Meier plot of the overall survival of all immune versus keratin subtype (C) and of low lymphocyte infiltrated immune versus keratin subtype (D) melanoma patients.

(E) Comparison of number of mutations between the indicated subtypes; two-sided unpaired Mann-Whitney test, P = 0.3791.

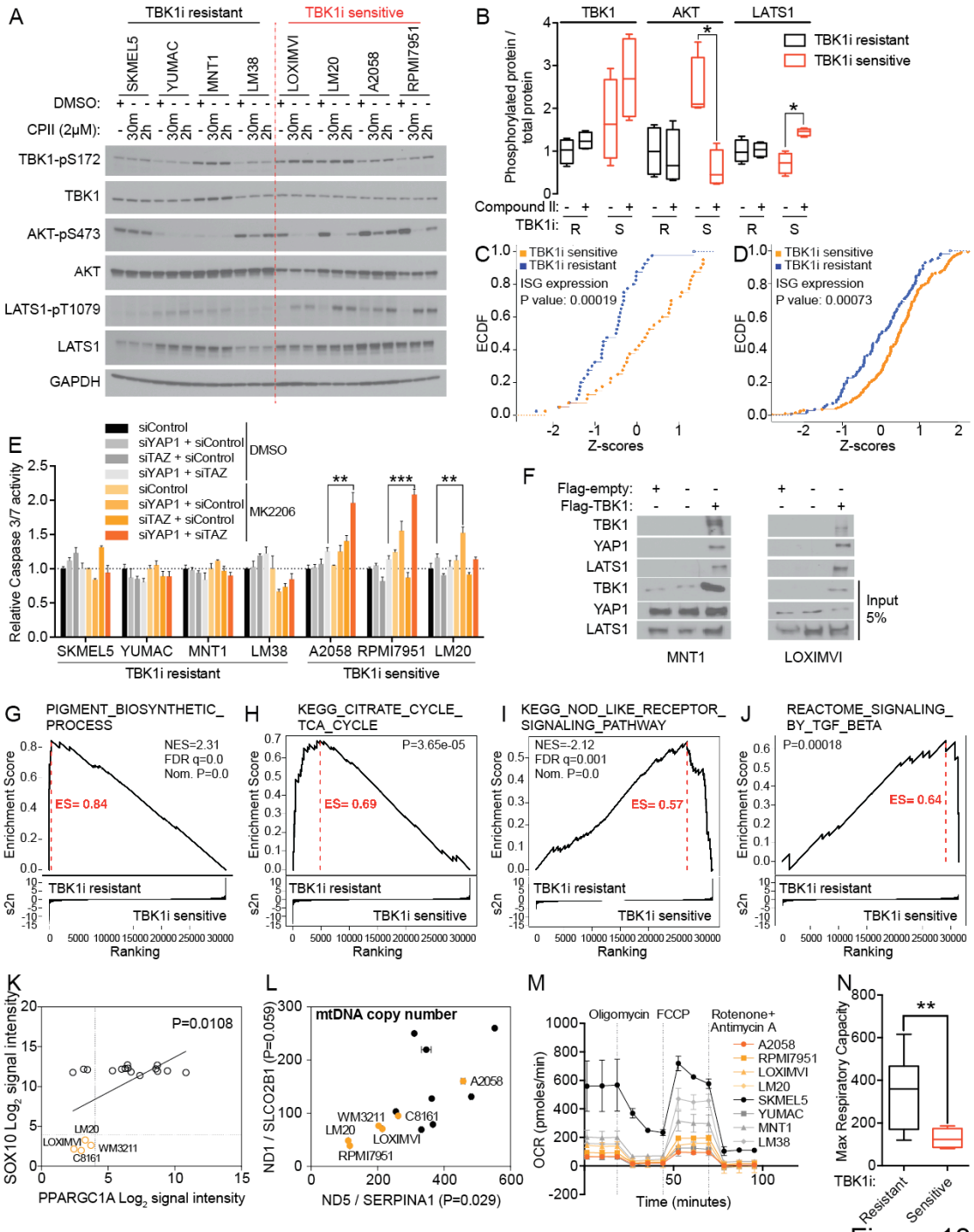
A
TBK1i resistant
TBK1i sensitive
SKMEL5
YUMAC
MNT1
LM38
LOXIMVI
LM20
A2058
RPMI7951
DMSO:
CPII (2μM):
30m
2h
TBK1-pS172
TBK1
AKT-pS473
AKT
LATS1-pT1079
LATS1
GAPDH
B
TBK1
AKT
LATS1
TBK1i resistant
TBK1i sensitive
Phosphorylated protein / total protein
Compound II:
TBK1i:
R
S
C
TBK1i sensitive
TBK1i resistant
ISG expression
P value: 0.00019
ECDF
Z-scores
D
TBK1i sensitive
TBK1i resistant
ISG expression
P value: 0.00073
ECDF
Z-scores
E
siControl
siYAP1 + siControl
siTAZ + siControl
siYAP1 + siTAZ
DMSO
MK2206
Relative Caspase 3/7 activity
SKMEL5
YUMAC
MNT1
LM38
A2058
RPMI7951
LM20
TBK1i resistant
TBK1i sensitive
F
Flag-empty:
Flag-TBK1:
TBK1
YAP1
LATS1
Input 5%
MNT1
LOXIMVI
G
PIGMENT_BIOSYNTHETIC_PROCESS
NES=2.31
FDR q=0.0
Nom. P=0.0
ES= 0.84
Enrichment Score
s2n
TBK1i resistant
TBK1i sensitive
Ranking
H
KEGG_CITRATE_CYCLE_TCA_CYCLE
P=3.65e-05
ES= 0.69
I
KEGG_NOD_LIKE_RECEPTOR_SIGNALING_PATHWAY
NES=-2.12
FDR q=0.001
Nom. P=0.0
ES= 0.57
J
REACTOME_SIGNALING_BY_TGF_BETA
P=0.00018
ES= 0.64
K
P=0.0108
SOX10 Log2 signal intensity
PPARGC1A Log2 signal intensity
LM20
LOXIMVI
SK
C8161
WM3211
L
mtDNA copy number
ND1 / SLCO2B1 (P=0.059)
ND5 / SERPINA1 (P=0.029)
A2058
WM3211
C8161
LM20
LOXIMVI
RPMI7951
M
Oligomycin
FCCP
Rotenone+ Antimycin A
OCR (pmoles/min)
Time (minutes)
A2058
RPMI7951
LOXIMVI
LM20
SKMEL5
YUMAC
MNT1
LM38
N
Max Respiratory Capacity
TBK1i:
Resistant
Sensitive

Figure 18

Figure 18. TBK1/IKKε Activate AKT and YAP to Support Survival of the Cell-autonomous Immune Melanoma Subtype

(A) Whole cell lysates, exposed to compound II for the indicated times, were assessed for the accumulation of the indicated phosphorylated proteins by immunoblot.

(B) Phosphorylated TBK1, AKT and LATS1 protein concentrations relative to total TBK1, AKT and LATS1 protein concentrations were measured from Figure 18A using Image J (background corrected).

(C-D) Cumulative distribution function (CDF) plot of mRNA expression of interferon-stimulated gene (ISG) expression comparing TBK1 inhibitor sensitive and resistant cell lines (C) and predicted TBK1 inhibitor sensitive and resistant TCGA SKCM tumors with low lymphocyte infiltration (D) one-sided two-sample K-S test.

(E) Caspase-3 and -7 activity was measured after exposure of MK2206 (1mM) for 24 hours following the siRNA-mediated knockdown of indicated genes in TBK1 inhibitor sensitive and resistant cell lines. Bars indicate mean ± s.d. (n = 3). **P = 0.0016 (A2058), ***P < 0.0001 (RPMI7951), and **P = 0.0032 (LM20), two-sided unpaired Student's t test.

(F) TBK1 was overexpressed in MNT1 and LOXIMVI, then immunoprecipitated with an antibody directed to the flag tag. Immunoprecipitates were analyzed for coprecipitation with YAP1 and LATS1.

(G-H) GSEA analysis shows a positive enrichment of pigment biosynthetic process (G) and TCA cycle (H) in TBK1i resistant cell lines.

(I-J) GSEA analysis shows a positive enrichment of nod-like receptor signaling (I) and TGFβ signaling (J) in TBK1i sensitive cell lines.

(K) Linear regression analysis of SOX10 (y-axis) and PPARCG1A (x-axis) $\log_2$ signal intensity values from microarray in the melanoma discovery set.

(L) Dot-plot shows the mitochondrial DNA copy number as measured by primer sets that designed for specific detection of two mitochondrial DNA targets (ND1 and ND5) and two nuclear DNA targets (SLCO2B1 and SERPINA1).

(M) Oxygen consumption rates of TBK1 inhibitor resistant (gray tones) and sensitive (orange tones) cell lines.

(N) Maximum respiratory capacity in TBK1 inhibitor sensitive and resistant cell lines; two-sided unpaired Mann-Whitney test, **P = 0.0011.

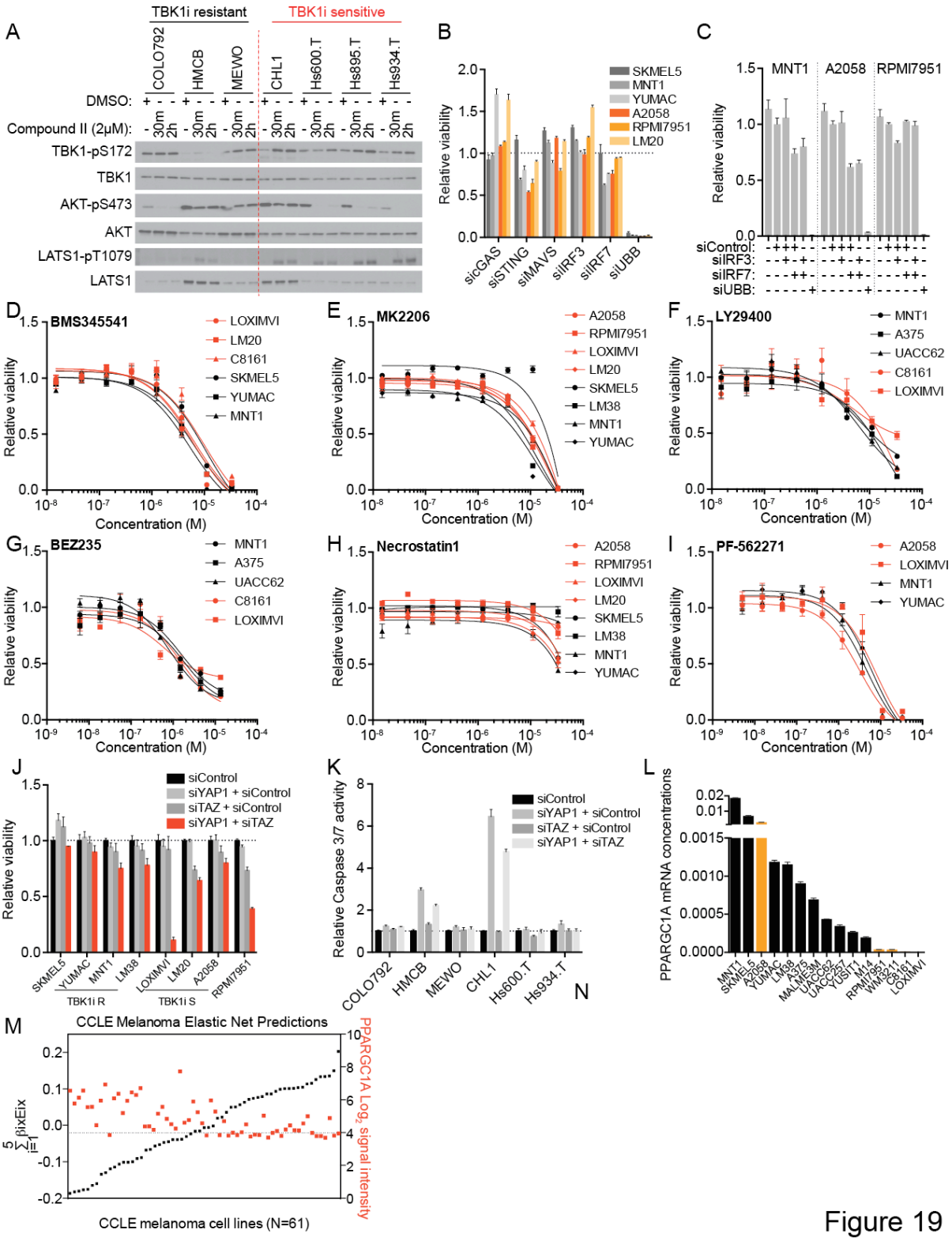
A
TBK1i resistant
TBK1i sensitive
COLO792
HMCB
MEWO
CHL1
Hs600.T
Hs895.T
Hs934.T
DMSO:
Compound II (2μM):
30m
2h
TBK1-pS172
TBK1
AKT-pS473
AKT
LATS1-pT1079
LATS1
B
Relative viability
SKMEL5
MNT1
YUMAC
A2058
RPMI7951
LM20
siGAS
siSTING
siMAVS
siIRF3
siIRF7
siUBB
C
MNT1
A2058
RPMI7951
siControl:
siIRF3:
siIRF7:
siUBB:
D
BMS345541
LOXIMVI
LM20
C8161
SKMEL5
YUMAC
MNT1
Concentration (M)
E
MK2206
A2058
RPMI7951
LOXIMVI
LM20
SKMEL5
LM38
MNT1
YUMAC
F
LY29400
MNT1
A375
UACC62
C8161
LOXIMVI
G
BEZ235
H
Necrostatin1
I
PF-562271
J
siControl
siYAP1 + siControl
siTAZ + siControl
siYAP1 + siTAZ
TBK1i R
TBK1i S
K
Relative Caspase 3/7 activity
L
PPARGC1A mRNA concentrations
M
CCLE Melanoma Elastic Net Predictions
PPARGC1A Log2 signal intensity
CCLE melanoma cell lines (N=61)
N

Figure 19

Figure 19. TBK1/IKKε Activate AKT and YAP to Support Survival of the Cell-autonomous Immune Melanoma Subtype, Related to Figure 18

(A) Whole cell lysates, exposed to compound II for the indicated times, were assessed for the accumulation of the indicated phosphorylated and total proteins by immunoblot.

(B) Consequences of depletion of indicated genes in TBK1 inhibitor sensitive and resistant melanoma cell lines. Bars indicate mean ± s.d. (n = 3).

(C) Consequences of IRF3 and IRF7 co-depletion in TBK1 inhibitor sensitive and resistant melanoma cell lines. Bars indicate mean ± s.d. (n = 3).

(D-I) BMS345541 (IKKβ inhibitor) (D), MK2206 (allosteric AKT inhibitor) (E), LY29400 (PI3K inhibitor) (F), BEZ235 (dual PI3K, mTOR inhibitor) (G), Necrostatin1 (RIP1 inhibitor) (H) and PF-562271 (FAK inhibitor) (I) dose-response curves for TBK1 inhibitor sensitive (red) and resistant (black) melanoma cell lines. Dots indicate mean ± s.d. (n = 3).

(J) Consequences of depletion of indicated genes in TBK1 inhibitor sensitive and resistant melanoma cell lines. Bars indicate mean ± s.d. (n = 3).

(K) Caspase-3 and -7 activity was measured following the depletion of indicated genes for 48 hr in TBK1 inhibitor sensitive and resistant BRAF wild-type cell lines. Bars indicate mean ± s.d. (n = 3).

(L) qPCR analysis of PPARGC1A mRNA concentrations in melanoma cells. Bars indicate mean ± s.d. (n = 3).

(M) Distribution of Cancer Cell Line Encyclopedia (CCLE) melanoma cell lines based on the linear weighted sums of the individual gene expression values for each predictive feature

(left y-axis) and the corresponding PPARCG1A $\log_2$ signal intensity values from microarray (right y-axis).

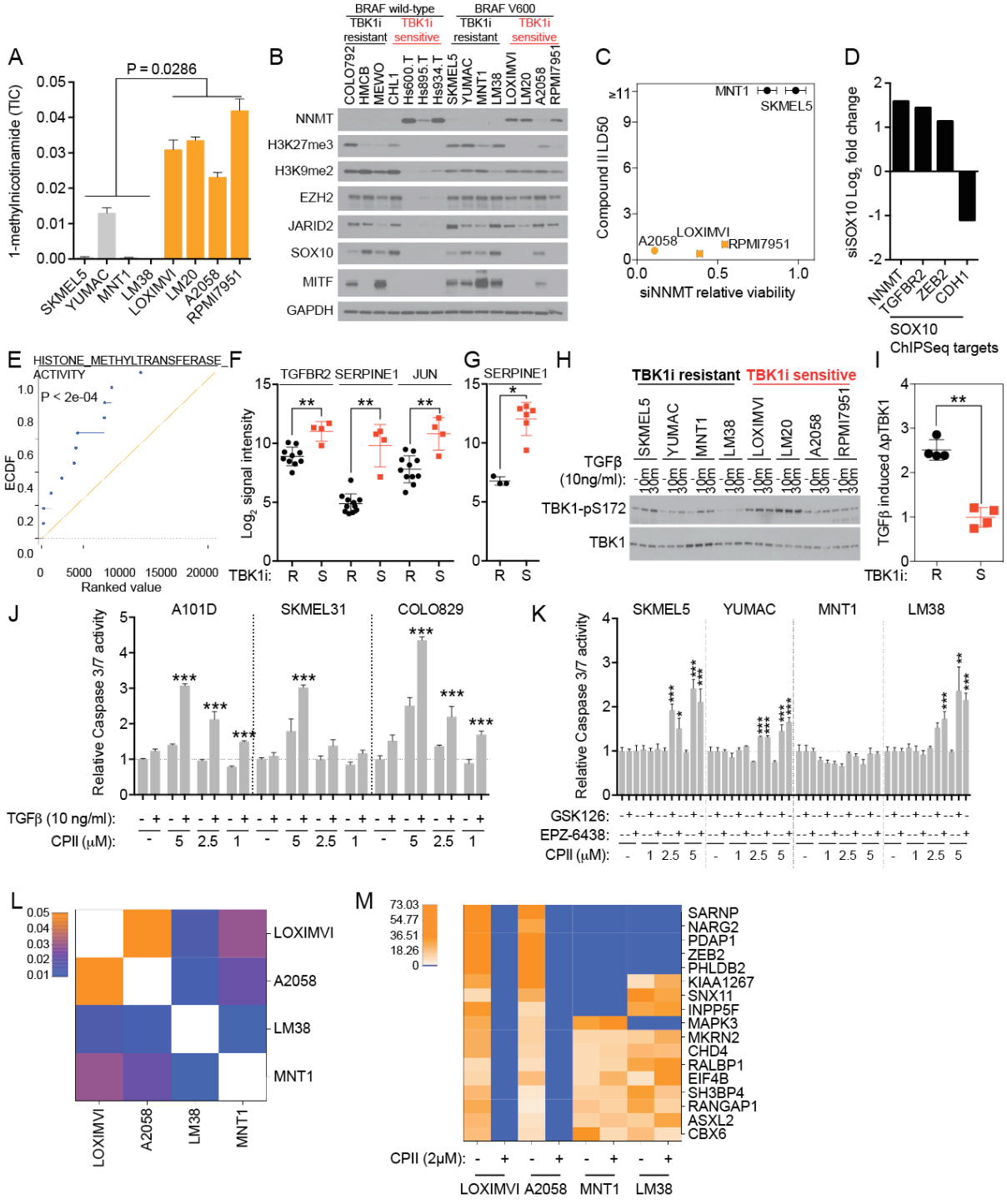
A
P = 0.0286
1-methylnicotinamide (TIC)
SKMEL5
YUMAC
MNT1
LM38
LOXIMVI
LM20
A2058
RPMI7951
B
BRAF wild-type
BRAF V600
TBK1i resistant
TBK1i sensitive
NNMT
H3K27me3
H3K9me2
EZH2
JARID2
SOX10
MITF
GAPDH
C
Compound II LD50
siNNMT relative viability
MNT1
SKMEL5
LOXIMVI
A2058
RPMI7951
D
siSOX10 Log2 fold change
NNMT
TGFBR2
ZEB2
CDH1
SOX10 ChIPSeq targets
E
HISTONE_METHYLTRANSFERASE_ACTIVITY
P < 2e-04
ECDF
Ranked value
F
TGFBR2
SERPINE1
JUN
Log2 signal intensity
TBK1i:
G
SERPINE1
H
TBK1i resistant
TBK1i sensitive
TGFβ (10ng/ml):
TBK1-pS172
TBK1
I
TGFβ induced ΔpTBK1
J
A101D
SKMEL31
COLO829
Relative Caspase 3/7 activity
TGFβ (10 ng/ml):
CPII (μM):
K
SKMEL5
YUMAC
MNT1
LM38
Relative Caspase 3/7 activity
GSK126:
EPZ-6438:
CPII (μM):
L
LOXIMVI
A2058
LM38
MNT1
M
SARNP
NARG2
PDAP1
ZEB2
PHLDB2
KIAA1267
SNX11
INPP5F
MAPK3
MKRN2
CHD4
RALBP1
EIF4B
SH3BP4
RANGAP1
ASXL2
CBX6
CPII (2μM):
LOXIMVI
A2058
MNT1
LM38

Figure 20

Figure 20. Distinct Epigenetic Cell Fate Programs Specify TBK1/IKKε Addiction

(A) Comparison of 1-MNA abundance in TBK1 inhibitor resistant (gray) and sensitive cell lines (orange); two-sided unpaired Mann-Whitney test.

(B) Whole cell lysates were assessed for the accumulation of the indicated proteins by immunoblot.

(C) Dot-plot shows compound II LD50 values (y-axis) and the consequence of NNMT depletion (x-axis) in the corresponding cell lines.

(D) Bars indicate the $\log_2$ fold change of the indicated genes in response to SOX10 depletion.

(E) Empirical cumulative distribution function (ECDF) plot of mRNA expression of histone methyltransferase activity related genes in siSOX10 (blue) versus the siControl treated MNT1 cells (background).

(F) Illumina-derived $\log_2$ signal intensity values of indicated genes in TBK1 inhibitor resistant (SKMEL5, YUMAC, MNT1 and LM38) and sensitive (LOXIMVI, LM20, C8161 and WM3211) cell lines; two-sided unpaired Mann-Whitney test, **P = 0.008 (TGFBR2), **P = 0.0015 (SERPINE1) and **P = 0.0051 (JUN).

(G) Affymetrix-derived $\log_2$ signal intensity values of SERPINE1 in TBK1 inhibitor resistant (A101D, COLO829 and SKMEL31) and sensitive (RPMI7951, LOXIMVI, Hs895.T, Hs839.T, Hs934.T, Hs940.T) cell lines; two-sided unpaired Mann-Whitney test, *P = 0.0238.

(H) Whole cell lysates, stimulated with TGFβ for the indicated times, were assessed for the accumulation of the phosphorylated TBK1 by immunoblot.

(I) Fold difference of phosphorylated TBK1 protein concentrations at 30 m timepoint relative to the 0 m timepoint was measured from Figure 20H using Image J (background corrected).

(J) Caspase-3 and -7 activity was measured after TGFβ stimulated (24 hours) TBK1 inhibitor resistant cell lines followed by the exposure to DMSO or compound II for an additional 24 hours. Bars indicate mean ± s.d. (n = 3). One-way ANOVA followed by Tukey's multiple comparisons test, ***P < 0.0001.

(K) Caspase-3 and -7 activity was measured after EZH2 inhibitor exposed (24 hours) TBK1 inhibitor resistant cell lines followed by the exposure to DMSO or compound II for an additional 24 hours. Bars indicate mean ± s.d. (n = 3). One-way ANOVA followed by Tukey's multiple comparisons test, *P = 0.0106 (SKMEL5), ***P = 0.0004 (YUMAC, GSK126 and compound II (2.5 mM), ***P = 0.006 (YUMAC, EPZ-6438 and compound II (2.5 mM), **P = 0.0025 (LM38) and ***P < 0.0001.

(L) Pearson correlation of phosphospeptide adjusted ion intensities in TBK1 inhibitor resistant (MNT1 and LM38) and sensitive (LOXIMVI and A2058) cell lines.

(L) S2N analysis shows the most differentially reduced phosphopeptide levels in TBK1 inhibitor sensitive cell lines compared to resistant cell lines.

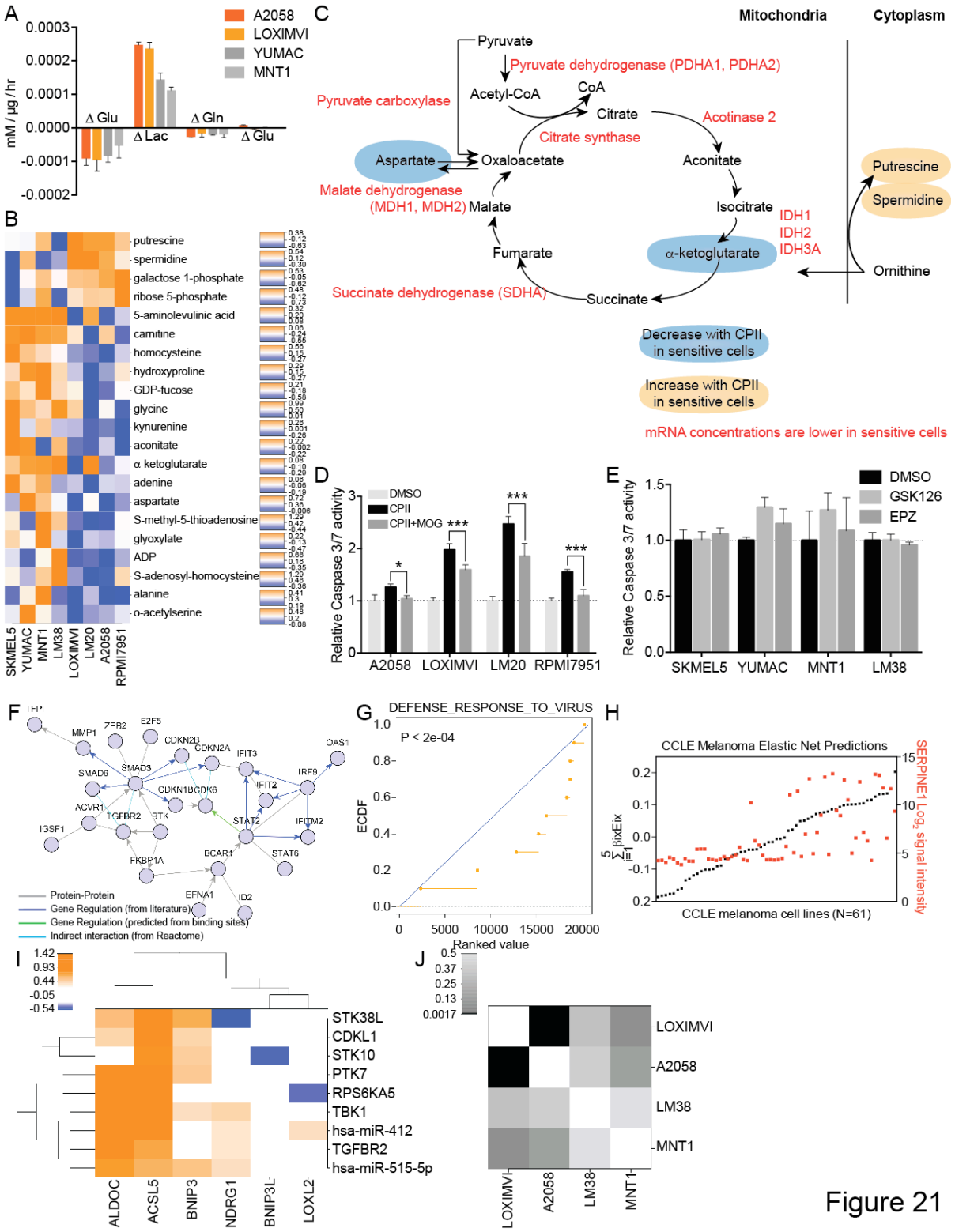
A
A2058
LOXIMVI
YUMAC
MNT1
mM / µg / hr
Δ Glu
Δ Lac
Δ Gln
Δ Glu
B
putrescine
spermidine
galactose 1-phosphate
ribose 5-phosphate
5-aminolevulinic acid
carnitine
homocysteine
hydroxyproline
GDP-fucose
glycine
kynurenine
aconitate
α-ketoglutarate
adenine
aspartate
S-methyl-5-thioadenosine
glyoxylate
ADP
S-adenosyl-homocysteine
alanine
o-acetylserine
SKMEL5
YUMAC
MNT1
LM38
LOXIMVI
LM20
A2058
RPMI7951
C
Mitochondria
Cytoplasm
Pyruvate
Pyruvate dehydrogenase (PDHA1, PDHA2)
Pyruvate carboxylase
Acetyl-CoA
CoA
Citrate
Acotinase 2
Citrate synthase
Aspartate
Oxaloacetate
Aconitate
Malate dehydrogenase
(MDH1, MDH2)
Malate
Isocitrate
IDH1
IDH2
IDH3A
Fumarate
α-ketoglutarate
Succinate dehydrogenase (SDHA)
Succinate
Putrescine
Spermidine
Ornithine
Decrease with CPII in sensitive cells
Increase with CPII in sensitive cells
mRNA concentrations are lower in sensitive cells
D
DMSO
CPII
CPII+MOG
Relative Caspase 3/7 activity
A2058
LOXIMVI
LM20
RPMI7951
E
DMSO
GSK126
EPZ
Relative Caspase 3/7 activity
SKMEL5
YUMAC
MNT1
LM38
F
MMP1
ZFR2
E2F5
CDKN2B
CDKN2A
IFIT3
OAS1
SMAD6
SMAD3
IRF9
IFIT2
CDKN1B
CDK6
ACVR1
TGFBR2
RTK
IGSF1
STAT2
IFITM2
FKBP1A
BCAR1
STAT6
EFNA1
ID2
Protein-Protein
Gene Regulation (from literature)
Gene Regulation (predicted from binding sites)
Indirect interaction (from Reactome)
G
DEFENSE_RESPONSE_TO_VIRUS
P < 2e-04
ECDF
Ranked value
H
CCLE Melanoma Elastic Net Predictions
SERPINE1 Log2 signal intensity
CCLE melanoma cell lines (N=61)
I
STK38L
CDKL1
STK10
PTK7
RPS6KA5
TBK1
hsa-miR-412
TGFBR2
hsa-miR-515-5p
ALDOC
ACSL5
BNIP3
NDRG1
BNIP3L
LOXL2
J
LOXIMVI
A2058
LM38
MNT1

Figure 21

Figure 21. Distinct Epigenetic Cell Fate Programs Specify TBK1/IKKε Addiction, Related to Figure 20

(A) Glucose, lactate, glutamine, and glutamate concentrations were determined from the medium of TBK1 inhibitor resistant and sensitive cell lines 8 hr after in culture using NOVA analyzer.

(B) S2N ratios for metabolites in TBK1 inhibitor resistant and sensitive cell lines in response to compound II exposure versus DMSO exposure for 2 hours.

(C) TCA cycle metabolites that are decreased (blue circles) or increased (orange circle) upon compound II exposure in TBK1 inhibitor sensitive cell lines. TCA cycle enzymes that are expressed lower in TBK1 inhibitor sensitive cell lines compared to resistant cell lines are labeled red.

(D) Caspase-3 and -7 activity was measured following exposure of TBK1 inhibitor sensitive cell lines to DMSO or compound II (1mM) with or without MOG (5 mM) for 24 hours. Bars indicate mean ± s.d. (n = 3). *P = 0.0147 and ***P < 0.0001, two-way ANOVA followed by Dunnett's multiple comparisons test).

(E) Caspase-3 and -7 activity was measured following exposure of TBK1 inhibitor resistant cell lines to DMSO or EZH2 inhibitors (2 mM) for 72 hours. Bars indicate mean ± s.d. (n = 3).

(F) First-degree network neighborhood of the gene products of SOX10 targets identified from ChIP-Seq and significantly upregulated in response to SOX10 depletion.

(G) Empirical cumulative distribution function (ECDF) plot of mRNA expression of "defense response to virus" related genes in siSOX10 (orange) versus the siControl treated MNT1 cells (blue).

(H) Distribution of Cancer Cell Line Encyclopedia (CCLE) melanoma cell lines based on the linear weighted sums of the individual gene expression values for each predictive feature (left y-axis) and the corresponding SERPINE1 $\log_2$ signal intensity values from microarray (right y-axis).

(I) FuSiOn analysis showing the TBK1 and TGFBR2 cluster.

(J) Heat map showing the p values derived from the Pearson correlation analysis of adjusted ion intensities.

CHAPTER THREE

DISCUSSION

Cutaneous melanoma and lung squamous cell carcinoma (LSCC) share the distinction of harboring the highest mutational burdens among all human tumors (Alexandrov et al., 2013; Lawrence et al., 2013). However, in stark contrast to the dearth of recurrent somatic alterations in LSCC, fully half of melanomas possess recurrent variants of the *BRAF* oncogene (*BRAF(V600)*) (Davies et al., 2002; Flaherty et al., 2012a). In consequence, this seemingly monolithic mechanistic subtype has rightfully been the object of intense targeted therapy (Flaherty et al., 2010; Larkin et al., 2014; Long et al., 2014b; Robert et al., 2015). The overall patient response frequency to targeted therapy is high (~50%) (Ahronian et al., 2015; Jain et al., 2015; Lito et al., 2013; Meador and Pao, 2015), yet intrinsic resistance, and ready emergence of acquired resistance, indicate that collateral genomic variation produces mechanistic diversity within the class of BRAF(V600) tumors. Consistent with this notion, we identified a cohort of 15 different context-specific genetic vulnerabilities, in melanoma cancer cell lines, that are individually linked to distinct genomic features detectable in tumors from melanoma patients. Collectively these target/biomarker relationships offer distinctive intervention strategies with potential relevance in ~20% of melanoma patients.

Among the detected biomarker associated vulnerabilities, addiction to the lineage-specific transcription factor SOX10 was strongly associated with genomic copy number driven

SOX10 gain-of-function in melanoma cancer cells and tumor samples. Genomic characterization of direct SOX10 target genes in melanoma cells revealed gene regulatory interactions that impact mitogenic signaling, mitosis, nutrient utilization, cell growth, and tissue lineage multipotency. Among these, MITF, GJB1, PLAT, CEACAM1, NARS2, ADSS, WBP11, and ERBB3, were significantly correlated with SOX10 expression in patient samples, and were individually required to support anchorage-independent melanoma colony formation. While MITF and ERBB3 are well-appreciated protumorigenic SOX10 target genes, the other members of this group highlight a striking diversity of protumorigenic activity engaged as a consequence SOX10 activity, some of which has never been described previously. For example, the gap junction protein GJB1 supports cytoplasmic communication between the lamellae of myelinating Schwann cells (Bicego et al., 2006) and is the second most commonly mutated gene (8.8%, (Szigeti et al., 2006)) in type 1 Charcot–Marie–Tooth disease (CMT1). Its participation in melanoma anchorage-independent growth indicates an obligatory contribution of cell-cell communication to 3-D colony formation. Germline mutations in the mitochondrial asparaginyl-tRNA synthetase, NARS2, cause Leigh syndrome (Simon et al., 2015), Alpers syndrome (Sofou et al., 2015) and are associated with Alzheimer's disease (Hong et al., 2012; Wang et al., 2015b). These diseases are consistent with mitochondrial respiratory chain deficiency, and may indicate an addiction to oxidative phosphorylation in SOX10-dependent melanoma. Of additional potential disease significance, natural catalytic null splice variants of NARS2 have been recently demonstrated to activate NF-κB (Lo et al., 2014)-- a key melanoma survival pathway. The carcinoembryonic antigen-related cell adhesion protein, CEACAM1, is a poor prognosis

marker in melanoma patients and accumulates with disease progression. Notably, CEACAM1 in activated T-cells oligomerizes with TIM-3 to induce tolerance, and co-blockade of CEACAM1 and TIM-3 enhances anti-tumor immune responses (Huang et al., 2015). Given the cancer cell-autonomous contribution of CEACAM1 to anchorage-independent growth, targeting the CEACAM1/TIM-3 axis for cancer immunotherapy may have a collateral benefit of direct reduction of tumor burden.

Analysis of the SOX10-responsive gene network in melanoma indicated a potent collaborative interaction with the MITF transcription factor-- both via direct activation of MITF by SOX10 and by co-occupancy of SOX10/MITF target gene promoters. A component of this network in melanoma tumors is the monomeric G protein RagD. While RagD is well appreciated for its contribution to nutrient dependent activation of mTOR, in SOX10-dependent melanoma cells, RagD supports cell survival through feedback activation of MITF nuclear translocation. This may reflect an ancestral mechanism of action conserved in yeast, and presents as a regulatory axis that can be considered for intervention strategies directed against the MITF transcription factor.

The stratification of melanoma cell lines based on SOX10 addiction lead to the discovery of 2 mechanistic subtypes associated with distinct pharmacological intervention opportunities and genomic features that specify subtype membership. The SOX10-dependent BRAF(V600) subtype predicts sensitivity to clinical BRAF and MEK inhibitors. Notably, we found the SOX10-independent targeted therapy resistant subtype to be selectively sensitive to chemical

inhibition of TBK1/IKKe kinase activity. Both subtypes can be simultaneously discriminated, from within melanoma cell line panels and melanoma patient cohorts, by a nearly bimodal 5-gene quantitative mRNA expression profile that is robust to measurement with multiple technical platforms. If verifiable in prospective human trials, these observations provide a path forward for biomarker-directed therapy by both predicting best responders to currently available MEK inhibitors and by detection of chemically targetable MEK-independent disease.

The host defense signaling kinases TBK1 and IKKε have been under consideration as an oncology targets since 2006- but biological features predictive of response to TBK1/IKKε inhibitors have been lacking. Biomarker-positive, BRAF/MEK-inhibitor resistant, melanoma now presents as an important therapeutic context for TBK1/IKKε inhibitors. Major tumorigenesis-associated TBK1/IKKε substrates include the innate immune transcription factors IRF3/7 (Fitzgerald et al., 2003; Sharma et al., 2003), the growth and survival kinases AKT and NF-κB, and the autophagy adaptor protein p62 (Pilli et al., 2012). Elevated TBK1 activity within the targeted therapy resistant/TBK1-dependent melanoma cohort was indicated by a qualitative enrichment of activating site phosphorylation (T172) on TBK1 relative to total TBK1 protein, and quantitative enrichment of IFR3/7 target gene expression. Selective biochemical response of biomarker positive, BRAF/MEK independent melanoma cell lines to TBK1/IKKε inhibition was indicated by suppression of AKT pathway activation only in that subtype. However, direct chemical inhibition of AKT or NF-κB was not sufficient to recapitulate selective toxicity observed with TBK1/IKKε inhibitors.

Of note, shotgun proteomic discovery efforts have implicated TBK1 as a suppressor of Hippo pathway activation (Couzens et al., 2013; Kim et al., 2013b). Importantly, the Hippo effector YAP has recently been demonstrated to promote resistance to RAF and MEK inhibition in multiple tumor types. We found that Hippo pathway activity is generally low among all melanoma cell lines tested, however, the TBK1/IKKε inhibitor sensitive subtype selectively responded to TBK1/IKKε inhibition by Hippo pathway activation. TBK1/IKKε likely supports melanoma cell survival by both activation of survival signaling and suppression of Hippo tumor suppressor pathway activity as combined inhibition of AKT and YAP/TAZ activity selectively induced apoptosis in the TBK1/IKKε inhibitor sensitive subtype. This combinatorial mechanism of action is likely preserved in vivo given the sensitivity of biomarker positive xenograft tumors to systemic delivery of TBK1/IKKε inhibitors.

The TBK1/IKKε-sensitive cohort includes both BRAF mutant and BRAF wild-type tumors and corresponds to an overarching gene regulatory phenotype reminiscent of host defense pathway activation and TGFβ-induced mesenchymal status. The presence of this expression signature in homogenous cancer cell line cultures and in melanoma tumors with low lymphocyte infiltration suggests this phenotype corresponds to a mechanistically distinct melanoma subtype that we refer to as “innate immune”. This subtype is enriched within both the “MITF-low” and “immune” expression subtypes currently defined by TCGA efforts. As would be expected from the nature of the biomarker features, we found that high lymphocyte infiltration can confound detection of the “innate immune” subtype using ensemble gene

expression measurements from patient samples-- a limitation that we expect to overcome by development of IHC markers.

We find that mechanistic establishment of the “innate immune” melanoma cell state appears to be a consequence of relaxed chromatin and the ensuing release of TGFβ and host defense pathway activation. Importantly, artificially inducing this cell state by exposure to EZH2 inhibitors can be sufficient to establish TBK1/IKKε-addiction in otherwise resistant melanoma cells. Remarkably, delineation of the SOX10 regulatory space indicated that development of a melanomagenic program with or without SOX10 may play a major role in determining BRAF/MEK versus TBK1/IKKε sensitivity. A key discriminatory element appears to be SOX10-dependent suppression of NNMT and TGFBR2 expression, two gene products which can otherwise collaborate within a feed-forward regulatory loop (Chambers et al., 2003; Hsu et al., 2012; Ulanovskaya et al., 2013) to establish the relaxed chromatin; “mesenchymal” expression signature; and TBK1 pathway activation we observe within the “innate immune” subtype. As mentioned above, an additional functionally relevant component of the TBK1/IKKε-sensitive cell state is TBK1/IKKε-dependent YAP pathway activation. Though we, and others, can detect both physical and functional interactions between TBK1, LATS, and YAP1, we have not yet defined the mechanism by which TBK1/IKKε participate in Hippo pathway regulation. However, compelling observations in drosophila (Ohsawa et al., 2012), non small cell lung cancer (Serresi et al., 2016), and aggressive glioma (Bhat et al., 2011) suggest an interplay among mitochondrial damage (Ohsawa et al., 2012), TGFβ-induced actin remodeling (Cantelli et al., 2015), and loss of

PRC2 activity (Serresi et al., 2016) can all generate cell states that are permissive to YAP activation.

In summary, we find that cell-based exploration of melanoma intervention opportunities can be a rich source for target discovery given sufficient resolution of molecular correlates that are preserved in patient populations. Here, these efforts have nominated new biomarker-coupled target opportunities for mechanistic subtypes of BRAF mutant and wild-type melanomas; identified key elements within the SOX10 regulatory network required to support tumorigenicity; produced molecular predictors of best responders to BRAF(V600) targeted therapy; and delivered strategies to predict and chemically address non-responders.

CHAPTER FOUR

EXPERIMENTAL PROCEDURES

Cell Lines and Culture Conditions

Accurate provenance of all cell lines is followed using the PowerPlex 1.2 microsatellite detection kit (Promega) and fingerprint library maintained by the Minna/Gazdar laboratory and the ATCC. Primary melanoma cells from patient derived xenografts (PDXs) were kindly provided by Sean Morrison (University of Texas (UT) Southwestern Medical Center, Dallas, TX) and maintained in PRIME-XV Tumorsphere Serum Free Media (IrvineScientific) supplemented with serum free B-27 Supplement (50X) (Invitrogen). Chemical sensitivity testing was carried out in Dulbecco's modified Eagle's medium (DMEM, Invitrogen) supplemented with 10% fetal bovine serum (FBS, Atlanta Biologicals) and penicillin (100 units/mL) and streptomycin (0.1 mg/mL) (1% PenStrep) (GIBCO). MNT1 cells were a kind gift from Michael Marks (University of Pennsylvania). LM17, LM17R, LM20 and LM38 were kind gifts from Monica Rodolfo (Fondazione IRCCS Istituto Nazionale Tumori, Milan, Italy). WM3211 cells were a kind gift from Meenhard Herlyn (Wistar Institute, Philadelphia, PA). WW165, YUMAC and YUSIT1 were purchased from the Yale Skin Disease Research Center. LOXIMVI, M14, UACC257, UACC62, A375, MALME3M, SKMEL2, SKMEL5 and SKMEL28 were from NCI60 (National Cancer Institute, Bethesda, MD). A2058, RPMI7951, A101D, SKMEL31, COLO829, MEWO, HMCB, CHL1, Hs600.T, Hs895.T, Hs934.T, Hs839.T and Hs940.T were purchased from the ATCC. COLO792 was purchased

from Sigma-Aldrich. All established cutaneous melanoma cell lines were cultured in DMEM supplemented with 10% FBS and 1% PenStrep with the exception of COLO829, COLO792, SKMEL2, SKMEL5, LM17, LM17R, LM20 and LM38 (cultured in RPMI 1640 (Invitrogen) supplemented with 10% FBS and 1% PenStrep), RPMI7951 (cultured in MEM (Invitrogen) supplemented with 10% FBS and 1% PenStrep) and SKMEL31, MEWO and HMCB (cultured in EMEM (ATCC) supplemented with 10% FBS and 1% PenStrep). Uveal melanoma cell lines OCM3 and OCM8 were kindly donated by June Kan-Mitchell (Wayne State University, Detroit, MI), 92.1 was kindly donated by Gregorius P. M. Luyten (Leiden University Medical Centre, Leiden, Netherlands), MEL270, MEL285, MEL290, OMM2.3, MEL202, OMM2.5 were kindly donated by Timothy J. Murray (Bascom Palmer Eye Institute, Miami, FL) and OM431 was kindly donated by Jerry Niederkorn (UT Southwestern Medical Center, Dallas, TX). All uveal melanoma cell lines were cultured in RPMI 1640 (Invitrogen) supplemented with 10% FBS, 1% PenStrep, 1mM sodium pyruvate (Sigma), 2.5mg/ml amphotericin B (HyClone) and 55mM 2-mercaptoethanol (Gibco). Neonatal human epidermal melanocytes from a lightly pigmented donor (HEMn-LP) were purchased from Invitrogen and immortalized by ectopic expression of hTERT and human papilloma virus, HPV16 E6/E7 protein (Eskiocak et al., 2014). The resulting immortalized human melanocytes were cultured in Medium 254 (Invitrogen) supplemented with human melanocyte growth supplement (HMGS) (Invitrogen) and 1% PenStrep. Human bronchial epithelial cells (HBEC3, HBEC30 and HBEC34) were isolated from three patients and immortalized by ectopic expression of CDK4 and hTERT (Ramirez et al., 2004). Growth media was Keratinocyte-SFM medium supplemented with human recombinant Epidermal

Growth Factor 1-53 (EGF 1-53), Bovine Pituitary Extract (BPE) (Invitrogen) and 1% PenStrep. U2OS GFP-LC3 cells were cultured in DMEM, 10% FBS, penicillin (100 U/ml), streptomycin (0.1 mg/ml), 1 mg/ml G418 and 5 mg/ml blasticidin.

Reagents

Antibodies were from Cell Signaling Technology (Cleaved-PARP, PCNA, MET, MET-pY1003, MET-pY1234/1235, MET-pY1349, ERBB3, AKT, AKT-pS473, AKT-pT308, S6, S6-pS235/236, NOTCH1, ERK1/2, TBK1, TBK1-pS172, LATS1, LATS1-pT1079, GAPDH, MEK1/2, MEK1/2-pS217/221, EZH2, JARID2, H3K27me3, H3K9me2, AMPKα, AMPKα-pT172, p70 S6 kinase, p70 S6 kinase-pT389, mTOR-pS2448, LKB1, LKB1-pS428, Raptor-pS792, ACC, ACC-pS79, ULK1-pS555, COX IV and ERK1/2-pThr202/Tyr204), Santa Cruz Biotechnology (SOX10, MITF, ERRα, VDAC1/2/3, Cytochrome C, BCL2 and TOM20), Sigma-Aldrich (ACTB), Invitrogen (BrdU), Abcam (NNMT). All the siRNAs were purchased from Dharmacon and Ambion. Vemurafenib and BEZ235 were purchased from LC Laboratories. Trametinib, MK2206, Momelotinib, WZ4003, GSK126 and EPZ-6438 were purchased from Selleckchem. BX795 and MRT67307 were purchased from EMD Millipore. BMS345541, LY29400, AntimycinA, Piericidin A, XCT 790, Rapamycin and Compound C were purchased from Sigma-Aldrich. Necrostatin-1 was purchased from Enzo Life Sciences. U0126 was purchased from Cell Signaling Technology. AICAR was purchased from Toronto Research Chemicals. HTH01015 was purchased from ApexBio. PF-

562271 was a kind gift from Pier Paolo Scaglioni (UT Southwestern Medical Center, Dallas, TX). Recombinant human TGFb-1 was purchased from Peprotech.

Compound II Synthesis

Compound II synthesis was a modification of that previously described (Ou et al., 2011).

All reactions were carried out under nitrogen atmosphere with dry solvents under anhydrous conditions, unless otherwise noted. Anhydrous solvents were obtained by passing them through commercially available alumina columns (Innovative Technology, Inc., MA). All reagents were commercial compounds of the highest purity available. Analytical thin layer chromatography (TLC) was performed on aluminum plates with Merck Kieselgel 60F254 and visualized by UV irradiation (254 nm) or by staining with a solution of phosphomolibdic acid. Flash column chromatography was carried out using Merck Kieselgel 60 (230– 400 mesh) under pressure. Infrared spectra were obtained on a Perkin-Elmer I1000 FTIR series, from a thin film deposited onto a NaCl glass. ^{1}H NMR spectra were recorded in $CDCl_3$ and $(CD_3)_2SO$ at ambient temperature on a Varian Inova-400 spectrometer at 400 MHz with residual protic solvent as the internal reference ($CDCl_3$, d_H = 7.26 ppm; $(CD_3)_2SO$, d_H = 2.50 ppm); chemical shifts (*d*) are given in parts per million (ppm), and coupling constants (*J*) are given in Hertz (Hz). The proton spectra are reported as follows: d (multiplicity, coupling constant *J*, number of protons). The following abbreviations were used to explain the multiplicities: b = broad, d = doublet, m = multiplet, s = singlet, t = triplet. ^{13}C NMR spectra

were recorded in $CDCl_3$ and $(CD_3)_2SO$ at ambient temperature on the same spectrometer at 100 MHz with the central peak of $CDCl_3$ (d_C = 77.0 ppm) or $(CD_3)_2SO$ (d_C = 32.5 ppm) as the internal reference. Electrospray ionization mass spectra (ESI-MS) were recorded on a Shimadzu 2010-LCMS. Microwave reactions were carried out on a Biotage® Initiator Classic.

Note: Compound numbering according to Supplemental Figure 5.

2,3-Dimethoxyphenol (2) (McElroy and DeShong, 2006), 2,3-dimethoxyphenyl benzenesulfonate (3) (Cooper et al., 2006), 2,3-dimethoxyphenyl benzenesulfonate (4) (Cooper et al., 2006), 2,3-dimethoxy-5-nitrophenol (5) (Cooper et al., 2006) and 4-chloro-2-(methylthio)pyrimidine-5-carbaldehyde (10) (Su et al., 2014) were prepared following previously described procedures.

1-(3-Chloropropoxy)-2,3-dimethoxy-5-nitrobenzene (6). 1-Bromo-3-chloropropane (3.0 equiv, 387 mL, 3.92 mmol) was added to a solution of phenol 5 (1.0 equiv, 0.26 g, 1.30 mmol) and K_2CO_3 (2.0 equiv, 0.36 g, 2.60 mmol) in DMF (8.0 mL) at 23 ºC. The reaction was stirred for 10 h and then diluted with water (8.0 mL). The mixture was extracted with EtOAc (10 mL x 3), and the combined organic extracts were washed with brine (20 mL), dried over anhydrous $MgSO_4$ and filtrated. The solvent was concentrated under reduced pressure, and the residue was purified by flash chromatography (SiO_2, 85/15 hexane/EtOAc) to afford 300 mg (84%) of 6 as a yellow oil. *Rf* = 0.15 (85/15 hexane/EtOAc); IR (cm^{-1}) 3107, 2943, 1619, 1520, 1496, 1426, 1339, 1318, 1241; ^1H NMR (400 MHz, $CDCl_3$, 25 °C): δ 7.54 (d, *J* = 2.6 Hz, 1H), 7.52 (d, *J* = 2.6 Hz, 1H), 4.24 (t, *J* = 6.0 Hz, 2H), 3.94 (s, 3H),

3.93 (s, 3H), 3.79 (t, J = 6.0 Hz, 2H), 2.32 (quin, J = 6.0 Hz, 2H) ppm; ^{13}C NMR (100 MHz, $CDCl_3$, 25 °C): δ 152.9, 151.8, 143.9, 143.2, 102.4, 101.2, 65.8, 60.9, 56.3, 41.1, 31.8 ppm. MS (ESI^+) m/z calcd. for $C_{11}H_{15}ClNO_5$ $[M + H]^+$ 276.1; found: 276.1.

1-(3-(2,3-Dimethoxy-5-nitrophenoxy)propyl)-4-methylpiperazine (7). 1-Methylpiperazine (5.0 equiv, 600 mL, 3.41 mmol) was added to a solution of chloride 6 (1.0 equiv, 0.30 g, 1.08 mmol) and NaI (0.1 equiv, 16 mg, 0.11 mmol) in DMF (7.0 mL) at 23 ºC. The reaction was heated for 5 h at 80 ºC and then quenched with satd. aqueous NaHCO3 (2.0 mL). The mixture was extracted with EtOAc (10 mL x 3), and the combined organic extracts were washed with brine (20 mL), dried over anhydrous $MgSO_4$ and filtrated. The solvent was concentrated under reduced pressure, and the residue (315 mg, 85%, yellowish oil) was used in the next step without further purification. Rf = 0.20 (90/10 CH_2Cl_2/MeOH); IR (cm^{-1}) 2939, 2795, 1619, 1524, 1496, 1338, 1316, 1124; ^{1}H NMR (400 MHz, $CDCl_3$, 25 °C): δ 7.53 (d, J = 2.6 Hz, 1H), 7.50 (d, J = 2.6 Hz, 1H), 4.14 (t, J = 6.8 Hz, 2H), 3.93 (s, 6H), 2.60 – 2.36 (m, 8H), 2.55 (t, J = 6.8 Hz, 2H), 2.29 (s, 3H), 2.04 (quin, J = 6.8 Hz, 2H) ppm; ^{13}C NMR (100 MHz, $CDCl_3$, 25 °C): δ 152.7, 152.0, 143.7, 143.1, 102.2, 100.8, 67.6, 60.8, 56.2, 54.9 (2C), 54.6, 53.0 (2C), 45.8, 26.3 ppm. MS (ESI^+) m/z calcd. for $C_{16}H_{26}N_3O_5$ $[M + H]^+$ 340.2; found: 340.2.

3,4-Dimethoxy-5-(3-(4-methylpiperazin-1-yl)propoxy)aniline (8). Fe (5.0 equiv, 1.2 g, 22.1 mmol) was added to solution of nitrobenzene 7 (1.0 equiv, 1.5 g, 4.42 mmol) in satd. aqueous NH_4Cl (28.0 mL) and EtOH (44.0 mL) at 23 ºC. The reaction was stirred and heated at 100 ºC for 2 h. The solution was filtered through celite and washed thoroughly with CH_2Cl_2. The

combined organic extracts were washed with brine (20 mL), dried over anhydrous $MgSO_4$ and filtrated. The solvent was concentrated under reduced pressure, and the residue (1.3 g, 95%, brownish solid) was used without further purification. *Rf* = 0.15 (90/10 CH_2Cl_2/MeOH); m.p. = 54 -56 ºC; IR (cm^{-1}) 3355, 3223, 2939, 2805, 1605, 1506, 1464, 1284, 1235; ^1H NMR (400 MHz, $CDCl_3$, 25 °C): δ 5.93 (d, J = 2.6 Hz, 1H), 5.91 (d, J = 2.6 Hz, 1H), 4.00 (t, J = 6.8 Hz, 2H), 3.80 (s, 3H), 3.74 (s, 3H), 3.51 (b, 2H), 2.55 – 2.36 (m, 8H), 2.54 (t, J = 6.8 Hz, 2H), 2.28 (s, 3H), 1.99 (quin, J = 6.8 Hz, 2H) ppm; ^{13}C NMR (100 MHz, $CDCl_3$, 25 °C): δ 153.7, 153.0, 142.7, 130.8, 93.8, 92.6, 66.9, 60.8, 55.7, 54.9 (3C), 53.0 (2C), 45.9, 26.6 ppm. MS (ESI^+) m/z calcd. for $C_{16}H_{28}N_3O_3$ $[M + H]^+$ 310.2; found: 310.2.

1-(4-Methoxyphenyl)-6-(methylsulfonyl)-1H-pyrazolo[3,4-d]pyrimidine (11). Triethylamine (2.1 equiv, 310 mL, 2.22 mmol) was added to a solution of aldehyde 10 (1.0 equiv, 0.20 g, 1.06 mmol) and (4-methoxyphenyl)hydrazine (2.0 equiv, 293 mg, 2.12 mmol) in THF (2.5 mL) at 23 ºC. After stirring for 30 min, the mixture was heated at 150 ºC under microwave irradiation for 1 h. The solvent was concentrated under reduced pressure, and the residue was passed through silica gel and eluted with 80/20 hexane/EtOAc to afford 200 mg (69%) of an orange solid. The solid was dissolved in CH_2Cl_2 (6.0 mL) and 3-chloroperoxybenzoic acid (3.0 equiv, 493 mg, 2.20 mmol) was subsequently added at 23 ºC. After stirring for 2 h, the reaction was quenched with satd. aqueous $NaHCO_3$ (5.0 mL) and extracted with CH_2Cl_2 (10 mL x 3). The combined organic extracts were washed with brine (20 mL), dried over anhydrous $MgSO_4$ and filtrated. The solvent was concentrated under reduced pressure, and the residue was purified by flash chromatography (SiO_2, from 70/30 hexane/EtOAc to 100%

EtOAc) to afford compound 11 (163 mg, 73%) as an orange solid. *Rf* = 0.2 (60/40 hexane/EtOAc); m.p. = 144 - 147 ºC; IR (cm^{-1}) 3009, 2932, 2840, 1515, 1385, 1312, 1251, 1122; ^{1}H NMR (400 MHz, $CDCl_3$, 25 °C): δ 9.40 (s, 1H), 8.46 (s, 1H), 8.07 (d, *J* = 9.6 Hz, 2H), 7.09 (d, *J* = 9.6 Hz, 2H), 3.90 (s, 3H), 3.45 (s, 3H) ppm; ^{13}C NMR (100 MHz, $CDCl_3$, 25 °C): δ 162.5, 158.9, 153.8, 150.6, 134.0, 130.8, 123.0 (2C), 116.6, 114.5 (2C), 55.5, 39.5 ppm. MS (ESI^+) m/z calcd. for $C_{13}H_{13}N_4O_3S$ $[M + H]^+$ 305.1; found: 305.1

N-(3,4-Dimethoxy-5-(3-(4-methylpiperazin-1-yl)propoxy)phenyl)-1-(4-methoxyphenyl)-1*H*-pyrazolo[3,4-*d*]pyrimidin-6-amine (12). A solution containing aniline 8 (1.0 equiv, 277 mg, 0.89 mmol), sulfone 11 (1.1 equiv, 298 mg, 0.98 mmol) and triethylamine (1.1 equiv, 136 mL, 0.98 mmol) in 3-methyl-3-pentanol (4.0 mL) was heated at 150 ºC under microwave irradiation for 4 h. The reaction was diluted with water (5.0 mL) and extracted with 3/1 CH_3Cl/2-propanol (10 mL x 3). The combined organic extracts were dried over anhydrous $MgSO_4$ and filtrated. The solvent was concentrated under reduced pressure, and the residue was purified by flash chromatography (SiO_2, from 95/5 CH_3Cl/MeOH to 90/10 CH_3Cl/MeOH in 1% of NH_4OH) to afford 12 (175 mg, 37%) as a yellowish solid. *Rf* = 0.18 (90/9/1 CH_3Cl/MeOH/NH_4OH); m.p. = 44 -47 ºC; IR (cm^{-1}) 3338, 2938, 2802, 1598, 1567, 1506, 1429, 1416, 1298, 1248, 1124; ^{1}H NMR (400 MHz, $((CD_3)_2SO_2$, 25 °C): δ 9.88 (s, 1H), 9.07 (s, 1H), 8.29 (s, 1H), 7.95 (d, *J* = 8.8 Hz, 2H), 7.28 (d, *J* = 2.0 Hz, 1H), 7.20 (d, *J* = 2.0 Hz, 1H), 7.10 (d, *J* = 8.8 Hz, 2H), 3.90 (t, *J* = 6.0 Hz, 2H), 3.83 (s, 3H), 3.71 (s, 3H), 3.63 (s, 3H), 2.39-2.14 (m, 10H), 2.11 (s, 3H), 1.83 (quin, *J* = 7.2 Hz, 2H) ppm; ^{13}C NMR (100 MHz, $(CD_3)_2SO_2$, 25 °C): δ 158.2, 157.6, 154.5, 153.0, 152.7, 152.0, 136.0, 134.9, 132.9,

131.6, 123.2 (2C), 114.2 (2C), 109.3, 97.8, 96.8, 66.5, 60.1, 55.7, 55.4, 54.7 (2C), 54.3, 52.7 (x2), 45.7, 26.3 ppm. MS (ESI^+) m/z calcd. for $C_{28}H_{36}N_7O_4$ $[M + H]^+$ 534.3; found: 534.3.

siRNA Screens

An arrayed whole genome siRNA library (21,125 genes; 4 siRNA duplexes per gene) was purchased from Dharmacon in 96-well microtiter plate format. A single agent viability siRNA screen was carried out in MNT1 cells as described (Ganesan et al., 2008). siRNAs were reconstituted in 1X siRNA buffer (Dharmacon) to a final concentration of 10 mM overnight at 4^{o}C and stored at -80^{o}C prior to use. Reverse transfection was performed by transferring 30 pmole (3 mL) of each siRNA pool into 65 mL of OpTiMEM in 96-well round-bottom plates (Greiner BioOne), then transferring 20 mL of this siRNA solution to the 96-well optical assay plates (Costar) in triplicates. After 5 min of incubation, RNAiMAX was added into the solution at a 0.2% final concentration per well. siRNA and RNAiMAX mixture was incubated for 20 min. In parallel cells were harvested and diluted, then added to the siRNA-lipid mixture (10K cells/well, MNT1) and incubated for 96 hours. CellTiter-Glo reagent (Promega) was added and mixed for 2 min on a plate shaker followed by incubation for 10 min at room temperature. Luminescence was determined using an EnVision multilabel plate reader. To correct position and batch effects, primary screen values were row and column median normalized and $\log_2$ transformed. Mean values were used to calculate batch-centered Z-scores using siMacro (Singh et al., 2013). A total of 60 “hits” (RNAi toxicity screen z-score<-2.5 and detectable copy number gain in patients) were resupplied in 4X1

duplex format from Dharmacon. Transfection conditions employing RNAiMax were optimized for each cell line using siUBB and siLONRF1 as positive and negative controls respectively. Secondary screen data were normalized using negative control oligos in each plate.

Copy Number Variation Annotation in Melanoma Tumors

Genomic DNA from patient melanoma tumor samples were processed, labeled and hybridized to Agilent CGH 244K arrays. Copy number gain was defined as $\log_2 \geq 0.4$ in tumor versus matched normal tissue (Figure 1A). Genomic Identification of Significant Targets in Cancer (GISTIC) (Mermel et al., 2011) was used to do copy number variation (CNV) analyses and selecting meaningful amplifications from random events (Figure 1G). Pearson correlation was used to calculate the correlation between DNA amplifications and matched expression data to identify copy number driven (CND) genes.

BrdU Incorporation Assays

For cell proliferation assays, BrdU (10 mM) was added 56 hr post-transfection in 96-well plates and incubated for 16 hr. Cells were then washed with warm Dulbecco's Phosphate Buffered Saline (DPBS) (Fisher Scientific), and fixed with formaldehyde (3.7% in warm DPBS) for 20 min. After washing with DPBS, DNA was denatured with HCl (2 N) for 30 min at 37^{o}C and neutralized with borate buffer (0.1 M, pH 8.5) for 10 min at room

temperature. Cells were then permeabilized with PBST (0.1% Triton X-100 in PBS) for 10 min, washed twice with PBS, and blocked in BSA (3% in PBST) for 30 min. BrdU antibody conjugated to Alexa488 was used at 1:200 in 3% BSA for 1 hr at room temperature. Nuclei were counterstained with Hoechst 33342 (Invitrogen). Images of each well were acquired using a BD Pathway 855 microscope and analyzed using BD AttoVision software (BD Biosciences). Percent BrdU incorporation was calculated by dividing the number of BrdU positive cells by the number of Hoechst positive cells. Data were then normalized using the negative control oligos in each plate.

Soft Agar Colony Formation Assay

For anchorage-independent growth assays, cells were reverse transfected in 96-well plates. 24 hr post-transfection, cells were harvested and resuspended in 0.375% agar (Noble agar, Difco) pre-equilibrated with growth medium and then seeded at a clonal density (n = 400/well, 96-well plates or n = 1500/well, 24-well plates (Figure 1F)), on top of a 0.75% bottom agar layer in each well of 96-well plate or 24-well plate. Colonies were allowed to form for 28 days (MNT1), 16 days (WW165) or 21 days (Figure 1F) with intermittent medium supplementation (a few drops twice a week). Pictures were taken using Zeiss SteREO microscope, and colonies were counted under a light microscope or using Image J software (Figure 1F).

SOX10 DNA Copy Number Analysis

Droplet Digital PCR (ddPCR) (Bio-RaD) was used to detect SOX10 DNA copy number. Genomic DNA was isolated from melanoma cell lines using DNeasy Blood & Tissue Kit (QIAGEN). Genomic DNA, ddPCR master mix and TaqMan Copy Number Assay for human SOX10 (Applied Biosciences) were mixed according to the manufacturer's protocols. To generate droplets 70 mL of droplet generator oil (BioRad) was added to the cartridge oil lane (BioRad), then 20 mL of PCR reaction was added to the center well. Cartridge gasket (BioRad) was then placed onto the droplet generator cartridge to form droplets. Droplets were then transferred to a PCR plate. A standard curve was generated using the SOX10-BAC clone. SOX10 DNA copy number was calculated for each cell line using the standard curve followed by normalization to immortalized human melanocytes.

SOX10 ChIP-Seq and Associated Data Analytics

We generated a SOX10-LAP BAC transgenic MNT1 cell line as previously described (Hua et al., 2009; Kittler et al., 2013; Poser et al., 2008). The SOX10-LAP BAC was obtained by recombineering of the BAC clone RP11-834N13 (purchased from Invitrogen) with a LAP-IRES-Neo/Kan cassette tagged with homology arms using two oligonucleotides (5'-CCCCACACACTGGGAGCAGCCAGTATATACGACACTGTCCCGGCCCGATTATGATATTCCAACTACTGCA-3'; 5'-CAGGCTGGGGGCAGGGGCTGGGCGGGGGGTGGTGGCGACAGGGCCCCCTTCAG

AAGAACTCGTCAAGAAG-3'). MNT1 cells were transfected with 1 µg BAC DNA using Effectene (QIAGEN), and cells expressing SOX10-LAP were selected with geneticin (500 µg/ml). BAC transgenic cells at 80% confluency (~$1x10^7$) were cross-linked with 1% formaldehyde for 10 minutes at 37°C, and quenched with 125 mM glycine at room temperature for 5 minutes. The fixed cells were washed twice with cold PBS, scraped, and transferred into 1 ml PBS containing protease inhibitors (Roche). After centrifugation at 700 g for 4 minutes at 4°C, the cell pellets were resuspended in 100 µl ChIP lysis buffer (1% SDS, 10 mM EDTA, 50 mM Tris-HCl [pH 8.1] with protease inhibitors) and sonicated at 4°C with a Bioruptor (Diagenode) (30 seconds ON and 30 seconds OFF at highest power for 15 minutes). The sheared chromatin with a fragment length of ~200 – 600 bp) was centrifuged at 20,000 g for 15 minutes at 4°C). 100 µl of the supernatant was used for ChIP or as input. A 1:10 dilution of the solubilized chromatin in ChIP dilution buffer (0.01% SDS, 1.1% Triton X-100, 1.2 mM EDTA, 167 mM NaCl 16.7 mM Tris-HCl [pH 8.1]) was incubated at 4°C overnight with 6 µg/ml of a goat anti-GFP (raised against His-tagged full-length eGFP and affinity-purified with GST-tagged full-length eGFP). Immunoprecipitation was carried out by incubating with 40 µl pre-cleared Protein G Sepharose beads (Amersham Bioscience) for 1 hour at 4°C, followed by five washes for 10 minutes with 1ml of the following buffers: Buffer I: 0.1% SDS, 1% Triton X-100, 2 mM EDTA, 20 mM Tris-HCl [pH 8.1], 150 mM NaCl; Buffer II: 0.1% SDS, 1% Triton X-100, 2 mM EDTA, 20 mM Tris-HCl [pH 8.1], 500 mM NaCl; Buffer III: 0.25 M LiCl, 1% NP-40, 1% deoxycholate, 1 mM EDTA, 10 mM Tris-HCl [pH 8.1]; twice with TE buffer [pH 8.0]. Elution from the beads was performed twice with 100 µl ChIP elution buffer (1% SDS, 0.1 M NaHCO3) at room

temperature (RT) for 15 minutes. Protein-DNA complexes were de-crosslinked by heating at 65°C in 192 mM NaCl for 16 hours. DNA fragments were purified using QiaQuick PCR Purification kit (QIAGEN) and eluted into 30 µl H_2O according to the manufacturer's protocol after treatment with RNase A and Proteinase K. For ChIP-Seq, barcoded libraries of SOX10-LAP ChIP and input DNA were generated with the TruSeq® ChIP Sample Preparation Kit (Illumina), and 50-nt single-end reads were generated with the HiSeq2000 system (Illumina). Sequence reads were aligned to the human reference genome (hg19) using Bowtie (v.0.12.7) (Langmead et al., 2009). Uniquely mapped reads with ≤2 mismatches to the reference sequence were retained for further analysis; for SOX10-LAP we obtained 23,375,102 reads and for input 20,961,448 reads. For normalization of Wig files we used the wignorm executable provided in MACS software tools to determine the background signal in the input sample and subtracted it from the ChIP signal. We used the fold-change between the ChIP signal and the input signal as the score to build a single wig track to represent the binding strength. This score was used to construct the UCSC browser tracks. For ChIP-Seq peak annotation the Model-based Analysis of ChIP-Seq (MACS) software tool (v.1.4.2) (Zhang et al., 2008) was used to identify SOX10-occupied regions from ChIP-Seq data with 200 bp as the fragment length and read shifting by 100 bp to identify candidate peaks with significant tag enrichment. MACS uses a Poisson distribution model to calculate the significance (p-value) of these peaks. Default parameters of MACS were used for the analyses in our study to quantify the SOX10 ChIP signal fold enrichment over input sample in each region with increased SOX10 occupancy (i.e. peaks), providing this value in the peak file. A false discovery rate (FDR) cutoff of 5% was used to select peaks for further analysis.

For annotation of SOX10 binding regions we used annotatePeaks function in Homer tools (Heinz et al., 2010) to assign SOX10 binding regions relative to their specific positions in the genome. This function takes the peak coordinates, tag directories as input and extends each tag by their estimated ChIP-fragment length, calculates ChIP fragment coverage represented in per basepair per peak. We used 2500 bp regions flanking the SOX10 peak summits to generate heatmap showing SOX10 ChIP signal across all binding regions. We used CEAS tool (Shin et al., 2009) to annotate the binding sites distributed over important genomic features such as promoter, downstream of transcription termination site, untranslated region (UTR), exons and introns. For *de novo* motif discovery in SOX10-bound regions in melanoma cells we used the Multiple EM for Motif Elicitation (MEME) software tool. MEME uses a multiple sequence alignment approach to identify repeated ungapped sequence patterns in the input DNA with statistical significance (Bailey et al., 2006). We retrieved 200 bp sequence (i.e. 100 bp sequence flanking the peak summits 3' and 5') as input for MEME. From the MEME prediction results, highly enriched motif in terms of number of sites and E-values were selected and then mapped against the transcription factor annotation databases JASPAR (Sandelin et al., 2004) and TRANSFAC (Wingender et al., 1996) using TOMTOM suite (Gupta et al., 2007). TOMTOM identifies transcription factors (TF) position weight matrices (PWMs) also known as motifs similar to the MEME predicted motif. For ChIP-Seq data of high quality we expect to identify known motifs for the analyzed transcription factor with this approach, which is critical to proceed with downstream analyses. For target gene analysis potential protein-coding target genes associated with SOX10 binding regions were identified based on the distance of their transcription start sites (TSSs) (obtained from the

human RefSeq annotation assembly, hg19) to SOX10 occupied peak summits. All genes whose TSSs were within 50 kb distance were called as candidate SOX10 target genes. Also, if no gene was identified within 50 kb distance, the gene with the nearest TSS was considered a candidate SOX10 target. For expression correlation analysis we used Spearman correlation to identify significantly ($P<0.01$) correlated SOX10 putative targets (identified from ChIP-Seq and significantly ($P<0.008$) downregulated in response to SOX10 depletion) with SOX10 using the whole transcript profiles of patient samples in three independent data sets (Melanoma Vienna II, GSE3189 and GSE8401 (Xu et al., 2008)).

Whole Genome Transcript Analysis

Total RNA was isolated with RNeasy Plus Mini Kit (Qiagen) from proliferating melanoma cell cultures or MNT1 melanoma cells 48 hours post siRNA transfection as indicated. All expression profiles were measured with the HumanHT-12 v4 BeadChip. For background noise detection and correction we employed a non-parametric version of model-based background correction method (MBCB), which uses an extended model of robust multi-array analysis (RMA) that incorporates information from negative control beads (Xie et al., 2009). The background-corrected data was then subjected to quantile normalization to obtain identical sample distributions. To assess the differential expression between samples, we used the linear models for microarray data (LIMMA) method (Smyth, 2004). LIMMA is specialized to minimize the standard error, for sparse sample matrices, by using an empirical Bayes method to compute the statistical significance and the fold change between two classes

of samples. P values for expression changes were computed and adjusted for multiple hypothesis testing (Smyth, 2004).

qRT PCR

For melanoma cell lines total RNA was isolated with RNeasy Plus Mini Kit (QIAGEN). Complementary DNA (cDNA) was synthesized with Transcriptor First Strand cDNA synthesis kit (Roche). QPCR was performed by either Solaris (Dharmacon) or Taqman (Applied Biosystems) assays for the indicated genes. ACTB was used to normalize RNA input. For melanoma clinical specimens qPCR was performed on resected tumors from patients undergoing BRAF(V600) (vemurafenib, dabrafenib) +/- MEK (trametinib) inhibitor therapy at pre-treatment (day 0) and on-treatment (10-14 days following treatment initiation). Tissue was processed with disruption by mortar and pestle followed by use of a QIAshredder (QIAGEN). Total RNA was isolated with QIAcube using the RNeasy Mini Kit (QIAGEN). Complementary DNA (cDNA) was synthesized with the SuperScript VILO cDNA Synthesis Kit (Invitrogen Life Technologies). QPCR was performed by Taqman (Applied Biosystems) assays for gene expression probes for RAC2 (Hs01036635_s1), NRP1 (Hs00826128_m1), MGC4294 (Hs01089157_s1), CTSV (Hs00952036_m1), FAM69B (Hs01060315_m1), ACTB (Hs01060665_g1). A375 resistant clones E and F were generated using the same protocol as in Smith, MP. et al., 2012. BRAF (V600E) A375 melanoma cells were exposed to cytotoxic concentrations of MEK inhibitor (PD184352, 1μM) for 4 days and then surviving colonies grown out, still in the presence of the drug (PD184352, 0.5μM).

PD184352 was purchased from Selleckchem. Total RNA was isolated using phenol/chloroform method using the TRIzol reagent (Invitrogen Life Technologies). Complementary DNA (cDNA) was synthesized with Omniscript reverse transcriptase kit (QIAGEN). QPCR was performed by either Solaris (Dharmacon) or Taqman (Applied Biosystems) assays for the indicated genes. ACTB was used to normalize RNA input.

Cell fractionation and Protein Analysis

Cells were lysed in 50 mM Tris (pH 6.8), 2% sodium dodecyl sulfate (SDS), and 10% glycerol. Samples were separated on SDS− polyacrylamide gels and transferred to polyvinylidene difluoride (PVDF) membranes for immunoblotting. NE-PER Nuclear and Cytoplasmic Extraction Reagents (Thermo Fisher) were used for nuclear-cytoplasmic fractionation assays. Lamin A/C and Histone H3 were used as nuclear loading controls, and GAPDH was used as cytoplasmic loading control.

In Vitro Binding Assays

Recombinant Rag proteins were purchased from Abnova. Recombinant karyopherin alpha 2 (KPNA2) delta form [ref] was a gift from Yuh Min Chook (UT Southwestern Medical Center). In vitro binding assays were performed by incubating 4 mg of KPNA2 delta protein and 4 mg of GST-tagged Rag proteins with Glutathione Sepharose beads 4B (GE Healthcare Life Sciences) for 1.5 hr in transport buffer (20 mM HEPES, 110 mM potassium acetate, 2 mM $MgCl_2$, and 0.1% Tween-20). After three washes in transport buffer, the proteins were eluted in SDS-sample buffer, boiled, subjected to SDS-PAGE, and blotted with anti-KPNA2 or anti-GST as a loading control.

Mitochondrial Membrane Potential and Mass Analyses

Cell were treated with either DMSO (0.5%) or XCT 790 (10 mM, 25 mM or 40 mM) for 15 minutes, then the growth medium removed and replaced with growth medium containing either DMSO (0.5%) or XCT 790 (10 mM, 25 mM or 40 mM) with MitoTracker CMXRos and MitoTracker Green FM probes from Invitrogen and incubated for another 15 minutes. Cells were then washed with warm growth medium, trypsinized, spun down, washed with cold PBS and resuspended in either FACS buffer (0.1% BSA, 10 mM HEPES pH 7.4, penicillin (100 U/ml) and streptomycin (0.1 mg/ml) in Leibowitz's L15 media) or PI/RNASE staining buffer from Invitrogen and immediately processed for fluorescence activated cell sorting (FACS) using FACSCalibur (BD Biosciences) and analyzed with FlowJo software.

Mitochondrial DNA Copy Number Analysis

Genomic DNA was isolated with DNeasy Blood and Tissue Kit (QIAGEN) from melanoma cells. QPCR was performed using the Human mitochondrial to nuclear DNA ratio kit (Clontech) and the Terra qPCR Direct SYBR Premix (Clontech). Primer sets were designed for specific detection two mitochondrial DNA targets (ND1 and ND5) and two nuclear DNA targets (SLCO2B1 and SERPINA1).

Mitochondrial Respiration Assays

Oxygen consumption rates (OCRs) were measured with an XF-24 Extracellular Flux Analyzer (Seahorse Bioscience). Cells were plated at 20K per well and cultured for 24 hours. Media was then exchanged with XF assay medium supplemented with 25 mM glucose, 2 mM glutamine, and 1 mM sodium pyruvate, and plates were inserted into calibrated XF sensor cartridges with preloaded oligomycin (1 mM final, mitochondrial H+-ATP-synthase inhibitor), FCCP (1 mM final, electron transport uncoupler via mitochondrial inner membrane permeabilization), rotenone/antimycin A (500 nM final, mitochondrial complex 1 and 3 inhibitors, respectively). All OCRs were normalized to cell number. Maximum respiratory capacity was measured by subtracting the mean OCR measurements after rotenone/antimycin A exposure (minimum OCR) from the mean OCR values after FCCP exposure (maximum OCR).

Metabolomics

Subconfluent cultures of TBK1 inhibitor resistant (SKMEL5, YUMAC, MNT1 and LM38) and TBK1 inhibitor sensitive melanoma cell lines (LOXIMVI, LM20, A2058 and RPMI7951) were exposed to compound II dissolved in DMSO or DMSO alone for 2 hours. Cells were then rinsed with ice-cold saline solution and the lysates were collected with 80% methanol on dry ice. Samples were snap frozen, and stored at -80°C. To extract metabolites, frozen samples were subjected to three freeze-thaw cycles between liquid nitrogen and a 37°C water bath. Samples were briefly vortexed and sedimented in a bench top centrifuge at 4°C for 15 minutes at 14,000xg. The supernatant, containing metabolites dissolved in methanol, was then dried using a SpeedVac and then suspended in 0.03% formic acid. The samples were vortexed, centrifuged at 14,000 rpm for 5 minutes at 4°C, and then analyzed using an AB SCIEX QTRAP 5500 LC/MS/MS system.

Metabolic Flux Analysis Using Isotope Tracing

Subconfluent cultures of TBK1 inhibitor resistant (SKMEL5 and MNT1) and TBK1 inhibitor sensitive melanoma cell lines (LOXIMVI and A2058) were incubated in D[U-^{13}C] glucose or D[U-^{13}C] glutamine containing media with exposure to compound II or DMSO carrier. At the indicated time-points, cells were washed with cold saline on ice and lysates were collected with 50% pre-cooled methanol in eppendorf tubes. Lysates were snap frozen in liquid nitrogen. Metabolites were extracted by three freeze-thaw cycles. Precipitated proteins were removed by centrifugation. The samples were dried and derivatized by trimethylsilylation (Tri-Sil HTP reagent, Thermo Scientific). Metabolites were analyzed

using an Agilent 6970 gas chromatograph networked to an Agilent 5973 mass selective detector. ^{13}C enrichment analysis was performed as previously described (Cheng et al., 2011)

Nutrient Utilization and Metabolite Secretion Assay

Subconfluent cultures of TBK1 inhibitor resistant (YUMAC and MNT1) and TBK1 inhibitor sensitive melanoma cell lines (LOXIMVI and A2058) were cultured for 8 hours. Medium was then collected for bulk metabolic rate measurements, and cells were harvested for protein quantification with BCA assays. Concentrations of glucose, lactate, glutamine, and glutamate were determined from the medium using an automated electrochemical analyzer (BioProfile Basic-4 analyzer; NOVA) (Yang et al., 2009).

Protein Analysis

Cells were lysed in 50 mM Tris (pH 6.8), 2% sodium dodecyl sulfate (SDS), and 10% glycerol. Samples were separated on SDS− polyacrylamide gels and transferred to polyvinylidene difluoride (PVDF) membranes for immunoblotting. For TGFb stimulation, cells were serum-starved overnight followed by exposure to TGFb in serum-free media for 10 or 30 minutes and then lysed in 50 mM Tris (pH 6.8), 2% sodium dodecyl sulfate (SDS), and 10% glycerol.

Immunoprecipitation and Immunoblotting

$1x10^5$ LOXIMVI and MNT1 cells were seeded into 35 mm dishes. Next day, 500 ng of 3XFlag-TBK1 plasmid or empty vector were transfected with Fugene 6 at a ratio of 3:1 (ml Fugene 6 to mg DNA). 60 hours post transfection; cells were lysed in immunoprecipitation lysis buffer (20 mM Tris-HCl pH 7.4, 137mM NaCl, 1% Triton X-100, 0.5% sodium deoxycholate, 10mM MgCl2, 2mM EGTA) with protease and phosphatase inhibitors (Roche EDTA-free cOmplete ULTRA and PhosphoSTOP) for 30 min and then cleared at 16,000 X g for 10 min at 4°C. 1500 mg of lysate was brought to the concentration of 1mg/mL by diluting it with lysis buffer. The immunoprecipitation was carried out for 14 hours using 2.5 mg of monoclonal anti-Flag M2 (Sigma Catalog#F1804). Antibody-antigen complexes were precipitated with 60 ml Protein A/G-agarose beads (Santa Cruz Biotechnology, SC-2003) for 2 hours. Subsequently, complexes were washed in lysis buffer 4 times for 1 min at 4°C then eluted with 60ml 2X SDS sample buffer (BIORAD Catalog#161-0737) followed by boiling at 95°C for 12 min. Samples were subsequently separated by SDS− polyacrylamide gels and transferred to PVDF membranes for immunoblotting.

Sample Preparation, Data Acquisition and Data Processing for TMT-labeling and LC-MS/MS experiments

The mass spectrometry samples were prepared following the protocol as described previously (Erickson et al., 2015). Briefly, cells were harvested with SDS lysis buffer [1.0 %

SDS w/v, 10 mM HEPES pH 7.0, 2 mM MgCl2]. Benzonase (Sigma) was added to the samples to decrease the viscosity of the lysate. About 15 mg total protein from each sample was reduced with 5 mM DTT, and cysteine residues were alkylated with 20 mM iodoacetamide. Proteins were then extracted by methanol−chloroform precipitation and were subsequently washed with ice cold acetone. Pellets were dried and were resuspended in 8 M urea containing 10 mM Tris-Cl, 5 mM EDTA, pH 8.5. Proteins were digested with trypsin at a 1:100 ratio (enzyme : substrate). Digests were acidified with 200 mL of 20 % formic acid (FA) to achieve a final pH of ~2 and were subjected to desalting using C18 solid-phase extraction (SPE) cartridges (Sep-Pak, Waters, Milford, MA).

To enrich the phosphopeptides, tryptic peptides (~10 mg per TMT channel) were resuspended in 1 mL of 2 M lactic acid/ 50% acetonitrile (ACN) then centrifuged at 15,000g for 20 min. Supernatants were then mixed with 15 mg of titanium dioxide beads (GL Sciences, Japan), and were vortexed for 1 h at room temperature. Beads were washed twice with 2 M lactic acid/50% ACN and once with 0.1% TFA in 50% ACN. Phosphopeptides were eluted twice with 150 mL of 50 mM HK2PO4, pH 10. The eluates were acidified with 40 mL of 20% formic acid, and were subjected to C18 StageTip desalting.

After the labeling with TMT reagents (TMT 10-plex, Thermo), samples were mixed together and were separated with basic-pH reverse phase (bpHrp) HPLC fractionation as reported previously (Erickson et al., 2015). A total of 18 fractions were collected, which were then acidified with 10 mL of 20% formic acid and vacuum-dried. Each sample was re-dissolved in

5% formic acid, desalted via StageTip, dried via vacuum centrifugation, and reconstituted for LC−MS/MS analysis.

All mass spectra were acquired on an Orbitrap Fusion mass spectrometer (Thermo) coupled to an Easy-nLC 1000 ultrahigh pressure liquid chromatography (UHPLC) pump. Peptides were separated on an in-house packed C18 column with a gradient consisting of 6-27% (ACN) over 190 min at 300 nL/min. For all experiments, the instrument was operated under the data-dependent mode. MS1 spectra were collected using FT detection with a resolution of 120,000, with an automated gain control (AGC) target and max injection time of 400,000 and 50 ms, respectively. The 10 most intense ions were selected and were targeted for MS/MS analyses. Previously detected ions were excluded using the dynamic exclusion option of (60 second and ±10 ppm). The MS2 ions were isolated with a quadrupole mass filter which is set to bear an isolation window of 0.7 m/z. Ions were then fragmented using CID with a collision energy set at 35%. The automated gain control (AGC) target and max injection time were set to be 10,000 and 50 ms. FTMS3 spectra were acquired with 10 MS2 ions isolated using the synchronous-precursor-selection (SPS) option, and the HCD collision energy was set at 65%.

Mass spectra were searched against a composite database of the human IPI protein database (Version 3.60) and its reversed complement using the Sequest algorithm. Search parameters allowed for a static modification of 57.02146 Da, 229.16293 Da and 229.16293 Da for cysteine, lysine and N-termini, respectively. A dynamic modification of oxidation (15.99491 Da) and phosphorylation (79.96633 Da) was allowed on methionine and Ser/Thr/Tyr, respectively. Search results were filtered to include <1% matches to the reverse database by

the linear discriminator function using parameters including Xcorr, dCN, missed cleavage, charge state (exclude 1+ peptides), mass accuracy, all heavy or light Lys and Arg, peptide length and fraction of ions matched to MS/MS spectra (Huttlin et al., 2010). Peptide quantification was performed by setting a 0.003 m/z window around the theoretical m/z values of each reporter ion using the CoreQuant algorithm (Erickson et al., 2015). Reporter ion intensities were further adjusted by removing the interference from isotopic impurities (based on the information provided in the manufacturer specifications). Pearson correlation was used to calculate the correlation of adjusted ion intensities (global phosphoproteomic states) between cell lines. The non-variant, lower quartile of adjusted ion intensity values were excluded from the correlation analysis.

Small Molecule Cell Viability Assays

For dose response analyses, cells were first plated at a density of 1-2K/well in 96-well plates. Twenty-four hours after seeding, compounds solubilized in DMSO or DMSO alone (equal volume) were added to achieve the indicated final concentrations. Cell viability was measured 72 hours after compound exposure by CellTiter-Glo (Promega). Data were normalized using DMSO control treated cells in the same plates. Response curves were modeled using a nonlinear regression curve fit with a three-parameter dose response using GraphPad Prism 6 software. Area under the curve (AUC) calculations were performed using the trapezoid rule by connecting every adjacent point defining the curve with a straight line and summing the areas below those points using GraphPad Prism 6 software. Receiver

operator characteristics (ROC) area under the curve analysis was performed using GraphPad Prism 6 software. For ROC curve analysis vemurafenib or trametinib treated cells were dichotomized (half and half) into “sensitive” or “resistant” bins based on the rank of their AUC values. Compound II or BX795 treated cells were dichotomized based on the observed natural break of their LD50 values (i.e. Figures 4D and S4K). A375 resistant clones cells were seeded at a density of 4K/well in 96-well plates and exposed to serial dilutions of Trametinib or compound II. Cell survival was assayed by fixing and staining cells with 0.5% crystal violet (Sigma) in 4% formaldehyde after 72 hours. Survival was quantified by measuring the absorbance of the solubilized dye at an optical density of 595nm (Synergy H1M).

Caspase-Glo 3/7 Assays

Cells were plated at a density of 2K/well in 96-well plates. Twenty-four hours after seeding, compounds solubilized in DMSO or DMSO alone (equal volume) were added to achieve the indicated final concentrations. Apoptosis was measured 24 hours after compound exposure by Caspase-Glo 3/7 Assay (Promega). For TGFβ stimulation, cells were plated in 0.5% FBS and allowed to attach to the wells overnight. The next morning 10 ng/ml recombinant human TGFβ was added in serum free medium. Twenty-four hours later compound II solubilized in DMSO or DMSO alone (equal volume) was added to achieve the indicated final concentrations. Apoptosis was measured 24 hours after compound II exposure by Caspase-Glo 3/7 Assay (Promega). In experiments testing the effects of EZH2 inhibition in

conjunction with TGFβ stimulation, cells were pretreated with either GSK126 or EPZ-6438 24 hours before the TGFβ stimulation.

Metabolic Stability and Pharmacokinetics Studies

Compound II and BX795 levels for metabolic stability and pharmacokinetic studies were monitored by LC-MS/MS using an AB/Sciex (Applied Biosystems, Foster City, CA) 4000 Qtrap mass spectrometer coupled to a Shimadzu Prominence LC. Compound II was detected with the mass spectrometer in positive MRM (multiple reaction monitoring) mode by following the precursor to fragment ion transition 534.267 to 141.188. BX795 was also detected in positive MRM mode by following the precursor to fragment ion transition 592.095 to 254.122. An Agilent C18 XDB 5 micron packing column (50 X 4.6 mm) was used for chromatography for both compounds with the following conditions: Buffer A: dH20 + 0.1% formic acid, Buffer B: methanol + 0.1% formic acid, 0 - 1.5 min 3% B, 1.5 - 2.5 min gradient to 100% B, 2.5 - 3.5 min 100% B, 3.5 - 3.6 min gradient to 3% B, 3.6 – 4.5 min 3% B. N-benzylbenzamide (Sigma, St. Louis, MO) was used as an internal standard (IS, transition 212.1 to 91.1). For S9 studies, Compound II or BX795 (2 μM) was incubated in a 0.5 ml incubation volume with 0.5 mg (1 mg/ml) of murine CD-1 S9 (combined cytosol and microsome) fractions purchased from Celsis/In Vitro Technologies (Baltimore, MD) and Phase I (an NADPH regenerating system) cofactors (Sigma) for 0-240 min. Reactions were quenched by mixing the incubation mixture with an equal volume of methanol containing formic acid and the N-benzylbenzamide IS. The quenched mixture was vortexed for 15 sec,

incubated at room temperature for 10 min and spun for 5 min at 986 x g. Supernatants were then transferred to an Eppendorf tube and spun in a refrigerated microcentrifuge for 5 min at 16,100 x g. The second supernatant was transferred to an HPLC vial and analyzed by LC-MS/MS. Metabolic stability studies using both Phase I and Phase II (UDPGA and PAPS both from Sigma) cofactors were conducted similarly. Metabolism of 7-ethoxycoumarin was used to monitor S9 performance. Pharmacokinetic studies were performed by injecting 6-7 week old CD-1 female mice from Charles River Laboratories (Willmington, MA) with Compound II at 10 mg/kg IP formulated in 100% saline or BX795 also at 10 mg/kg formulated in 10% DMSO, 10% cremophor EL (Sigma) and 80% saline. Animals were sacrificed in groups of three, blood was obtained by cardiac puncture at each time point (0, 10, 30, 90, 180, 360, 960 and 1440 min post dose) using the anticoagulant ACD (acidified citrate dextrose) and plasma isolated by centrifugation. The ACD solution was made using 1.32g of sodium citrate, 0.48g of citric acid and 1.47g of dextrose dissolved in 100 ml of water. 100 µl of plasma was mixed with 200 µl of methanol containing 0.15% formic acid and 20 ng/ml N-benzylbenzamide IS. The samples were vortexed 15 sec, incubated at room temp for 10' and spun twice at 16,100 x g 4^0C in a refrigerated microcentrifuge. The amount of Compound II or BX795 present in plasma was quantified by LC-MS/MS to determine the rate of clearance from mouse blood. Standard curves were generated using blank plasma spiked with known concentrations of Compound II or BX795 and processed as described above. The concentrations of Compound II or BX795 in each time-point sample were quantified using Analyst 1.6.1. A value of 3-fold above the signal obtained from blank plasma was designated the limit of detection (LOD). The limit of quantitation (LOQ) was defined as the lowest concentration at which back

calculation yielded a concentration within 20% of theoretical. The LOQ for plasma was 1 ng/ml for Compound II and 5 ng/ml for BX795. Pharmacokinetic parameters were calculated using the noncompartmental analysis tool of WinNonLin (Pharsight, Sunnyvale, CA). Compound II levels in tumors were determined in a similar fashion. Tumor-bearing NOD/SCID IL2Rγnull (NSG) mice were euthanized 2 hr after compound administration. Tumors were removed, rinsed briefly with PBS, patted dry, weighed and snap frozen in liquid nitrogen. Tumors were homogenized in a 3-fold volume of dH20 in ml relative to their weight in g. 100 µl of tumor homogenate was processed as described above for plasma, and compound II levels in tumor determined using a standard curve prepared in untreated tumor matrix.

Mouse Xenograft Studies

NOD/SCID IL2Rg^{null} (NSG) mice were purchased from UTSWMC shared resource. Animals were cared for according to guidelines set forth by the American Association for Accreditation of Laboratory Animal Care and the U.S. Public Health Service policy on Human Care and Use of Laboratory Animals. All mouse studies were approved and supervised by the UT Southwestern Institutional Animal Care and Use Committee. All animals used were between 8–12 weeks of age at the time of injection. For all animal experiments, cells were trypsinized, washed, and resuspended in PBS prior to injection. 5 x 10^5 LOXIMVI cells or 7.5 x 10^5 A2058 cells/flank were injected in 100 ml subcutaneously into both flanks. 1 x 10^6 CHL1 cells were injected in 25% matrigel in 100 ml into right

flanks. Compound II (100 mg/kg) or saline were delivered IP daily after detection of palpable tumors (5 days post inoculation for LOXIMVI and 7 days post inoculation for A2058 and CHL1). Tumor volume was monitored throughout the experiment with digital calipers and volume calculated using the formula: D x d2 x 0.52. Mice were euthanized when the largest diameter of at least one tumor reached 20mm. Compound II or vehicle was IP delivered ~2 hr before collecting the tumors.

Feature-based Cluster Analysis

Clustering analysis was performed with the affinity propagation clustering (APC) algorithm using the 'apcluster' package in R. APC was selected as it is a deterministic clustering method which identifies the number of clusters, and cluster 'exemplars' (i.e. the cluster centroid or the data point that is the best representative of all the other data points within that cluster) entirely from the data (Frey and Dueck, 2007), giving it an advantage over non-deterministic methods subject to a biased randomized initialization step. APC performs clustering by passing messages between the data points. It takes as input a square matrix representing pairwise similarity measures between all data points. The algorithm views each data point as a node in a network and is initialized by connecting all the nodes together where edges between nodes are proportional to Pearson correlations. The algorithm then iteratively transmits messages along the edges, pruning edges with each iteration, until a set of clusters and exemplars emerges. Two real valued messages are passed between nodes. The

'responsibility' message computes how well suited it is for point *i* to choose point *k* as an exemplar, given all the other candidate exemplars, *k'*, and is updated by:

$$r(i,k) \leftarrow s(i,k) - \max_{k' s.t. k' \neq k}\{a(i,k') + s(i,k')\}$$

The availability message, a(i,k), computes how appropriate it is for point *i* to select point *k* as an exemplar, taking into account all the other points for which *k* is an exemplar, *i'*, and is given by:

$$a(i,k) \leftarrow \min\left\{0, r(k,k) + \sum_{i' s.t.\ i' \notin (i,k)} \max(0, r(i',k))\right\}$$

In the above equation, *a(i,k)* is set to the self responsibility, *r(k,k),* plus the sum of the positive responsibilities candidate *k* receives from other points. The entire sum is thresholded at 0, and a negative availability indicates that it is inappropriate for point *i* to choose point *k* as an exemplar and the tie is severed. The self-availability, *a(k,k)*, reflects the accumulated evidence that point *k* is an exemplar and is updated with the following rule, which reflects the evidence that *k* is an exemplar based on the positive responsibilities sent to *k* from all points, and is updated by:

$$a(k,k) \leftarrow \sum_{i' s.t.\ i' \notin (i,k)} \max(0, r(i',k))$$

In the first iteration, all points are considered equally likely to be candidate exemplars, and *a(i,k)* is set to 0 and *s(i,k)* is set to the input similarity measure between points *i* and *k*. The above rules are then iteratively updated until a clear, stable set of clusters and exemplars emerges. In our implementation, we first employed the algorithm to identify an initial set of

exemplars and clusters from the data matrix. The exemplars were then clustered together and this procedure was repeated until no more clusters emerged to identify a hierarchical structure of clusters. The 19 Melanoma cell lines were clustered according to their relative viability vectors across 60 siRNAs (Figure 1I). To cluster cell lines by similar expression profiles, we first reduced the panel of genes to represent those that were expressed at a $\log_2$ normalized expression value of 6 in at least one cell line and those genes that were present in the top 20% of the most highly variant genes, resulting in a panel of 2522 genes. Networks were drawn with Cytoscape (Shannon et al., 2003).

Elastic Net Analysis

We employed a penalized linear regression model (elastic net) to select features that, either alone or in combination, can predict an siRNA viability response vector (Zou and Hastie, 2005).

Candidate predictive features were selected from measures of gene expression (Illumina Bead arrays) across 19 cell lines. Measures were quantile normalized and background corrected with the MBCB package in R and duplicated measurements for the same gene were compressed into a single value by taking the median value between the duplicates. Genes were included as candidate predictive features if they were expressed at a minimum $\log_2$ expression value of 6 in at least one cell line and if there was at least a 2 fold difference

between minimal and maximal gene expression across the cell line panel; resulting in a total of 12133 candidate genes.

Let $X \in \mathbb{R}^{n \times p}$ be the matrix of predictive features where n is the number of cell lines included in the training dataset and p is the number of features, and let $y \in \mathbb{R}^{n}$ be the vector of binary sensitivity values for the same cell line panel. Columns of the predictive features matrix and y were normalized to have a mean of zero and a standard deviation of 1. The elastic net attempts to find which weighted linear combination of the columns of the predictive features matrix can best approximate y, or it solves the following equation for w:

$$argmin_{w} \{\|y - Xw\|_2^2\}$$

The elastic net solves the above by enforcing a penalty to the solution that makes the solution both unique and sparse so that only the features that best approximate *y* are left with non-zero weight values. It does this by combining L1-norm and L2-norm regularization parameters so that the elastic net formulation to the above problem is given by:

$$argmin_{w} \{\|y - Xw\|_2^2 + \lambda(\alpha\|w\|_2^2 + (1-\alpha)\|w\|_1)\}$$

where λ, α, are two adjustable parameters such that λ controls the degree of the overall penalty and α controls the degree to which the L1 norm and L2 norm constraints are applied so that when α=0, only the L1 penalty is applied and when α=1, only the L2 penalty is applied. In order to determine the optimal values of alpha and lambda for the model, we carried out 100 iterations of 5-fold cross-validation where, for each iteration, cell lines were randomly re-sampled into different groups. The values of alpha and lambda were chosen to

be those that resulted in the minimum mean squared error for each fold. Features were then chosen to be those with the highest weights that were selected as features in at least 80% of the cross-validation permutations.

Predicting Sensitivities in Test Sets

Weights were calculated for each of the features selected from the elastic net using the original 19 cell lines as a training set. Normalized predictive sensitivity values for untested samples (cell lines or tumor tissue) were then calculated for each of the samples in the test set with the following formula:

$$s_j = \sum_{i=1}^{n=3} w_i x_{ij}$$

where w_i is the weight determined from the elastic net for feature i, and x_{ij} is the normalized expression value of feature i in line j. The range of s_i values predicts the degree of sensitivity where a high value of s_i predicts resistant and a low value of s_i predicts sensitive. Melanoma discovery set: The described 5-gene SOX10 Elastic Net gene signature was used to generate prediction scores in 19 melanoma cells (Figure 12A). mRNA expression data was from Illumina HT-12 V4 Beadchip microarrays. CCLE: The same 5-gene SOX10 Elastic Net gene signature was used to predict chemical and siRNA sensitivities in 61 Melanoma cells from the CCLE panel (data available at www.broadinstutite.com/ccle). CCLE mRNA expression data was from Affymetrix HGU 133A Plus 2.0 microarrays. Garnett et al.: Raw HTU 133A affymetrix expression data (.CEL files) from the McDermott/Benes GDSC dataset was

downloaded using ArrayExpress accession number E-MTAB-783. Data was background corrected with an RMA function and quantile normalized using the packages gcrma and affy in R. A 4-gene signature (FAM69B was not assayed in the array) was used to predict SOX10 sensitivity for 35 melanoma cell lines. TCGA cutaneous melanoma: TCGA RNASeq measures of RPKM gene expression were acquired for 80 Uveal Melanoma (UVM) and for 333 Stage III Skin Cutaneous Melanoma (SKCM) tumor samples with manually curated high confidence clinical data using the cgdsr package in R. A 5-gene expression signature was used to predict tumor sensitivity to targeted therapies or TBK1i. Rizos et al.: Normalized and background corrected data from Rizos et al. (Rizos et al., 2014) was downloaded using accession number GSE50509, representing dabrafenib and/or vemurafenib treated and untreated metastatic melanoma tumor samples from a total of 21 patients. Some tumors were assayed at multiple sites, resulting in 21 untreated samples and 33 compound treated tumor samples assayed with Illumina HT-12 V4 Bead Chip arrays. A 4-gene prediction expression signature (FAM69B was found to have poor dynamic range in this data set and was removed from the signature) was used to predict targeted therapy sensitivity for treated and untreated tumor samples separately. Long dataset (Figure 12L): Normalized and background corrected expression data was used to predict the targeted therapy sensitivity using 5-gene biomarker from melanoma tumor samples isolated from patients treated with either BRAF(V600) therapy (dabrafenib/vemurafenib) or BRAF(V600) and MEKi combination therapy (dabrafenib and trametinib). Hugo et al.: RNASeq-derived FPKM values were used to predict the targeted therapy sensitivity of 17 pre-treatment tumors resected from patients undergoing dabrafenib, vemurafenib or dabrafenib/trametinib therapy. Jonsson et al.: Normalized and

background corrected expression data assayed with Affymetrix HGU 133 Plus 2.0 arrays from Jonsson et al. (Jonsson et al., 2010) was downloaded using GEO accession number GSE19234. A 5-gene expression signature was used to predict SOX10 sensitivity in 31 Stage IV metastatic melanoma tumor samples. Melanoma PDX: Mouse Xenograft derived expression data assayed with Illumina HT-12 V4 Beadchip microarrays was acquired from Sean Morrison (personal communication), representing a total of 81 xenografts from 32 patients. A 5-gene expression signature was used to predict SOX10 sensitivity.

Survival Analysis

Differences in survival were calculated for the predicted targeted therapy sensitive and resistant classes represented by tails of the distributions. Cutoffs, defining the tails of the distributions, were specified by the inflection points of the predicted scores for each dataset. They are as follows: TCGA UVM : +/- .1; TCGA SKCM: +/- .05; GSE19234: +/- .05; GSE50509: +/- .05; Morrison PDX: +/- .1. Kaplan-Meier method was then used to estimate overall survival. Log-rank test was used to assess the statistical significance between the predicted targeted therapy sensitive and resistant groups. In addition log-rank analysis was used to generate hazard ratios (HRs). All survival analyses were done using GraphPad Prism 6 software.

KS Test

The combined expression distributions of 10 ISG genes (IFI44, IFIT3, STAT1, STAT2, RTP4, DDX58, IFIH1, IRF7, IRF1, IRF3) (West et al., 2015) in TCGA SKCM-low lymphocyte samples with prediction scores <-0.05 and in TCGA SKCM-low lymphocyte samples with prediction scores >0.05 was compared. In addition, the combined expression of this set of genes in Compound II sensitive melanoma cell lines (LOXIMVI, LM20, C8161, and WM3211) was compared to expression in Compound II resistant melanoma cell lines (SKMEL5, LM38, MNT1, and YUMAC). Significance of separation between the empirical cumulative distributions in each comparison was calculated with a KS test using the KS stats package in R.

Ranked KS Test:

To calculate pathways that were down regulated relative to the background distribution on an individual cell line basis, we used a modification of a Kolmogorov Smirnov test. Illumina-derived gene expression ratios from SOX10 siRNA- versus control siRNA-treated MNT1 cells were log2 transformed and then converted to a ranked integer list. To determine the degree to which the values in a set are located towards the top of a ranked list, and thus upregulated relative to background, the following equation was used:

$$u = max_{i=1}^{t}\left[\frac{j}{t} - \frac{V(j)}{n}\right]$$

and to determine the degree to which a set is downregulated relative to background, the following equation was used:

$$u = max_{i=1}^{t} \left| \frac{V(j)}{n} - \frac{(j-1)}{t} \right|$$

where v(j) is the position of each gene in the gene set in the ordered list of genes, t is the total number of genes in the gene set, and n is the total number of genes assayed in the array.

To determine a p-value, 5000 permutations of randomized sorting of genes of genes of the same set size was performed, and u_{random} was calculated. The resulting p-value was determined to be:

$$p = \frac{\#\ instances\ u_{random} > u}{\#\ total\ permutation}$$

This modification is distinct from a standard KS test in several ways: First, when comparing a large distribution to a small distribution in a standard KS test, the NULL hypothesis is biased towards being rejected, and thus introduce false positives. Second, a ranked KS test allows for the preferential ranking of sets that are separated from the background at the tails of the distribution, which was desirable for the analysis in this study.

Signal to Noise Ratios

To identify compounds that segregate with predicted SOX10 sensitivity status in the

McDermott/Benes GDSC dataset, we first determined the size and density of the available melanoma cell line/ chemical compound dose response matrix by two-way clustering of a binary presence call matrix. We next calculated an S2N for each compound using the IC50 values for the top 4 highest predicted SOX10 sensitive melanoma tumor cell lines versus the top 4 highest predicted SOX10 resistant lines. A signal to noise ratio between two classes, A and B, was defined as:

$$S2N = \frac{\mu(A) - \mu(B)}{\sigma(A) + \sigma(B)}$$

Compounds were ranked on absolute values of the S2N values.

BIBLIOGRAPHY

Abel, E. V., Basile, K. J., Kugel, C. H., 3rd, Witkiewicz, A. K., Le, K., Amaravadi, R. K., Karakousis, G. C., Xu, X., Xu, W., Schuchter, L. M.*, et al.* (2013). Melanoma adapts to RAF/MEK inhibitors through FOXD3-mediated upregulation of ERBB3. J Clin Invest *123*, 2155-2168.

Ahronian, L. G., Sennott, E. M., Van Allen, E. M., Wagle, N., Kwak, E. L., Faris, J. E., Godfrey, J. T., Nishimura, K., Lynch, K. D., Mermel, C. H.*, et al.* (2015). Clinical Acquired Resistance to RAF Inhibitor Combinations in BRAF-Mutant Colorectal Cancer through MAPK Pathway Alterations. Cancer Discov *5*, 358-367.

Alexandrov, L. B., Nik-Zainal, S., Wedge, D. C., Aparicio, S. A., Behjati, S., Biankin, A. V., Bignell, G. R., Bolli, N., Borg, A., Borresen-Dale, A. L.*, et al.* (2013). Signatures of mutational processes in human cancer. Nature *500*, 415-421.

Bailey, T. L., Williams, N., Misleh, C., and Li, W. W. (2006). MEME: discovering and analyzing DNA and protein sequence motifs. Nucleic Acids Res *34*, W369-373.

Bain, J., Plater, L., Elliott, M., Shpiro, N., Hastie, C. J., McLauchlan, H., Klevernic, I., Arthur, J. S., Alessi, D. R., and Cohen, P. (2007). The selectivity of protein kinase inhibitors: a further update. Biochem J *408*, 297-315.

Barretina, J., Caponigro, G., Stransky, N., Venkatesan, K., Margolin, A. A., Kim, S., Wilson, C. J., Lehar, J., Kryukov, G. V., Sonkin, D.*, et al.* (2012). The Cancer Cell Line Encyclopedia enables predictive modelling of anticancer drug sensitivity. Nature *483*, 603-607.

Benz, R., and McLaughlin, S. (1983). The molecular mechanism of action of the proton ionophore FCCP (carbonylcyanide p-trifluoromethoxyphenylhydrazone). Biophys J *41*, 381-398.

Beuret, L., Flori, E., Denoyelle, C., Bille, K., Busca, R., Picardo, M., Bertolotto, C., and Ballotti, R. (2007). Up-regulation of MET expression by alpha-melanocyte-stimulating hormone and MITF allows hepatocyte growth factor to protect melanocytes and melanoma cells from apoptosis. J Biol Chem *282*, 14140-14147.

Bhat, K. P., Salazar, K. L., Balasubramaniyan, V., Wani, K., Heathcock, L., Hollingsworth, F., James, J. D., Gumin, J., Diefes, K. L., Kim, S. H.*, et al.* (2011). The transcriptional coactivator TAZ regulates mesenchymal differentiation in malignant glioma. Genes Dev *25*, 2594-2609.

Bianco, S., Lanvin, O., Tribollet, V., Macari, C., North, S., and Vanacker, J. M. (2009). Modulating estrogen receptor-related receptor-alpha activity inhibits cell proliferation. J Biol Chem *284*, 23286-23292.

Bicego, M., Morassutto, S., Hernandez, V. H., Morgutti, M., Mammano, F., D'Andrea, P., and Bruzzone, R. (2006). Selective defects in channel permeability associated with Cx32 mutations causing X-linked Charcot-Marie-Tooth disease. Neurobiol Dis *21*, 607-617.

Bombail, V., Gibson, D. A., Collins, F., MacPherson, S., Critchley, H. O., and Saunders, P. T. (2010). A Role for the orphan nuclear receptor estrogen-related receptor alpha in endometrial stromal cell decidualization and expression of genes implicated in energy metabolism. J Clin Endocrinol Metab *95*, E224-228.

Bondurand, N., Girard, M., Pingault, V., Lemort, N., Dubourg, O., and Goossens, M. (2001). Human Connexin 32, a gap junction protein altered in the X-linked form of Charcot-Marie-Tooth disease, is directly regulated by the transcription factor SOX10. Hum Mol Genet *10*, 2783-2795.

Bonnelye, E., Reboul, P., Duval, N., Cardelli, M., and Aubin, J. E. (2011). Estrogen receptor-related receptor alpha regulation by interleukin-1beta in prostaglandin E(2)- and cAMP-dependent pathways in osteoarthritic chondrocytes. Arthritis Rheum *63*, 2374-2384.

Brugarolas, J., Lei, K., Hurley, R. L., Manning, B. D., Reiling, J. H., Hafen, E., Witters, L. A., Ellisen, L. W., and Kaelin, W. G., Jr. (2004). Regulation of mTOR function in response to hypoxia by REDD1 and the TSC1/TSC2 tumor suppressor complex. Genes Dev *18*, 2893-2904.

Burke, J. R., Pattoli, M. A., Gregor, K. R., Brassil, P. J., MacMaster, J. F., McIntyre, K. W., Yang, X., Iotzova, V. S., Clarke, W., Strnad, J.*, et al.* (2003). BMS-345541 is a highly selective inhibitor of I kappa B kinase that binds at an allosteric site of the enzyme and blocks NF-kappa B-dependent transcription in mice. J Biol Chem *278*, 1450-1456.

Buss, H., Dorrie, A., Schmitz, M. L., Hoffmann, E., Resch, K., and Kracht, M. (2004). Constitutive and interleukin-1-inducible phosphorylation of p65 NF-{kappa}B at serine 536 is mediated by multiple protein kinases including I{kappa}B kinase (IKK)-{alpha}, IKK{beta}, IKK{epsilon}, TRAF family member-associated (TANK)-binding kinase 1 (TBK1), and an unknown kinase and couples p65 to TATA-binding protein-associated factor II31-mediated interleukin-8 transcription. J Biol Chem *279*, 55633-55643.

Cancer Genome Atlas, N. (2015). Genomic Classification of Cutaneous Melanoma. Cell *161*, 1681-1696.

Cantelli, G., Orgaz, J. L., Rodriguez-Hernandez, I., Karagiannis, P., Maiques, O., Matias-Guiu, X., Nestle, F. O., Marti, R. M., Karagiannis, S. N., and Sanz-Moreno, V. (2015). TGF-beta-Induced Transcription Sustains Amoeboid Melanoma Migration and Dissemination. Curr Biol *25*, 2899-2914.

Chambers, R. C., Leoni, P., Kaminski, N., Laurent, G. J., and Heller, R. A. (2003). Global expression profiling of fibroblast responses to transforming growth factor-beta1 reveals the induction of inhibitor of differentiation-1 and provides evidence of smooth muscle cell phenotypic switching. Am J Pathol *162*, 533-546.

Chang, C. Y., Kazmin, D., Jasper, J. S., Kunder, R., Zuercher, W. J., and McDonnell, D. P. (2011). The metabolic regulator ERRalpha, a downstream target of HER2/IGF-1R, as a therapeutic target in breast cancer. Cancer Cell *20*, 500-510.

Chapman, P. B., Hauschild, A., Robert, C., Haanen, J. B., Ascierto, P., Larkin, J., Dummer, R., Garbe, C., Testori, A., Maio, M.*, et al.* (2011). Improved survival with vemurafenib in melanoma with BRAF V600E mutation. N Engl J Med *364*, 2507-2516.

Chen, L., and Wong, C. (2009). Estrogen-related receptor alpha inverse agonist enhances basal glucose uptake in myotubes through reactive oxygen species. Biol Pharm Bull *32*, 1199-1203.
Cheng, T., Sudderth, J., Yang, C., Mullen, A. R., Jin, E. S., Mates, J. M., and DeBerardinis, R. J. (2011). Pyruvate carboxylase is required for glutamine-independent growth of tumor cells. Proc Natl Acad Sci U S A *108*, 8674-8679.
Clark, K., Peggie, M., Plater, L., Sorcek, R. J., Young, E. R., Madwed, J. B., Hough, J., McIver, E. G., and Cohen, P. (2011). Novel cross-talk within the IKK family controls innate immunity. Biochem J *434*, 93-104.
Cooper, R., Singh, R., and Clough, J. (2006). Spiro-2, 4-pyrimidinediamine compounds and their uses. In, (US Patent Office).
Cooper, Z. A., Juneja, V. R., Sage, P. T., Frederick, D. T., Piris, A., Mitra, D., Lo, J. A., Hodi, F. S., Freeman, G. J., Bosenberg, M. W.*, et al.* (2014). Response to BRAF inhibition in melanoma is enhanced when combined with immune checkpoint blockade. Cancer Immunol Res *2*, 643-654.
Couzens, A. L., Knight, J. D., Kean, M. J., Teo, G., Weiss, A., Dunham, W. H., Lin, Z. Y., Bagshaw, R. D., Sicheri, F., Pawson, T.*, et al.* (2013). Protein interaction network of the mammalian Hippo pathway reveals mechanisms of kinase-phosphatase interactions. Sci Signal *6*, rs15.
Davies, H., Bignell, G. R., Cox, C., Stephens, P., Edkins, S., Clegg, S., Teague, J., Woffendin, H., Garnett, M. J., Bottomley, W.*, et al.* (2002). Mutations of the BRAF gene in human cancer. Nature *417*, 949-954.
Davies, S. P., Sim, A. T., and Hardie, D. G. (1990). Location and function of three sites phosphorylated on rat acetyl-CoA carboxylase by the AMP-activated protein kinase. Eur J Biochem *187*, 183-190.
Dwyer, M. A., Joseph, J. D., Wade, H. E., Eaton, M. L., Kunder, R. S., Kazmin, D., Chang, C. Y., and McDonnell, D. P. (2010). WNT11 expression is induced by estrogen-related receptor alpha and beta-catenin and acts in an autocrine manner to increase cancer cell migration. Cancer Res *70*, 9298-9308.
Emery, C. M., Vijayendran, K. G., Zipser, M. C., Sawyer, A. M., Niu, L., Kim, J. J., Hatton, C., Chopra, R., Oberholzer, P. A., Karpova, M. B.*, et al.* (2009). MEK1 mutations confer resistance to MEK and B-RAF inhibition. Proc Natl Acad Sci U S A *106*, 20411-20416.
Erickson, B. K., Jedrychowski, M. P., McAlister, G. C., Everley, R. A., Kunz, R., and Gygi, S. P. (2015). Evaluating multiplexed quantitative phosphopeptide analysis on a hybrid quadrupole mass filter/linear ion trap/orbitrap mass spectrometer. Anal Chem *87*, 1241-1249.
Eskiocak, B., Ali, A., and White, M. A. (2014). The estrogen-related receptor alpha inverse agonist XCT 790 is a nanomolar mitochondrial uncoupler. Biochemistry *53*, 4839-4846.
Feldman, R. I., Wu, J. M., Polokoff, M. A., Kochanny, M. J., Dinter, H., Zhu, D., Biroc, S. L., Alicke, B., Bryant, J., Yuan, S.*, et al.* (2005). Novel small molecule inhibitors of 3-phosphoinositide-dependent kinase-1. J Biol Chem *280*, 19867-19874.

Fiori, J. L., Sanghvi, M., O'Connell, M. P., Krzysik-Walker, S. M., Moaddel, R., and Bernier, M. (2011). The cannabinoid receptor inverse agonist AM251 regulates the expression of the EGF receptor and its ligands via destabilization of oestrogen-related receptor alpha protein. Br J Pharmacol *164*, 1026-1040.
Fisher, K. W., Das, B., Kortum, R. L., Chaika, O. V., and Lewis, R. E. (2011). Kinase suppressor of ras 1 (KSR1) regulates PGC1alpha and estrogen-related receptor alpha to promote oncogenic Ras-dependent anchorage-independent growth. Mol Cell Biol *31*, 2453-2461.
Fitzgerald, K. A., McWhirter, S. M., Faia, K. L., Rowe, D. C., Latz, E., Golenbock, D. T., Coyle, A. J., Liao, S. M., and Maniatis, T. (2003). IKKepsilon and TBK1 are essential components of the IRF3 signaling pathway. Nat Immunol *4*, 491-496.
Flaherty, K. T., Hodi, F. S., and Fisher, D. E. (2012a). From genes to drugs: targeted strategies for melanoma. Nat Rev Cancer *12*, 349-361.
Flaherty, K. T., Puzanov, I., Kim, K. B., Ribas, A., McArthur, G. A., Sosman, J. A., O'Dwyer, P. J., Lee, R. J., Grippo, J. F., Nolop, K., and Chapman, P. B. (2010). Inhibition of mutated, activated BRAF in metastatic melanoma. N Engl J Med *363*, 809-819.
Flaherty, K. T., Robert, C., Hersey, P., Nathan, P., Garbe, C., Milhem, M., Demidov, L. V., Hassel, J. C., Rutkowski, P., Mohr, P.*, et al.* (2012b). Improved survival with MEK inhibition in BRAF-mutated melanoma. N Engl J Med *367*, 107-114.
Frederick, D. T., Piris, A., Cogdill, A. P., Cooper, Z. A., Lezcano, C., Ferrone, C. R., Mitra, D., Boni, A., Newton, L. P., Liu, C.*, et al.* (2013). BRAF inhibition is associated with enhanced melanoma antigen expression and a more favorable tumor microenvironment in patients with metastatic melanoma. Clin Cancer Res *19*, 1225-1231.
Frey, B. J., and Dueck, D. (2007). Clustering by passing messages between data points. Science *315*, 972-976.
Gacias, M., Perez-Marti, A., Pujol-Vidal, M., Marrero, P. F., Haro, D., and Relat, J. (2012). PGC-1beta regulates mouse carnitine-acylcarnitine translocase through estrogen-related receptor alpha. Biochem Biophys Res Commun *423*, 838-843.
Ganesan, A. K., Ho, H., Bodemann, B., Petersen, S., Aruri, J., Koshy, S., Richardson, Z., Le, L. Q., Krasieva, T., Roth, M. G.*, et al.* (2008). Genome-wide siRNA-based functional genomics of pigmentation identifies novel genes and pathways that impact melanogenesis in human cells. PLoS Genet *4*, e1000298.
Garnett, M. J., Edelman, E. J., Heidorn, S. J., Greenman, C. D., Dastur, A., Lau, K. W., Greninger, P., Thompson, I. R., Luo, X., Soares, J.*, et al.* (2012). Systematic identification of genomic markers of drug sensitivity in cancer cells. Nature *483*, 570-575.
Garraway, L. A., Widlund, H. R., Rubin, M. A., Getz, G., Berger, A. J., Ramaswamy, S., Beroukhim, R., Milner, D. A., Granter, S. R., Du, J.*, et al.* (2005). Integrative genomic analyses identify MITF as a lineage survival oncogene amplified in malignant melanoma. Nature *436*, 117-122.
Girotti, M. R., Pedersen, M., Sanchez-Laorden, B., Viros, A., Turajlic, S., Niculescu-Duvaz, D., Zambon, A., Sinclair, J., Hayes, A., Gore, M.*, et al.* (2013). Inhibiting EGF receptor or SRC family kinase signaling overcomes BRAF inhibitor resistance in melanoma. Cancer Discov *3*, 158-167.

Gopal, Y. N., Rizos, H., Chen, G., Deng, W., Frederick, D. T., Cooper, Z. A., Scolyer, R. A., Pupo, G., Komurov, K., Sehgal, V.*, et al.* (2014). Inhibition of mTORC1/2 overcomes resistance to MAPK pathway inhibitors mediated by PGC1alpha and oxidative phosphorylation in melanoma. Cancer Res *74*, 7037-7047.

Gupta, S., Stamatoyannopoulos, J. A., Bailey, T. L., and Noble, W. S. (2007). Quantifying similarity between motifs. Genome Biol *8*, R24.

Gwinn, D. M., Shackelford, D. B., Egan, D. F., Mihaylova, M. M., Mery, A., Vasquez, D. S., Turk, B. E., and Shaw, R. J. (2008). AMPK phosphorylation of raptor mediates a metabolic checkpoint. Mol Cell *30*, 214-226.

Hamid, O., Robert, C., Daud, A., Hodi, F. S., Hwu, W. J., Kefford, R., Wolchok, J. D., Hersey, P., Joseph, R. W., Weber, J. S.*, et al.* (2013). Safety and tumor responses with lambrolizumab (anti-PD-1) in melanoma. N Engl J Med *369*, 134-144.

Hao, Y., Chun, A., Cheung, K., Rashidi, B., and Yang, X. (2008). Tumor suppressor LATS1 is a negative regulator of oncogene YAP. J Biol Chem *283*, 5496-5509.

Heinz, S., Benner, C., Spann, N., Bertolino, E., Lin, Y. C., Laslo, P., Cheng, J. X., Murre, C., Singh, H., and Glass, C. K. (2010). Simple combinations of lineage-determining transcription factors prime cis-regulatory elements required for macrophage and B cell identities. Mol Cell *38*, 576-589.

Hirai, H., Sootome, H., Nakatsuru, Y., Miyama, K., Taguchi, S., Tsujioka, K., Ueno, Y., Hatch, H., Majumder, P. K., Pan, B. S., and Kotani, H. (2010). MK-2206, an allosteric Akt inhibitor, enhances antitumor efficacy by standard chemotherapeutic agents or molecular targeted drugs in vitro and in vivo. Mol Cancer Ther *9*, 1956-1967.

Hodi, F. S., O'Day, S. J., McDermott, D. F., Weber, R. W., Sosman, J. A., Haanen, J. B., Gonzalez, R., Robert, C., Schadendorf, D., Hassel, J. C.*, et al.* (2010). Improved survival with ipilimumab in patients with metastatic melanoma. N Engl J Med *363*, 711-723.

Hoek, K., Rimm, D. L., Williams, K. R., Zhao, H., Ariyan, S., Lin, A., Kluger, H. M., Berger, A. J., Cheng, E., Trombetta, E. S.*, et al.* (2004). Expression profiling reveals novel pathways in the transformation of melanocytes to melanomas. Cancer Res *64*, 5270-5282.

Hoek, K. S., Schlegel, N. C., Eichhoff, O. M., Widmer, D. S., Praetorius, C., Einarsson, S. O., Valgeirsdottir, S., Bergsteinsdottir, K., Schepsky, A., Dummer, R., and Steingrimsson, E. (2008). Novel MITF targets identified using a two-step DNA microarray strategy. Pigment Cell Melanoma Res *21*, 665-676.

Hong, M. G., Reynolds, C. A., Feldman, A. L., Kallin, M., Lambert, J. C., Amouyel, P., Ingelsson, E., Pedersen, N. L., and Prince, J. A. (2012). Genome-wide and gene-based association implicates FRMD6 in Alzheimer disease. Hum Mutat *33*, 521-529.

Hsu, S., Kim, M., Hernandez, L., Grajales, V., Noonan, A., Anver, M., Davidson, B., and Annunziata, C. M. (2012). IKK-epsilon coordinates invasion and metastasis of ovarian cancer. Cancer Res *72*, 5494-5504.

Hua, S., Kittler, R., and White, K. P. (2009). Genomic antagonism between retinoic acid and estrogen signaling in breast cancer. Cell *137*, 1259-1271.

Huang, J., Wu, S., Barrera, J., Matthews, K., and Pan, D. (2005). The Hippo signaling pathway coordinately regulates cell proliferation and apoptosis by inactivating Yorkie, the Drosophila Homolog of YAP. Cell *122*, 421-434.

Huang, Y. H., Zhu, C., Kondo, Y., Anderson, A. C., Gandhi, A., Russell, A., Dougan, S. K., Petersen, B. S., Melum, E., Pertel, T.*, et al.* (2015). CEACAM1 regulates TIM-3-mediated tolerance and exhaustion. Nature *517*, 386-390.
Huber, W. E., Price, E. R., Widlund, H. R., Du, J., Davis, I. J., Wegner, M., and Fisher, D. E. (2003). A tissue-restricted cAMP transcriptional response: SOX10 modulates alpha-melanocyte-stimulating hormone-triggered expression of microphthalmia-associated transcription factor in melanocytes. J Biol Chem *278*, 45224-45230.
Hugo, W., Shi, H., Sun, L., Piva, M., Song, C., Kong, X., Moriceau, G., Hong, A., Dahlman, K. B., Johnson, D. B.*, et al.* (2015). Non-genomic and Immune Evolution of Melanoma Acquiring MAPKi Resistance. Cell *162*, 1271-1285.
Huss, J. M., Imahashi, K., Dufour, C. R., Weinheimer, C. J., Courtois, M., Kovacs, A., Giguere, V., Murphy, E., and Kelly, D. P. (2007). The nuclear receptor ERRalpha is required for the bioenergetic and functional adaptation to cardiac pressure overload. Cell Metab *6*, 25-37.
Huss, J. M., Kopp, R. P., and Kelly, D. P. (2002). Peroxisome proliferator-activated receptor coactivator-1alpha (PGC-1alpha) coactivates the cardiac-enriched nuclear receptors estrogen-related receptor-alpha and -gamma. Identification of novel leucine-rich interaction motif within PGC-1alpha. J Biol Chem *277*, 40265-40274.
Huttlin, E. L., Jedrychowski, M. P., Elias, J. E., Goswami, T., Rad, R., Beausoleil, S. A., Villen, J., Haas, W., Sowa, M. E., and Gygi, S. P. (2010). A tissue-specific atlas of mouse protein phosphorylation and expression. Cell *143*, 1174-1189.
Jain, P., Polliack, A., and Ravandi, F. (2015). Novel therapeutic options for relapsed hairy cell leukemia. Leuk Lymphoma, 1-9.
Johannessen, C. M., Boehm, J. S., Kim, S. Y., Thomas, S. R., Wardwell, L., Johnson, L. A., Emery, C. M., Stransky, N., Cogdill, A. P., Barretina, J.*, et al.* (2010). COT drives resistance to RAF inhibition through MAP kinase pathway reactivation. Nature *468*, 968-972.
Jonsson, G., Busch, C., Knappskog, S., Geisler, J., Miletic, H., Ringner, M., Lillehaug, J. R., Borg, A., and Lonning, P. E. (2010). Gene expression profiling-based identification of molecular subtypes in stage IV melanomas with different clinical outcome. Clin Cancer Res *16*, 3356-3367.
Kamei, Y., Ohizumi, H., Fujitani, Y., Nemoto, T., Tanaka, T., Takahashi, N., Kawada, T., Miyoshi, M., Ezaki, O., and Kakizuka, A. (2003). PPARgamma coactivator 1beta/ERR ligand 1 is an ERR protein ligand, whose expression induces a high-energy expenditure and antagonizes obesity. Proc Natl Acad Sci U S A *100*, 12378-12383.
Kasianowicz, J., Benz, R., and McLaughlin, S. (1984). The kinetic mechanism by which CCCP (carbonyl cyanide m-chlorophenylhydrazone) transports protons across membranes. J Membr Biol *82*, 179-190.
Kim, H. S., Mendiratta, S., Kim, J., Pecot, C. V., Larsen, J. E., Zubovych, I., Seo, B. Y., Kim, J., Eskiocak, B., Chung, H.*, et al.* (2013a). Systematic identification of molecular subtype-selective vulnerabilities in non-small-cell lung cancer. Cell *155*, 552-566.
Kim, J. Y., Welsh, E. A., Oguz, U., Fang, B., Bai, Y., Kinose, F., Bronk, C., Remsing Rix, L. L., Beg, A. A., Rix, U.*, et al.* (2013b). Dissection of TBK1 signaling via phosphoproteomics in lung cancer cells. Proc Natl Acad Sci U S A *110*, 12414-12419.

Kirmizis, A., Bartley, S. M., Kuzmichev, A., Margueron, R., Reinberg, D., Green, R., and Farnham, P. J. (2004). Silencing of human polycomb target genes is associated with methylation of histone H3 Lys 27. Genes Dev *18*, 1592-1605.
Kittler, R., Zhou, J., Hua, S., Ma, L., Liu, Y., Pendleton, E., Cheng, C., Gerstein, M., and White, K. P. (2013). A comprehensive nuclear receptor network for breast cancer cells. Cell Rep *3*, 538-551.
Kleopa, K. A., and Sargiannidou, I. (2014). Connexins, gap junctions and peripheral neuropathy. Neurosci Lett.
Komurov, K., Dursun, S., Erdin, S., and Ram, P. T. (2012). NetWalker: a contextual network analysis tool for functional genomics. BMC Genomics *13*, 282.
Komurov, K., White, M. A., and Ram, P. T. (2010). Use of data-biased random walks on graphs for the retrieval of context-specific networks from genomic data. PLoS Comput Biol *6*.
Kong, X., Fan, H., Liu, X., Wang, R., Liang, J., Gupta, N., Chen, Y., Fang, F., and Chang, Y. (2009). Peroxisome proliferator-activated receptor gamma coactivator-1alpha enhances antiproliferative activity of 5'-deoxy-5-fluorouridine in cancer cells through induction of uridine phosphorylase. Mol Pharmacol *76*, 854-860.
Krzysik-Walker, S. M., Gonzalez-Mariscal, I., Scheibye-Knudsen, M., Indig, F. E., and Bernier, M. (2013). The biarylpyrazole compound AM251 alters mitochondrial physiology via proteolytic degradation of ERRalpha. Mol Pharmacol *83*, 157-166.
Laganiere, J., Tremblay, G. B., Dufour, C. R., Giroux, S., Rousseau, F., and Giguere, V. (2004). A polymorphic autoregulatory hormone response element in the human estrogen-related receptor alpha (ERRalpha) promoter dictates peroxisome proliferator-activated receptor gamma coactivator-1alpha control of ERRalpha expression. J Biol Chem *279*, 18504-18510.
Langmead, B., Trapnell, C., Pop, M., and Salzberg, S. L. (2009). Ultrafast and memory-efficient alignment of short DNA sequences to the human genome. Genome Biol *10*, R25.
Lanvin, O., Bianco, S., Kersual, N., Chalbos, D., and Vanacker, J. M. (2007). Potentiation of ICI182,780 (Fulvestrant)-induced estrogen receptor-alpha degradation by the estrogen receptor-related receptor-alpha inverse agonist XCT790. J Biol Chem *282*, 28328-28334.
Larkin, J., Ascierto, P. A., Dreno, B., Atkinson, V., Liszkay, G., Maio, M., Mandala, M., Demidov, L., Stroyakovskiy, D., Thomas, L.*, et al.* (2014). Combined vemurafenib and cobimetinib in BRAF-mutated melanoma. N Engl J Med *371*, 1867-1876.
Lawrence, M. S., Stojanov, P., Polak, P., Kryukov, G. V., Cibulskis, K., Sivachenko, A., Carter, S. L., Stewart, C., Mermel, C. H., Roberts, S. A.*, et al.* (2013). Mutational heterogeneity in cancer and the search for new cancer-associated genes. Nature *499*, 214-218.
Lin, L., Sabnis, A. J., Chan, E., Olivas, V., Cade, L., Pazarentzos, E., Asthana, S., Neel, D., Yan, J. J., Lu, X.*, et al.* (2015). The Hippo effector YAP promotes resistance to RAF- and MEK-targeted cancer therapies. Nat Genet *47*, 250-256.
Lito, P., Rosen, N., and Solit, D. B. (2013). Tumor adaptation and resistance to RAF inhibitors. Nat Med *19*, 1401-1409.

Liu, D., Hinshelwood, M. M., Giguere, V., and Mendelson, C. R. (2006). Estrogen related receptor-alpha enhances surfactant protein-A gene expression in fetal lung type II cells. Endocrinology *147*, 5187-5195.
Lo, W. S., Gardiner, E., Xu, Z., Lau, C. F., Wang, F., Zhou, J. J., Mendlein, J. D., Nangle, L. A., Chiang, K. P., Yang, X. L.*, et al.* (2014). Human tRNA synthetase catalytic nulls with diverse functions. Science *345*, 328-332.
Long, G. V., Fung, C., Menzies, A. M., Pupo, G. M., Carlino, M. S., Hyman, J., Shahheydari, H., Tembe, V., Thompson, J. F., Saw, R. P.*, et al.* (2014a). Increased MAPK reactivation in early resistance to dabrafenib/trametinib combination therapy of BRAF-mutant metastatic melanoma. Nat Commun *5*, 5694.
Long, G. V., Stroyakovskiy, D., Gogas, H., Levchenko, E., de Braud, F., Larkin, J., Garbe, C., Jouary, T., Hauschild, A., Grob, J. J.*, et al.* (2014b). Combined BRAF and MEK inhibition versus BRAF inhibition alone in melanoma. N Engl J Med *371*, 1877-1888.
Lu, N., Wang, W., Liu, J., and Wong, C. W. (2011). Protein kinase C epsilon affects mitochondrial function through estrogen-related receptor alpha. Cell Signal *23*, 1473-1478.
McElroy, W. T., and DeShong, P. (2006). Synthesis of the CD-ring of the anticancer agent streptonigrin: studies of aryl–aryl coupling methodologies. In Tetrahedron, pp. 6945-6954.
McGill, G. G., Haq, R., Nishimura, E. K., and Fisher, D. E. (2006). c-Met expression is regulated by Mitf in the melanocyte lineage. J Biol Chem *281*, 10365-10373.
McGill, G. G., Horstmann, M., Widlund, H. R., Du, J., Motyckova, G., Nishimura, E. K., Lin, Y. L., Ramaswamy, S., Avery, W., Ding, H. F.*, et al.* (2002). Bcl2 regulation by the melanocyte master regulator Mitf modulates lineage survival and melanoma cell viability. Cell *109*, 707-718.
Meador, C. B., and Pao, W. (2015). Old Habits Die Hard: Addiction of BRAF-Mutant Cancer Cells to MAP Kinase Signaling. Cancer Discov *5*, 348-350.
Mermel, C. H., Schumacher, S. E., Hill, B., Meyerson, M. L., Beroukhim, R., and Getz, G. (2011). GISTIC2.0 facilitates sensitive and confident localization of the targets of focal somatic copy-number alteration in human cancers. Genome Biol *12*, R41.
Murray, J., and Huss, J. M. (2011). Estrogen-related receptor alpha regulates skeletal myocyte differentiation via modulation of the ERK MAP kinase pathway. Am J Physiol Cell Physiol *301*, C630-645.
Nakashima, N., Noguchi, E., and Nishimoto, T. (1999). Saccharomyces cerevisiae putative G protein, Gtr1p, which forms complexes with itself and a novel protein designated as Gtr2p, negatively regulates the Ran/Gsp1p G protein cycle through Gtr2p. Genetics *152*, 853-867.
Nazarian, R., Shi, H., Wang, Q., Kong, X., Koya, R. C., Lee, H., Chen, Z., Lee, M. K., Attar, N., Sazegar, H.*, et al.* (2010). Melanomas acquire resistance to B-RAF(V600E) inhibition by RTK or N-RAS upregulation. Nature *468*, 973-977.
Ohsawa, S., Sato, Y., Enomoto, M., Nakamura, M., Betsumiya, A., and Igaki, T. (2012). Mitochondrial defect drives non-autonomous tumour progression through Hippo signalling in Drosophila. Nature *490*, 547-551.

Ou, Y. H., Torres, M., Ram, R., Formstecher, E., Roland, C., Cheng, T., Brekken, R., Wurz, R., Tasker, A., Polverino, T.*, et al.* (2011). TBK1 directly engages Akt/PKB survival signaling to support oncogenic transformation. Mol Cell *41*, 458-470.
Pilli, M., Arko-Mensah, J., Ponpuak, M., Roberts, E., Master, S., Mandell, M. A., Dupont, N., Ornatowski, W., Jiang, S., Bradfute, S. B.*, et al.* (2012). TBK-1 promotes autophagy-mediated antimicrobial defense by controlling autophagosome maturation. Immunity *37*, 223-234.
Pomerantz, J. L., and Baltimore, D. (1999). NF-kappaB activation by a signaling complex containing TRAF2, TANK and TBK1, a novel IKK-related kinase. EMBO J *18*, 6694-6704.
Poser, I., Sarov, M., Hutchins, J. R., Heriche, J. K., Toyoda, Y., Pozniakovsky, A., Weigl, D., Nitzsche, A., Hegemann, B., Bird, A. W.*, et al.* (2008). BAC TransgeneOmics: a high-throughput method for exploration of protein function in mammals. Nat Methods *5*, 409-415.
Potterf, S. B., Furumura, M., Dunn, K. J., Arnheiter, H., and Pavan, W. J. (2000). Transcription factor hierarchy in Waardenburg syndrome: regulation of MITF expression by SOX10 and PAX3. Hum Genet *107*, 1-6.
Potts, M. B., McMillan, E. A., Rosales, T. I., Kim, H. S., Ou, Y. H., Toombs, J. E., Brekken, R. A., Minden, M. D., MacMillan, J. B., and White, M. A. (2015). Mode of action and pharmacogenomic biomarkers for exceptional responders to didemnin B. Nat Chem Biol.
Poulikakos, P. I., Persaud, Y., Janakiraman, M., Kong, X., Ng, C., Moriceau, G., Shi, H., Atefi, M., Titz, B., Gabay, M. T.*, et al.* (2011). RAF inhibitor resistance is mediated by dimerization of aberrantly spliced BRAF(V600E). Nature *480*, 387-390.
Prasad, M. K., Reed, X., Gorkin, D. U., Cronin, J. C., McAdow, A. R., Chain, K., Hodonsky, C. J., Jones, E. A., Svaren, J., Antonellis, A.*, et al.* (2011). SOX10 directly modulates ERBB3 transcription via an intronic neural crest enhancer. BMC Dev Biol *11*, 40.
Quintana, E., Piskounova, E., Shackleton, M., Weinberg, D., Eskiocak, U., Fullen, D. R., Johnson, T. M., and Morrison, S. J. (2012). Human melanoma metastasis in NSG mice correlates with clinical outcome in patients. Sci Transl Med *4*, 159ra149.
Quintana, E., Shackleton, M., Foster, H. R., Fullen, D. R., Sabel, M. S., Johnson, T. M., and Morrison, S. J. (2010). Phenotypic heterogeneity among tumorigenic melanoma cells from patients that is reversible and not hierarchically organized. Cancer Cell *18*, 510-523.
Quintana, E., Shackleton, M., Sabel, M. S., Fullen, D. R., Johnson, T. M., and Morrison, S. J. (2008). Efficient tumour formation by single human melanoma cells. Nature *456*, 593-598.
Ramirez, R. D., Sheridan, S., Girard, L., Sato, M., Kim, Y., Pollack, J., Peyton, M., Zou, Y., Kurie, J. M., Dimaio, J. M.*, et al.* (2004). Immortalization of human bronchial epithelial cells in the absence of viral oncoproteins. Cancer Res *64*, 9027-9034.
Rasbach, K. A., Gupta, R. K., Ruas, J. L., Wu, J., Naseri, E., Estall, J. L., and Spiegelman, B. M. (2010). PGC-1alpha regulates a HIF2alpha-dependent switch in skeletal muscle fiber types. Proc Natl Acad Sci U S A *107*, 21866-21871.

Rizos, H., Menzies, A. M., Pupo, G. M., Carlino, M. S., Fung, C., Hyman, J., Haydu, L. E., Mijatov, B., Becker, T. M., Boyd, S. C*., et al.* (2014). BRAF inhibitor resistance mechanisms in metastatic melanoma: spectrum and clinical impact. Clin Cancer Res *20*, 1965-1977.

Robert, C., Karaszewska, B., Schachter, J., Rutkowski, P., Mackiewicz, A., Stroiakovski, D., Lichinitser, M., Dummer, R., Grange, F., Mortier, L*., et al.* (2015). Improved overall survival in melanoma with combined dabrafenib and trametinib. N Engl J Med *372*, 30-39.

Robert, C., Thomas, L., Bondarenko, I., O'Day, S., Weber, J., Garbe, C., Lebbe, C., Baurain, J. F., Testori, A., Grob, J. J*., et al.* (2011). Ipilimumab plus dacarbazine for previously untreated metastatic melanoma. N Engl J Med *364*, 2517-2526.

Sancak, Y., Bar-Peled, L., Zoncu, R., Markhard, A. L., Nada, S., and Sabatini, D. M. (2010). Ragulator-Rag complex targets mTORC1 to the lysosomal surface and is necessary for its activation by amino acids. Cell *141*, 290-303.

Sancak, Y., Peterson, T. R., Shaul, Y. D., Lindquist, R. A., Thoreen, C. C., Bar-Peled, L., and Sabatini, D. M. (2008). The Rag GTPases bind raptor and mediate amino acid signaling to mTORC1. Science *320*, 1496-1501.

Sandelin, A., Alkema, W., Engstrom, P., Wasserman, W. W., and Lenhard, B. (2004). JASPAR: an open-access database for eukaryotic transcription factor binding profiles. Nucleic Acids Res *32*, D91-94.

Schreiber, S. N., Knutti, D., Brogli, K., Uhlmann, T., and Kralli, A. (2003). The transcriptional coactivator PGC-1 regulates the expression and activity of the orphan nuclear receptor estrogen-related receptor alpha (ERRalpha). J Biol Chem *278*, 9013-9018.

Scott, K. L., Kabbarah, O., Liang, M. C., Ivanova, E., Anagnostou, V., Wu, J., Dhakal, S., Wu, M., Chen, S., Feinberg, T*., et al.* (2009). GOLPH3 modulates mTOR signalling and rapamycin sensitivity in cancer. Nature *459*, 1085-1090.

Sekiguchi, T., Hayashi, N., Wang, Y., and Kobayashi, H. (2008). Genetic evidence that Ras-like GTPases, Gtr1p, and Gtr2p, are involved in epigenetic control of gene expression in Saccharomyces cerevisiae. Biochem Biophys Res Commun *368*, 748-754.

Sekiguchi, T., Todaka, Y., Wang, Y., Hirose, E., Nakashima, N., and Nishimoto, T. (2004). A novel human nucleolar protein, Nop132, binds to the G proteins, RRAG A/C/D. J Biol Chem *279*, 8343-8350.

Serresi, M., Gargiulo, G., Proost, N., Siteur, B., Cesaroni, M., Koppens, M., Xie, H., Sutherland, K. D., Hulsman, D., Citterio, E*., et al.* (2016). Polycomb Repressive Complex 2 Is a Barrier to KRAS-Driven Inflammation and Epithelial-Mesenchymal Transition in Non-Small-Cell Lung Cancer. Cancer Cell *29*, 17-31.

Shakhova, O., Zingg, D., Schaefer, S. M., Hari, L., Civenni, G., Blunschi, J., Claudinot, S., Okoniewski, M., Beermann, F., Mihic-Probst, D*., et al.* (2012). Sox10 promotes the formation and maintenance of giant congenital naevi and melanoma. Nat Cell Biol *14*, 882-890.

Shannon, P., Markiel, A., Ozier, O., Baliga, N. S., Wang, J. T., Ramage, D., Amin, N., Schwikowski, B., and Ideker, T. (2003). Cytoscape: a software environment for integrated models of biomolecular interaction networks. Genome Res *13*, 2498-2504.

Sharma, S., tenOever, B. R., Grandvaux, N., Zhou, G. P., Lin, R., and Hiscott, J. (2003). Triggering the interferon antiviral response through an IKK-related pathway. Science *300*, 1148-1151.
Shi, H., Hugo, W., Kong, X., Hong, A., Koya, R. C., Moriceau, G., Chodon, T., Guo, R., Johnson, D. B., Dahlman, K. B.*, et al.* (2014). Acquired resistance and clonal evolution in melanoma during BRAF inhibitor therapy. Cancer Discov *4*, 80-93.
Shi, H., Moriceau, G., Kong, X., Lee, M. K., Lee, H., Koya, R. C., Ng, C., Chodon, T., Scolyer, R. A., Dahlman, K. B.*, et al.* (2012). Melanoma whole-exome sequencing identifies (V600E)B-RAF amplification-mediated acquired B-RAF inhibitor resistance. Nat Commun *3*, 724.
Shin, H., Liu, T., Manrai, A. K., and Liu, X. S. (2009). CEAS: cis-regulatory element annotation system. Bioinformatics *25*, 2605-2606.
Simon, M., Richard, E. M., Wang, X., Shahzad, M., Huang, V. H., Qaiser, T. A., Potluri, P., Mahl, S. E., Davila, A., Nazli, S.*, et al.* (2015). Mutations of Human NARS2, Encoding the Mitochondrial Asparaginyl-tRNA Synthetase, Cause Nonsyndromic Deafness and Leigh Syndrome. PLoS Genet *11*, e1005097.
Singh, N. K., Seo, B. Y., Vidyasagar, M., White, M. A., and Kim, H. S. (2013). siMacro: A Fast and Easy Data Processing Tool for Cell-Based Genomewide siRNA Screens. Genomics Inform *11*, 55-57.
Sivan, S., Suzan, F., Rona, O., Tamar, H., Vivian, B., Tamar, P., Jacob, S., Gal, M., and Michal, L. (2012). Serum CEACAM1 Correlates with Disease Progression and Survival in Malignant Melanoma Patients. Clin Dev Immunol *2012*, 290536.
Smyth, G. K. (2004). Linear models and empirical bayes methods for assessing differential expression in microarray experiments. Stat Appl Genet Mol Biol *3*, Article3.
Sofou, K., Kollberg, G., Holmstrom, M., Davila, M., Darin, N., Gustafsson, C. M., Holme, E., Oldfors, A., Tulinius, M., and Asin-Cayuela, J. (2015). Whole exome sequencing reveals mutations in NARS2 and PARS2, encoding the mitochondrial asparaginyl-tRNA synthetase and prolyl-tRNA synthetase, in patients with Alpers syndrome. Mol Genet Genomic Med *3*, 59-68.
Sperber, H., Mathieu, J., Wang, Y., Ferreccio, A., Hesson, J., Xu, Z., Fischer, K. A., Devi, A., Detraux, D., Gu, H.*, et al.* (2015). The metabolome regulates the epigenetic landscape during naive-to-primed human embryonic stem cell transition. Nat Cell Biol *17*, 1523-1535.
Strub, T., Giuliano, S., Ye, T., Bonet, C., Keime, C., Kobi, D., Le Gras, S., Cormont, M., Ballotti, R., Bertolotto, C., and Davidson, I. (2011). Essential role of microphthalmia transcription factor for DNA replication, mitosis and genomic stability in melanoma. Oncogene *30*, 2319-2332.
Su, W.-G., Dai, G., Xiao, K., Jia, H., Venable, J. D., and Bembenek, S. D. (2014). Novel heteroaryl and heterocycle compounds, composition and methods. In.
Sun, C., Wang, L., Huang, S., Heynen, G. J., Prahallad, A., Robert, C., Haanen, J., Blank, C., Wesseling, J., Willems, S. M.*, et al.* (2014). Reversible and adaptive resistance to BRAF(V600E) inhibition in melanoma. Nature *508*, 118-122.

Szigeti, K., Garcia, C. A., and Lupski, J. R. (2006). Charcot-Marie-Tooth disease and related hereditary polyneuropathies: molecular diagnostics determine aspects of medical management. Genet Med *8*, 86-92.
Talantov, D., Mazumder, A., Yu, J. X., Briggs, T., Jiang, Y., Backus, J., Atkins, D., and Wang, Y. (2005). Novel genes associated with malignant melanoma but not benign melanocytic lesions. Clin Cancer Res *11*, 7234-7242.
Teng, C. T., Beames, B., Alex Merrick, B., Martin, N., Romeo, C., and Jetten, A. M. (2014). Development of a stable cell line with an intact PGC-1alpha/ERRalpha axis for screening environmental chemicals. Biochem Biophys Res Commun *444*, 177-181.
Teyssier, C., Bianco, S., Lanvin, O., and Vanacker, J. M. (2008). The orphan receptor ERRalpha interferes with steroid signaling. Nucleic Acids Res *36*, 5350-5361.
Thies, A., Moll, I., Berger, J., Wagener, C., Brummer, J., Schulze, H. J., Brunner, G., and Schumacher, U. (2002). CEACAM1 expression in cutaneous malignant melanoma predicts the development of metastatic disease. J Clin Oncol *20*, 2530-2536.
Topalian, S. L., Hodi, F. S., Brahmer, J. R., Gettinger, S. N., Smith, D. C., McDermott, D. F., Powderly, J. D., Carvajal, R. D., Sosman, J. A., Atkins, M. B.*, et al.* (2012). Safety, activity, and immune correlates of anti-PD-1 antibody in cancer. N Engl J Med *366*, 2443-2454.
Ulanovskaya, O. A., Zuhl, A. M., and Cravatt, B. F. (2013). NNMT promotes epigenetic remodeling in cancer by creating a metabolic methylation sink. Nat Chem Biol *9*, 300-306.
Verastegui, C., Bille, K., Ortonne, J. P., and Ballotti, R. (2000). Regulation of the microphthalmia-associated transcription factor gene by the Waardenburg syndrome type 4 gene, SOX10. J Biol Chem *275*, 30757-30760.
Villanueva, J., Vultur, A., Lee, J. T., Somasundaram, R., Fukunaga-Kalabis, M., Cipolla, A. K., Wubbenhorst, B., Xu, X., Gimotty, P. A., Kee, D.*, et al.* (2010). Acquired resistance to BRAF inhibitors mediated by a RAF kinase switch in melanoma can be overcome by cotargeting MEK and IGF-1R/PI3K. Cancer Cell *18*, 683-695.
Wang, J., Huang, S. K., Marzese, D. M., Hsu, S. C., Kawas, N. P., Chong, K. K., Long, G. V., Menzies, A. M., Scolyer, R. A., Izraely, S.*, et al.* (2015a). Epigenetic changes of EGFR have an important role in BRAF inhibitor-resistant cutaneous melanomas. J Invest Dermatol *135*, 532-541.
Wang, J., Wang, Y., and Wong, C. (2010). Oestrogen-related receptor alpha inverse agonist XCT-790 arrests A549 lung cancer cell population growth by inducing mitochondrial reactive oxygen species production. Cell Prolif *43*, 103-113.
Wang, X., Lopez, O., Sweet, R. A., Becker, J. T., DeKosky, S. T., Barmada, M. M., Feingold, E., Demirci, F. Y., and Kamboh, M. I. (2015b). Genetic Determinants of Survival in Patients with Alzheimer's Disease. J Alzheimers Dis.
Wang, Y., Nakashima, N., Sekiguchi, T., and Nishimoto, T. (2005). Saccharomyces cerevisiae GTPase complex: Gtr1p-Gtr2p regulates cell-proliferation through Saccharomyces cerevisiae Ran-binding protein, Yrb2p. Biochem Biophys Res Commun *336*, 639-645.

West, A. P., Khoury-Hanold, W., Staron, M., Tal, M. C., Pineda, C. M., Lang, S. M., Bestwick, M., Duguay, B. A., Raimundo, N., MacDuff, D. A*., et al.* (2015). Mitochondrial DNA stress primes the antiviral innate immune response. Nature.
Wingender, E., Dietze, P., Karas, H., and Knuppel, R. (1996). TRANSFAC: a database on transcription factors and their DNA binding sites. Nucleic Acids Res *24*, 238-241.
Witkiewicz, A. K., McMillan, E. A., Balaji, U., Baek, G., Lin, W. C., Mansour, J., Mollaee, M., Wagner, K. U., Koduru, P., Yopp, A*., et al.* (2015). Whole-exome sequencing of pancreatic cancer defines genetic diversity and therapeutic targets. Nat Commun *6*, 6744.
Wu, F., Wang, J., Wang, Y., Kwok, T. T., Kong, S. K., and Wong, C. (2009). Estrogen-related receptor alpha (ERRalpha) inverse agonist XCT-790 induces cell death in chemotherapeutic resistant cancer cells. Chem Biol Interact *181*, 236-242.
Xie, Y., Wang, X., and Story, M. (2009). Statistical methods of background correction for Illumina BeadArray data. Bioinformatics *25*, 751-757.
Xu, L., Shen, S. S., Hoshida, Y., Subramanian, A., Ross, K., Brunet, J. P., Wagner, S. N., Ramaswamy, S., Mesirov, J. P., and Hynes, R. O. (2008). Gene expression changes in an animal melanoma model correlate with aggressiveness of human melanoma metastases. Mol Cancer Res *6*, 760-769.
Yang, C., Sudderth, J., Dang, T., Bachoo, R. M., McDonald, J. G., and DeBerardinis, R. J. (2009). Glioblastoma cells require glutamate dehydrogenase to survive impairments of glucose metabolism or Akt signaling. Cancer Res *69*, 7986-7993.
Zhang, Y., Liu, T., Meyer, C. A., Eeckhoute, J., Johnson, D. S., Bernstein, B. E., Nusbaum, C., Myers, R. M., Brown, M., Li, W., and Liu, X. S. (2008). Model-based analysis of ChIP-Seq (MACS). Genome Biol *9*, R137.
Zhu, L. L., Liu, Y., Cui, A. F., Shao, D., Liang, J. C., Liu, X. J., Chen, Y., Gupta, N., Fang, F. D., and Chang, Y. S. (2010). PGC-1alpha coactivates estrogen-related receptor-alpha to induce the expression of glucokinase. Am J Physiol Endocrinol Metab *298*, E1210-1218.
Zou, C., Yu, S., Xu, Z., Wu, D., Ng, C. F., Yao, X., Yew, D. T., Vanacker, J. M., and Chan, F. L. (2014). ERRalpha augments HIF-1 signalling by directly interacting with HIF-1alpha in normoxic and hypoxic prostate cancer cells. J Pathol *233*, 61-73.
Zou, H., and Hastie, T. (2005). Regularization and variable selection via the elastic net. J R Statist Soc B *67*, 301-320.